Thesis

Pump-probe Spectroscopy on Cubic III-Nitride Structures

Joshua J. Whale, MSc.

Thesis presented to the University of Nottingham
for the degree of Doctor of Philosophy,
January 2019

Contents

List of Figures

List of Tables

Abstract

This thesis presents a series of studies applying the picosecond acoustics technique to investigate the ultrafast phonon dynamics in cubic III-nitride epilayers grown by molecular beam epitaxy on GaAs (001) substrates. The aim of these studies was twofold, firstly for the investigation and characterisation of the photo-elastic properties of zinc-blende (cubic) nitride materials. And secondly for the study of high frequency coherent phonons in sub-μm-thick cubic AlGaN structures with the general aim of modulating light in the UV spectrum at up to terahertz frequencies.

A series of $c-Al_xGa_{1-x}N$ layers were produced with aluminium fractions (x) ranging from 0 - 0.66. So called Brillouin oscillations were studied in three of the samples around the 50% Al fraction by optically pumping the GaAs substrate through the transparent epilayer and tracking the strain pulse as it propagates toward the surface. We obtain the values for complex refractive index and their dependence on Al content and the optical wavelength in the range 250-300 nm. Spectroscopic ellipsometry measurements in the same energy range are taken for comparative analysis. Analysis of the surface reflection of phonons matching the Brillouin backscattering frequency are used to estimate the surface roughness of the samples and are in close agreement with measurements of the surface topology by atomic force microscopy.

The phononic properties of these epilayers were further investigated in a free-standing membrane geometry by etching away the substrate. In the membranes the optical absorption is weak so strain is generated approximately uniformly in the layer. This leads to a periodic modulation of the layer thickness with frequency related to the round trip time of acoustic phonons in the layer. The optical reflectivity response did not rely on the photoelastic effect but predominantly the optical cavity thickness modulation, so confined membrane modes were observed in the full series of samples. From this data the longitudinal speed of sound in material released from the interfacial stress is defined.

In the second part of this work single cubic GaN quantum well (QW) with $c-Al_xGa_{1-x}N$ barrier cladding layers are utilised for the generation and detection of narrow strain pulses in buried layers. The QW did not function well as a detector at the probe wavelengths applied because the photo-elastic response could not be disentangled from the barrier layers. Acoustic pulses generated in the QW are observed in

the GaAs substrate after propagating some distance and are independently resolved with a time resolution ∼3.2 ps. Theoretical calculations of the excited carrier distribution in the well indicate the efficient generation of frequencies up to 10 THz dependent on the abrupt electronic junction between the well and barrier layers.

Terahertz coherent folded longitudinal acoustic (FLA) phonon modes in a zinc-blende GaN/AlN superlattice (SL) are observed and studied by two colour time-resolved pump-probe spectroscopy. We observe the characteristic triplet of first-order mini-Brillouin zone folded modes at the zone center (q = 0), with frequency 1.2 THz, and with sidebands at phonon vector $q = 2k_{laser}$ where the detection mechanism is strongest. The observed frequencies show good agreement with the theoretical dispersion curves in the elastic limit. Picosecond acoustics is demonstrated as a diagnostic tool for measuring the period of SLs.

List of Publications

J. Whale, A. V. Akimov, S. V. Novikov, C. J. Mellor and A. J. Kent. Photoelastic properties of zinc-blende $Al_xGa_{1-x}N$ in the UV: Picosecond ultrasonic studies, *Physical Review Materials*, 2:034606, 2018.

S. V. Novikov, C. R. Staddon, J. Whale, A. J. Kent, and C. T. Foxon. Growth of free-standing wurtzite AlGaN by MBE using a highly efficient RF plasma source, *J. Vac. Sci. Technol. B*, 34:02L102, 2016

T. Gohil, J. Whale, G. Lioliou, S. V. Novikov, C. T. Foxon, A. J. Kent, and A. M. Barnett. X-ray detection with zinc-blende (cubic) GaN Schottky diodes, *Scientific Reports*, 6:29535, 2016

Acknowledgements

There are many people who deserve credit for making the assembly of this thesis possible. I would like to start off by thanking my supervisor Prof. Tony Kent for the opportunity in the first place and for his steady guidance throughout the process, both in and out of the lab. Andrey Akimov for his continual encouragement and support with experimental matters.

I am grateful for all the help received from people in the clean room, particularly from Jas Chauhan and Dave Taylor who were always ready to drop what they were doing to assist students. Thanks are due to all the members of the THz Acoustics group, past and present. To Caroline Poyser I say thank you for teaching me everything I know about phonons, to Bill York for many enlightening conversations and to Sarah Heywood for her steadfast friendship. Anyone who I haven't called by name who made tea breaks a little more enjoyable and was willing to listen to my crazy ideas.

I would like to thank my family, though they might not always have believed in me they supported me unfailingly for which I am eternally grateful. And last of all, thanks go to God who makes all things possible and who found me in the course of this endeavour.

Chapter 1

Introduction

In much the same way that light can behave as both a wave and a particle, so too can sound be modelled by a wave-particle duality. Where an individual quantum of light is described as a photon, a quantised lattice vibration in a semiconductor is called a phonon. Phonons are the medium for the transfer of heat and sound, as such there is a concerted research effort towards the fine control of phonons to enable the realisation of devices for applications including acoustic rectification and thermal cloaking among others [1, 2]. The work presented in this thesis explores the effects of acoustic pulses on semiconductor thin films and nanostructures and the potential applications. The focus is specifically on the cubic III-nitride semiconductors as a promising but novel area of study due to the complexities of the growth process. This introductory chapter begins by making the case for nitride semiconductors over conventional arsenides and the inherent differences arising from the cubic crystal structure as well as delivering a review of the existing literature, focusing on that which is closely related to topics covered in this work. It then goes on to provide an explanation of the concepts and applications of picosecond acoustics and the implications for nitride research.

1.1 Introduction to Nitride Semiconductors

Over the past 40 years the III-nitride semiconductors gallium nitride (GaN), aluminium nitride (AlN) and indium nitride (InN) have been of great interest due to their potential applications in the field of electronics and optoelectronics. In comparison to the III-arsenide materials, the nitride binary alloys have a much wider direct bandgap which can be exceptionally useful in the fields of optics and power electronics. The energy gap ranges from the near infrared for InN (0.7 eV) to near UV in GaN (3.4 eV) and finally UV-C or deep UV for AlN (6.2 eV). By tuning the composition

of the ternary alloys it is possible to create optoelectronic devices that cover almost the entire spectral range; from infra-red down to deep ultraviolet. Today commercial blue GaN LEDs are used extensively in white light sources found in television and mobile phone screens and automotive and street lighting. There is a particular effort being devoted to the development of optoelectronics which may span the UV spectral region, these would have a host of commercial applications. In the UV-C in water purification, e.g., wastewater treatment and recycling [3–5] in addition to sterilisation of point-of-use systems and disinfection of medical equipment. In the UV-B range uses in phototherapy i.e., the treatment of skin disease [6] as well as grow lighting to encourage specific markers in plants [7]. AlGaN alloys are an ideal choice as the basis for these emerging technologies. The nitride materials have also been identified as candidates for the next generation of power electronics along with SiC. Interest is driven by the superior material characteristics: the typically high electric breakdown field, higher operating temperatures, high electron saturation velocity and high mobility. For example, Romanczyk et al. have recently developed a high-electron mobility transistor (HEMT) that boasts a record power density of $8\,\mathrm{W\,mm^{-1}}$ operating at $20\,\mathrm{V}$ [8].

The III-nitride semiconductors usually crystallise in the hexagonal (wurtzite) polytype. Wurtzite nitrides grown on the c-plane are subject to spontaneous polarisation fields as a result of the pyroelectric nature of the material in addition to net piezoelectric polarisation when strain is applied to the lattice as the crystal symmetry does not possess a centre of inversion. The presence of such internal fields has a considerable impact on device performance and must be considered when designing a new device. For instance the influence of large strain and therefore large polarisation fields in multiple quantum well (QW) systems result in the quantum confined stark effect negatively affecting the performance of light emitting diodes and lasers [9]. In addition the latent fields may decrease internal quantum efficiency of recombination by spatially separating free electrons and holes at opposite ends of the quantum well. The effect is not only detrimental however, the built in electric fields are the reason for the outstanding performance of III-nitride based HEMTs which operate on the creation of highly mobile two-dimensional electron gas (2DEG) at the band discontinuity between the GaN/AlGaN interface [10].

It is possible to grow wurtzite III-nitride semiconductors in both polar and semipolar orientations by initiating epitaxial growth on planes perpendicular or angled

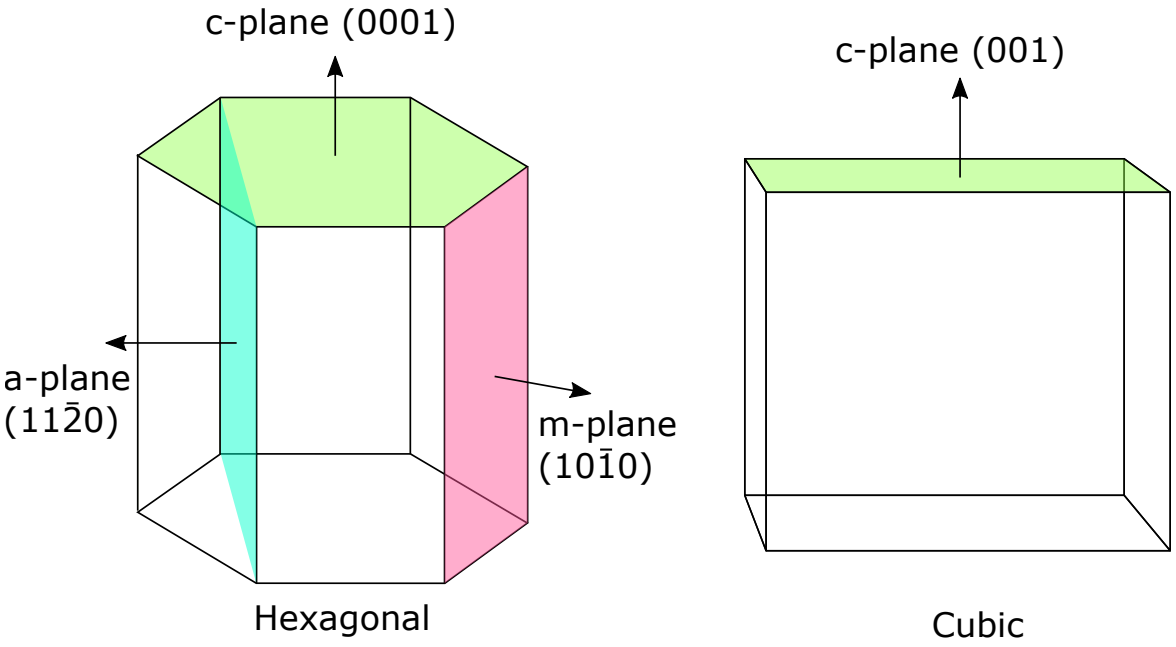

Figure 1.1: An illustration of different growth planes for wurtzite and zinc-blende semiconductors

with respect to the c-plane as shown in Fig. 1.1. The problem with such techniques is that the free-standing growth substrates are costly and difficult to produce as they are manufactured by cleaving bulk hexagonal material grown on the c-plane and are therefore size limited [11,12]. A more elegant solution is to simply use the unpolarized cubic (zinc-blende) phase of nitride semiconductors. Zinc-blende crystals grown in the (001) direction possess a centre of inversion such that the charge distribution is symmetric even when the lattice is subject to strain, the crystal symmetry is also sufficient that the dipole moments in the Group-III–N bonds are cancelled out on a macroscopic scale and therefore do not suffer the effects. Another consequence of the additional axis of crystal symmetry is the enhanced mobility of the carriers (particularly holes) which is approximately one order of magnitude higher than in hexagonal layers, as well as reduced phonon scattering which impacts thermal conductivity.

1.1.1 Basic Properties of Nitrides

The vast majority of research into the nitride semiconductors has been focused on the hexagonal phase due to it being the thermodynamically stable form and therefore simpler to grow. In spite of this there is still a significant body of work on the cubic phase. This section will provide a review of the state of existing literature concerning the growth and acousto-optical properties of the III-nitrides and an introduction to

the basic properties of the material in both hexagonal and cubic variations.

It is well established that the electronic properties of any semiconductor are dependent on the atomic arrangement of the constituent elements. An unavoidable side effect of the growth process is the inclusion of impurities, defects and vacancies in the material. This has further effects on the atomic arrangement and therefore the electrical properties of the material which will be discussed further on.

Crystal Structure

Group-III nitrides can take three crystalline structures: wurtzite, zinc-blende and rock salt. For all III-nitrides the thermodynamically stable configuration under ambient conditions is wurtzite. The cubic variation is a metastable structure, but can be stabilised for thin films grown epitaxially on the appropriate face of a cubic substrate. Under these conditions the tendency to form a wurtzite structure can be overcome by the influence of the substrate, however as layers become thicker the rate of hexagonal defect inclusions tends to increase. As the cohesive energies of the two polytypes are very similar [13] it is easy to observe transitions between the wurtzite and zinc-blende crystal structure through stacking faults of basal planes. The rock-salt arrangement can only be induced at very high pressures which increase the ionicity of the chemical bonds and is not stable during epitaxial growth; it is therefore mostly confined to laboratory environments.

The electronic and optical properties of a crystal are very sensitive to its real structure as a direct consequence of the valence electron density distribution. The wurtzite structure has a hexagonal unit cell and therefore two lattice constants, a and c. It holds six atoms of each type. The wurtzite crystal structure is not invariant with respect to inversion along the c-direction. A translation such as this results in an exchange of group-III atoms with nitrogen atoms and vice-versa. Therefore if the lattice is subject to strain, such as that arising from lattice mismatch, there is a spatial separation of ionic charges which affects the symmetry of the internal electric field. The zinc-blende structure has a cubic unit cell and a much greater degree of crystallographic symmetry as the lattice constants are identical in three perpendicular directions. It is defined by two interlocked face centred cubic lattices offset by one quarter along the diagonal of the unit cell. The similar covalent radii of the elements results in strong covalent

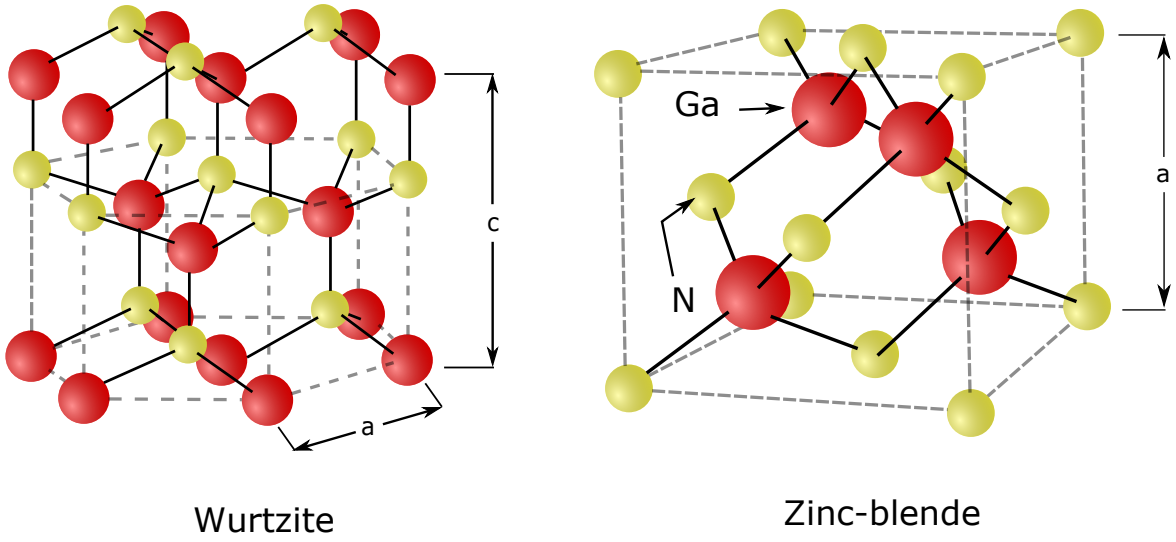

Figure 1.2: The atomic arrangement for both (a) wurtzite and (b) zinc-blende formation

bonding and consequently high chemical inertness and thermodynamic stability. It contains four atoms of each type.

Fig. 1.2 shows that in both cases every nitrogen atom is tetrahedrally coordinated by four group-III atoms and that the reverse is true for each group-III atom. The main difference lies in the bond angle between neighbouring atoms and consequently the stacking sequence of closest packed diatomic planes, taking Ga and N pairs as an example, leading to either **AaBbCcAaBbCc** sequence in the $\langle 0001 \rangle$ plane (zinc-blende) or **AaBbAaBbAaBb** in the $\langle 111 \rangle$ plane (wurtzite).

The basic parameters for the relevant configurations of the III-nitride groups can be seen in Table 1.1 and Table 1.2. The valence band at the Γ point in wurtzite nitrides is non-symmetric in k-space compared to the zinc-blende nitrides, therefore as the effective mass is the second derivative of the band structure for each direction away from the Γ point there are two separate values. For the cubic nitrides only one effective hole mass is necessary.

For the case of a grown layer with lattice constant larger than the substrate the in-plane lattice constant is decreased and the lattice constant in the grown direction is increased due to the requirement for constant unit cell volume. The reverse is true for a substrate with larger lattice constant. The change in the lattice constants and thermal expansion coefficient differences during epitaxial growth and cooling causes

Parameter	GaN	AlN	InN
Direct Band Gap (eV)	3.39 [14]	6.20 [15]	0.69 [16]
Effective electron mass, m_e	0.22 m_0 [17]	0.35 m_0 [18]	0.033 m_0 [19]
Effective hole mass (heavy), $m_{hh}^{\parallel}$	1.27 m_0 [20]	2.04 m_0 [20]	1.56 m_0 [20]
$m_{hh}^{\perp}$	1.02 m_0 [20]	2.08 m_0 [20]	1.25 m_0 [20]
Effective hole mass (light), $m_{lh}^{\parallel}$	1.27 m_0 [20]	2.04 m_0 [20]	1.56 m_0 [20]
$m_{lh}^{\perp}$	0.11 m_0 [20]	0.20 m_0 [20]	0.09 m_0 [20]
Electron affinity, χ (eV)	3.4 [21]	1.9 [22]	5.8 [23]
Young modulus (GPa) c_{11}	390 [24]	396 [24]	223 [24]
c_{12}	145 [24]	137 [24]	115 [24]
Lattice constant, a (Å)	3.189 [25]	3.110 [25]	3.540 [25]
Lattice constant, c (Å)	5.185 [25]	4.980 [25]	5.700 [25]

Table 1.1: Basic Parameters of Hexagonal Nitrides at 300K

storage of elastic energy in the crystal as strain. A consequence of this is that the total energy of the crystal can be reduced by the inclusion of defects and dislocations, which has been one of the main obstacles in the pursuit of high quality bulk nitride materials.

As seen in Fig. 1.3 the compressive in-plane residual strain causes the lattice constant perpendicular to the surface to be slightly expanded. The value for the critical thickness h_c, at which the incorporation of defects becomes energetically favourable, can be calculated by equating the stored elastic energy and the defect energy [31] leading to an implicit relation modified by Sherwin et al. [32] for a III-nitride system.

$$h_c = \frac{a_{layer}\left(1-\frac{\nu}{4}\right)}{4\sqrt{2}\pi\left(1+\nu\right)f} * ln\frac{\sqrt{2}h_c}{a_{substrate}} + 1) \tag{1.1}$$

where $\nu = \frac{c_{12}}{c_{11}+c_{12}}$ the Poisson ration and $f = \frac{a_{layer}-a_{substrate}}{a_{layer}}$ the lattice mismatch where a corresponds to the in-plane lattice constant. This result makes it clear

Parameter	**c-GaN**	**c-AlN**	**c-InN**
Direct Band Gap (eV)	3.20 [26]	5.93 [27]	0.595 [28]
Electron affinity, χ (eV)	-	-	-
Effective electron mass, m_e	0.15 m_0 [20]	0.25 m_0 [29]	0.07 m_0 [29]
Effective hole mass (heavy), m_{hh}	0.80 m_0 [20]	1.20 m_0 [20]	0.84 m_0 [20]
Effective hole mass (light), m_{lh}	0.18 m_0 [20]	0.33 m_0 [20]	0.16 m_0 [20]
Young modulus (GPa) c_{11}	296 [30]	304 [30]	184 [30]
c_{12}	154 [30]	152 [30]	116 [30]
Lattice constant, a (Å)	4.500 [29]	4.380 [29]	4.980 [29]

Table 1.2: Basic Parameters of Cubic Nitrides at 300K

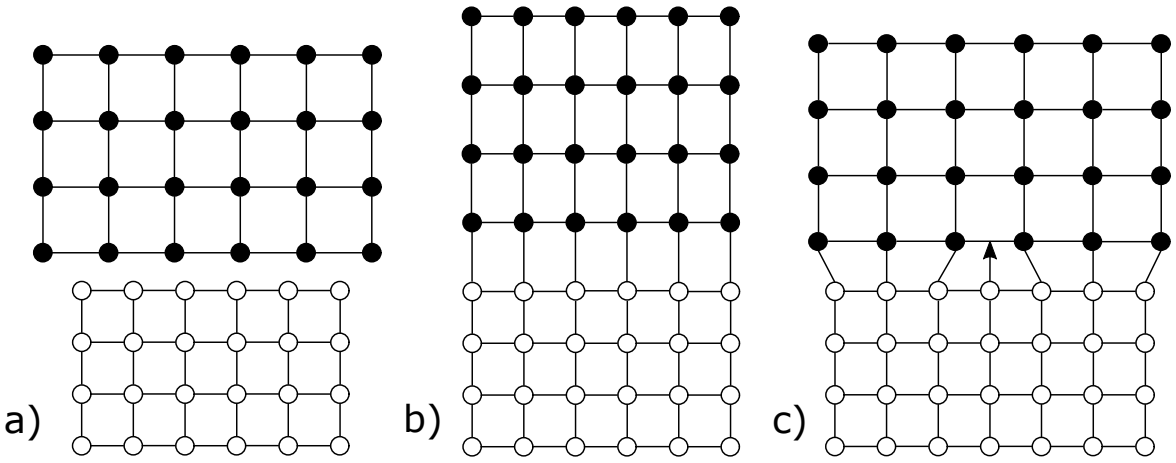

Figure 1.3: Lattice structure during heteroepitaxy with a) separated layers b) strained layer c) relaxed layer with incorporation of defects

that the limiting factor for the growth of thick nitride films with low defect density is the availability of appropriately lattice matched commercial substrates for homoepitaxy, particularly in the case of the cubic nitrides for which no commercial option yet exists. Worse still for the cubic nitrides is the fact that any hexagonal inclusions created by structural defects are thermodynamically stable and cannot be eliminated once created.

1.2 Summary of Nitride Growth

GaN was synthesized for the first time in 1938 by Juza and Hahn [33] by passing ammonia over hot gallium to produce small needles and platelets, which were sufficient to study the crystal structure and determine the lattice constant and crystal structure. In 1959 Grimmeiss and Koelmans used the same method of growth to produce small crystals of GaN and were able to measure their photoluminescence (PL) spectra [34]. The first large area thin films were reported in 1969 by Maruska and Tietjen [35] who used the hydride vapour phase epitaxy (HVPE) method to produce GaN epilayers on sapphire substrates. Since then a considerable progress has been made, not least in developing the possibility and quality of growth in the cubic polytype. This section will summarise the growth techniques used in the manufacture of cubic nitrides and their physical properties as a point of reference to material used in this work.

1.2.1 Growth of Cubic GaN

As described previously gallium nitride may crystallise in either the stable wurtzite (α) form or the metastable zinc-blende (β) phase. The type of nucleation that occurs is dependent on both the substrate orientation and the growth parameters. Okumura et al. [36] first demonstrated the growth by gas phase molecular beam epitaxy (MBE) of both wurtzite and zinc-blende material on the (111) and (001) face of GaAs substrates respectively. It was also found that MBE conditions such as pre-growth nitridation of the substrate and the arsenic over-pressure in the chamber can be used to selectively influence the subsequent phase of the film between cubic, mixed-phase and hexagonal [37].

There are no reports on the growth of zinc-blende (cubic) GaN bulk crystals and substrates, and all attempts to achieve bulk cubic GaN substrates have so far failed. Previously at the University of Nottingham, work was conducted to develop free-standing cubic GaN layers with thicknesses up to 100 µm to be used as substrates in further growth. This technique has the advantage over non-polar material of not having to be cleaved through the c-axis and therefore having a width limited by the growth thickness, instead having a wafer size of 2-3 inches diameter [38]. RHEED and TEM measurements showed no evidence of hexagonal inclusions within the first 10 µm but layers with thicknesses from 20-50 µm showed from nuclear magnetic resonance (NMR) imaging that the hexagonal fraction had increased to an average of 10% [39, 40]. For the purpose of growing the thick films, the growth rate being on the

order of $0.3\,\mu m\,h^{-1}$, the MBE system was modified to maintain stable temperatures and flux ratios for long periods of time.

Reducing the inclusion of hexagonal content, especially in bulk material, is a key factor when considering the optimal growth method. As et al. [41] successfully used radio-frequency plasma assisted molecular beam epitaxy (pa-MBE) to grow cubic GaN epilayers up to 1.5 µm on GaAs (001) substrates with a hexagonal fraction <0.1% estimated from the relative photoluminescence (PL) yield and x-ray diffraction (XRD) measurements. In 2002 Sung et al. [42] studied the effects of varying the III-V ratio between a Ga-rich, N-rich and stoichiometric growth conditions. It was found that growing in a slightly Ga-rich environment without the formation of gallium droplets resulted in a higher quality film with fewer hexagonal inclusions.

Cubic GaN has to date been grown on many substrates with 4-fold symmetry including GaAs, Si, 3C-SiC, MgO and Al_2O_3 (sapphire) [36, 40, 43–46]. The most popular choice being 3C-SiC which possesses a lattice constant much closer to that of c-GaN at 3.7% mismatch compared to the significant mismatch of 20% with GaAs.

Tsuchiya et al. [47] grew thick cubic GaN layers on GaAs (001) with a hybrid growth method of halide vapour phase epitaxy with a cubic GaN buffer layer put down by metal organic MBE (MOMBE). It was found that the incorporation of hexagonal inclusions increased exponentially with the growth time, the thickest layer at 10 µm having a hexagonal component of 40%. They attribute this increase to be proportional to the increase of the surface roughness with time as hexagonal material nucleates on the (111) plane of cubic GaN.

More recently Rüsing et al. [44] published an in depth study on defect formation in cubic GaN films grown on 3C-SiC (001) substrates by radio frequency plasma assisted MBE (pa-MBE). It was found that defect density in layers of thickness between 75 and 505 nm actually decreased with distance from the substrate interface as stacking faults on the (111) plane formed at nucleation sites annihilate as they intersect with one another. The surface roughness of the substrate is therefore important for achieving high purity cubic material. High resolution XRD and Raman spectroscopy showed no detectable hexagonal inclusions although the layers remained relatively thin. A newly developed unorthodox technique for the growth of cubic material involves the merging of two hexagonal-phase (0001) growth fronts at the right angle, this will result in the

proliferation of cubic (001) phase growth after the seam. Liu and Bayram [48] used nano-patterned grooves in Si (100) to create a hexagonal to cubic phase transition by metal-organic chemical vapour deposition (MOCVD).

Of the varying growth techniques MBE has been shown to reliably produce the material with the lowest fraction of hexagonal content [47] although it is limited in growth rate. In HVPE and MOVPE the higher growth temperature cause the metastable cubic phase to rapidly break down with increasing thickness even when grown on phase pure MBE grown buffer layers. The GaAs substrate is desirable as optoelectronic devices may be easily integrated with existing conventional GaAs-based electronic devices and it may be easily chemically etched to produce free-standing layers.

1.2.2 Growth of Cubic AlGaN

There exists less work published on the growth of cubic AlGaN, especially for high aluminium fractions of the alloy, and most of what does exist is centred on low dimensional heterostructures such as quantum wells incorporating only thin films as sustaining the zinc-blende growth conditions for bulk ternary AlGaN is considerably more challenging. There are only a few publications on the growth of very thin cubic AlN layers and no reports on the growth of bulk zinc-blende AlN crystals so far. However, progress continues to be made and a variety of growth substrates and techniques have been utilised in this field although the most common method is MBE growth.

Nakadaira and Tanaka [49] used MOVPE to put down 500nm thick c-$Al_xGa_{1-x}N$ epilayers on GaAs (100) in the range $0 \leqslant x \leqslant 0.51$. Photoluminescence emission intensity decreased rapidly as the aluminium content increased, attributed to an increase in impurities acting as deep-level recombination centers. A cubic GaN buffer layer was grown beforehand as is conventional to reduce the surface roughness and help initiate growth in the cubic phase. Higher temperature growth of the buffer layer has been found to be beneficial since the buffer layer can be a seed for either c-GaN or h-GaN and the increased migration of surface adatoms at higher temperatures help to decrease the prevalence of stacking faults during nucleation [50]. Kakuda et al. have studied growing cubic AlGaN directly on MgO (001) by pa-MBE [51]. The phase purity significantly decreased from 70% to 19% for c-AlGaN films with the Al contents of 9% and 34%, respectively. Again they theorise that at higher Al incorporation lower surface migration of Al adatoms leads to the generation of stacking faults on the (111)

facets. Without a cubic GaN buffer layer it was not possible to initiate cubic growth of AlN at all [52].

Controlling the rate of aluminium incorporation, which is very sensitive to the growth conditions, to get a uniform distribution both across the wafer and the duration of growth has been a challenge. This requires maintaining stoichiometric conditions and growth temperatures across time as well as across the length of the wafer. Researchers at the University of Nottingham grew cubic $Al_xGa_{1-x}N$ for the entire range of aluminium composition, i.e. $0 \leqslant x \leqslant 1$, on GaAs (001) substrates which were subsequently removed to yield free-standing material [53]. At higher Al concentrations the Al incorporation across the lattice became less uniform as the rate of inclusion becomes more sensitive to variations in the III\V ratio. It is well established in the growth of hexagonal AlGaN that aluminium fraction is inversely proportional to the available nitrogen flux as it affects the proclivity for preferential incorporation of Al over Ga [54].

Contrary to GaAs and AlAs there is a large difference in the lattice spacing for GaN and AlN making the mismatch with cubic substrates even more significant. Schupp et al. [55] were able to grow atomically smooth films of c-AlN with a surface roughness of 0.2 nm RMS on 3C-SiC substrates by flashing the substrate surface with Al and allowing it to desorb before growth. This eliminates amorphous surface oxides that can precipitate crystal defects. Growth was performed under one monolayer of Al coverage; it is well documented that exposing a c-AlN surface to nitrogen flux precipitates the formation of hexagonal clusters [27].

1.2.3 Doping Cubic Nitrides

Controlling the concentration of active dopants in any semiconductor material is important for achieving the desired specifications for electronic devices. Cubic nitrides in principle possess superior structures for efficiently incorporating dopants however there are barriers to high carrier concentration levels in the form of compensatory natural defects and the fact that in wide band gap materials many donors and acceptors are deep levels and therefore the thermally ionised populations are minimal. None of the crystals studied in this work are intentionally doped so this brief review will focus on unintentional impurities originating in MBE growth and their consequences.

Well studied is the phenomenon of yellow luminescence in III-nitrides originating

from a variety of point defects, impurities and donor-acceptor complexes. The lack of native substrates is typified by defect densities of $10^9 - 10^{10}/\text{cm}^2$ which have implications for recombination efficiency and leakage currents in optoelectronic devices. Bulk undoped gallium nitride typically has high n-type conductivity. This was originally attributed to the positively charged vacancy in the nitrogen sublattice, however it was shown that the formation energy of this defect was too large to account for such a carrier concentration. First principles calculations for wurtzite GaN showed the most likely extrinsic donor impurity is oxygen; wurtzite and the cubic phase show nearly equivalent formation energies and band structure for defects [56].

Oxygen is a shallow donor in GaN, and in c-$Al_xGa_{1-x}N$ for $x \leqslant 0.4$ [57], and is often present in high concentrations in nominally undoped material as a substitution on a nitrogen site. The probability of chemisorption of oxygen atoms increases with the Al content in AlGaN when oxygen atoms collide with the film surface during epitaxial growth because of the strong affinity between Al and O. Contrary to this fact is the result that a reduction in free electrons, n, is observed with increasing Al content as the gap state becomes more strongly localised [58].

Novikov et al. [59] have studied the unintentional inclusion of boron in AlGaN layers grown by pa-MBE. As the pyrolytic boron nitride cavity of the RF plasma source decomposes it releases free boron into the growth chamber where it is incorporated into the crystal. SIMS measurements revealed a fairly homogeneous distribution at a concentration of $\sim 1 \times 10^{18}/\text{cm}^3$ throughout the films. The most effective method to inhibit the inclusion of boron was to increase the nitrogen flow, effectively diluting the concentration of boron atoms in the nitrogen flux.

1.3 Picosecond Acoustics

The work presented in this thesis is focused on the acousto-optical interaction between photons and acoustic strain pulses in semiconductor bulk films and nanostructures with varying acoustical properties. The interaction is considered from two perspectives, namely, the generation of coherent acoustic phonons (CAPs) in semiconductor structures and their detection. The phonon frequencies of interest are in the sub-THz to THz range which falls within the region of the phononic spectrum characterised as heat. For decades the propagation of sound waves with frequencies in the kilohertz to megahertz range have been effectively applied for non-destructive ultrasound imaging

purposes by, for instance, piezoelectric transduction [60]. In this work the possibilities of generating frequencies beyond the limit of conventional high speed electronics and into the optical regime by means of picosecond acoustics are explored.

Picosecond acoustics was developed as an experimental technique in the 1980's when ultrafast pico/femto-second lasers had first become widely available. The inital publications on the topic were by Thomsen et al. [61, 62] and demonstrated the potential for the investigation of the structural, acoustic and electrical properties of thin films and microstructures. A short light pulse incident on an opaque material will be absorbed within a certain distance, resulting in the generation of a bipolar strain pulse by thermoelastic effects. A typical strain pulse is conventionally described by the derivative of the displacement and is composed of a variety of coherent phonons of differing frequencies. This wavepacket propagates in two directions away from the site of absorption changing shape as it does so due to attenuation and dispersion effects. More details of the mechanisms involved in the generation of coherent phonons will be given in further chapters.

In pump-probe spectroscopy a second, weaker, pulse of light deemed the probe is used to monitor the time resolved reflectivity, or transmittance for thin transparent films, of the sample as the strain pulse modifies it. Analysis of the resulting strain profile will show the times at which the strain pulse or successive echoes traverse sample interfaces or are reflected from the sample surface as demonstrated in Fig. 1.4. Initially this technique was applied for the non-destructive testing of thin films for the determination of various phenomena such as acoustic velocity and phonon-electron scattering by observing the period between and relative magnitude of successive strain pulse reflections [61–64]. This technique was modified for compatibility with samples transparent to the laser light by the introduction of an opaque transducer with which to generate the strain [64–66].

The above methods rely on the displacement of the free surface; further information may be gained by observing the interaction of the propagating strain pulse with the photoelastic properties of the sample. As the acoustic wave propagates a part of the probe pulse is scattered from it and interferes periodically with reflections from the surface and interfaces, giving rise to so-called Brillouin oscillations [67]. Later research started to investigate alternative mediums for generating and detecting strain such as multilayer structures e.g. quantum wells [68] and superlattices (SLs) [69, 70]. Reflec-

tion of the acoustic pulse from multiple abrupt interfaces with a significant change in density or elastic constants can give rise to a number of interesting effects such as phononic stop bands in a superlattice [70], while strain induced changes in low dimensional structures can be applied in electro-phononics, for instance modulating the energy levels of exciton transitions in quantum wells at high frequency [71].

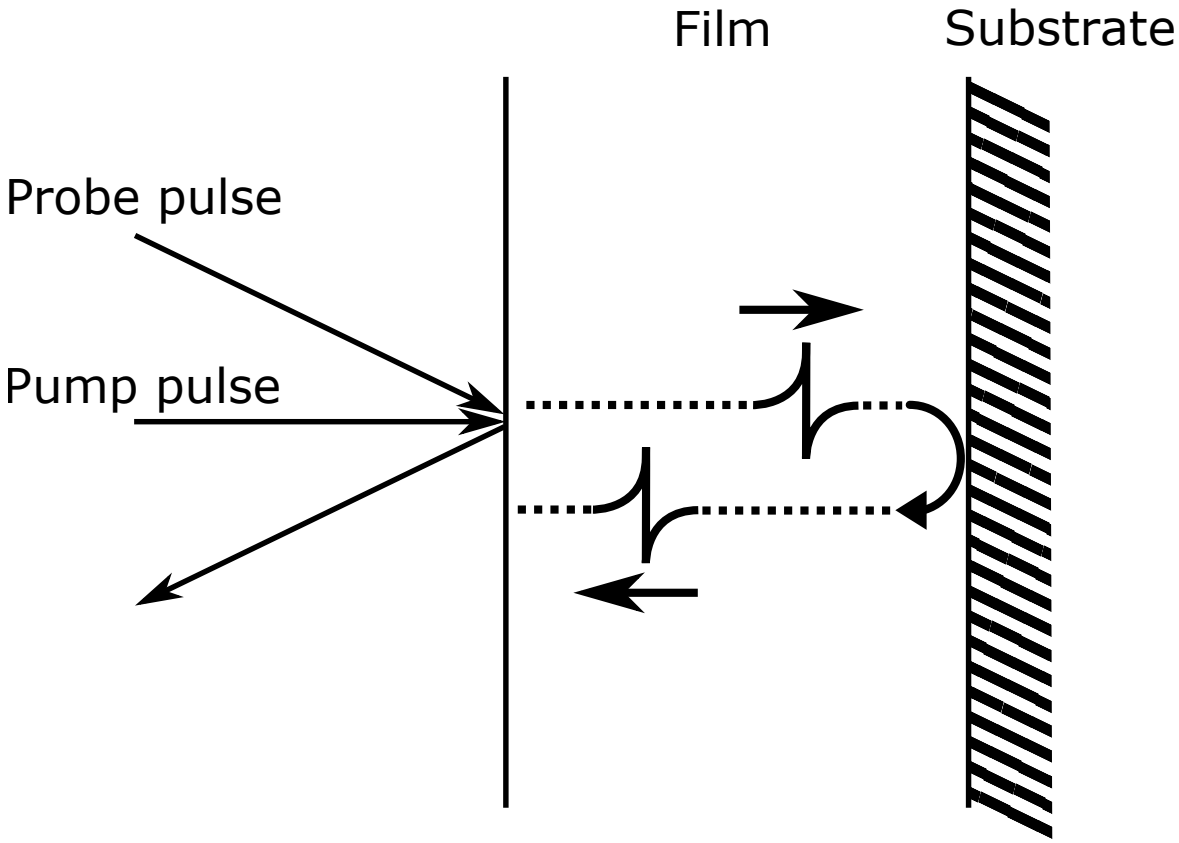

Figure 1.4: Schematic of the pulse-echo technique applied to an opaque thin film. The pulse is serially reflected inside the effective acoustic cavity leading to a periodic signal related to the round trip time.

1.3.1 Phonons in Cubic Nitrides

Hexagonal GaN as in other research areas has attracted most of the attention and the phenomenon of coherent acoustic phonons in nitride materials have been extensively studied [72–74]. Nitride semiconductor QWs [e.g. GaN/(InGa)N] are exceptionally efficient nanostructures for the generation and detection of very high frequency coherent acoustic phonons, up to 1.3 THz, as the strain induced piezo-electric field couples

strongly with the photo-excited carrier population [72].

Picosecond acoustic experiments with bulk zinc-blende nitrides are so far limited to the binary alloy of c-GaN. Moss et al. reported the first picosecond acoustic experiments for the characterisation of micrometre thick c-GaN layers epitaxially grown on (001) GaAs substrates, where the CAP strain pulse is generated by an Al transducer layer thermally evaporated onto the substrate. In this way the low temperature values for longitudinal sound velocity, elastic constants and refractive index were obtained by observing both dynamical thickness changes and oscillatory behaviour in the time-resolved optical reflectivity [75].

Subsequently He et al. investigated the thin film dynamics of free-standing cubic GaN membranes using an asynchronous optical sampling (ASOPS) technique [76]. Back etching of the GaAs substrate was used to produce the membranes released from the interfacial strain. These membrane structures are interesting due to their potential applications as optomechanical resonators as well as their usage in more fundamental research. By simultaneous observation of the high frequency Brillouin and lower frequency dilatational modes the thickness of the film was measured and the deformation potential for GaN was found to be positive (the sign convention is dictated by whether we are referring to positive hydrostatic pressure, as in this case, or the equivalent negative strain).

There exist well established techniques based on exploiting the transduction of acoustic strain by embedded QWs, the variation in band structure between the well and barrier meant that phonon pulses could be exclusively generated in the QW and detected at the sample surface. Czerniuk et al. used cubic GaN QWs sandwiched beteween c-$Al_xGa_{1-x}N$ barrier layers as detectors for propagating CAP pulses [68]. They indicate towards the potential for strain induced modulation of vertical laser structures incorporating nitride quantum wells. Similar experiments are undertaken in this work and a report of the results is given in Chapter 5.

1.4 Motivation for Work and Thesis Outline

The motivation behind this work is twofold. One aspect focuses on the application of picosecond ultrasonics as a tool for the investigation and characterisation of the photoelastic properties of zinc-blende nitride materials, in addition to investigating

methods for the high-speed modulation of UV light. The other is to examine strain generation using cubic nitride microstructures as a medium for the generation and detection of coherent acoustic strain.

The structure of the thesis is as follows. In Chapter 2 the reader will be briefed on the theory governing the interactions of thermal phonons in semiconductor structures. Chapter 3 gives detailed descriptions of the experimental techniques employed in the course of this thesis as well as covering the specific parameters for material growth. The fourth chapter presents results of picosecond acoustic experiments on bulk and free standing c-AlGaN films. In the fifth chapter single GaN quantum wells and GaN/AlN are used as transducers of high frequency longitudinal coherent phonons. Finally the arrived at conclusions are discussed along with the potential further work that remains to be done.

Chapter 2

Background Theory and Research Summary

The experiments described in this thesis rely upon the generation and detection of high frequency phonons in semiconductor structures. The generation, propagation and detection mechanisms of these coherent acoustic phonons are discussed in detail in this chapter. Specifically, the thermoelastic and deformation potential generation of strain in semiconductors via electron-phonon coupling processes will be considered along with a mathematical description of the initial strain profile. The effects of attenuation, dispersion and reflection will be considered as the strain pulse evolves in time. A summary of the mechanisms involved in the optical detection scheme of acoustic strain is presented, before an analysis of the confined modes created in the low dimensional films and heterostructures which have been investigated in this work.

2.1 Generation of Coherent Phonons

In an equilibrium crystalline solid the atoms are constantly oscillating in a simple harmonic motion with random phase. Because of the electrostatic forces linking the constituent atoms of the crystal the perturbation of one atom, which alters the charge distribution, also exerts a force on its nearest neighbours. An ultrafast laser pulse can be used to initiate collective in phase motion of atoms in the crystal lattice which we refer to as coherent phonons.

There exist alternative techniques, other than optical excitation, for the generation of strain pulses in semiconductor structures such as stimulated emission by electrical bias using the Wannier-Stark ladder effect or sequential tunnelling model [77, 78]. However such techniques are not considered here, as the sole method used for the

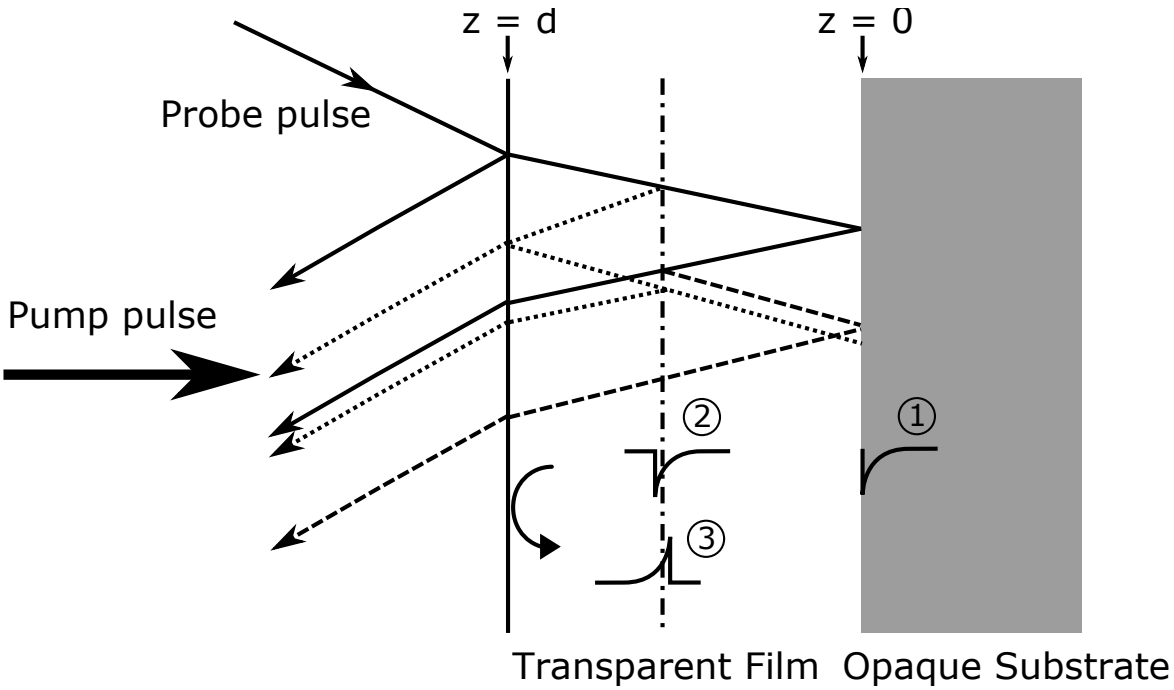

Figure 2.1: Schematic of the pump induced strain pulse in a transparent film after absorption in an opaque substrate and the subsequent multiple reflection ray diagram for the optical probe. The vertical dashed-dotted line represents the localised position of the strain pulse. The time evolution of the acoustic pulse is also shown: 1. Initial stress profile in the substrate at $t = 0$; 2. Propagation of unipolar acoustic pulse in thin film; 3. Reflection and inversion of acoustic pulse from the film-air interface.

generation of strain is surface and sub-surface heating as a response to optical absorption. An understanding of the mechanisms involved in the transduction of light to acoustic strain will be beneficial to the understanding of the experiments detailed in further chapters. A macroscopic description will be given, considering the case for the absorption of a light pulse within a short distance of GaAs, which is sufficient for the purposes of this thesis. A more detailed microscopic analysis is given by Ruello et al. [79]. There are a number of electron-phonon coupling mechanisms that may function in mediating the opto-acoustic conversion process. In this section only the relevant processes are reviewed, those that rely on piezoelectric or polar behaviour such as electrostriction are not covered.

2.1.1 Thermoelasticity

Consider the experimental situation of an ultrafast laser pulse, full width at half maximum (FWHM) duration of less than 1 ps, incident on an opaque substrate (GaAs) after passing through a transparent thin film (GaN). It illuminates an area of the substrate with fluence W and is absorbed within a distance ξ, which is assumed to be much less than the film thickness, transferring energy to the surface and sub-surface layers in the direction of photon propagation z. The corresponding temperature increase in the illuminated region by depth is [62, 64],

$$\Delta T(z) = \frac{(1-R)W}{C\xi} exp(\frac{z}{\xi}) \tag{2.1}$$

where R is the total optical reflectivity and C is the specific heat capacity per unit volume. The absorption length of the transducing material is given by,

$$\xi = \alpha^{-1} = 4\pi\kappa(\lambda)^{-1} \tag{2.2}$$

where α is the absorption coefficient and $\kappa(\lambda)$ is the imaginary part of the refractive index associated with wavelength λ. Assuming for the moment that the temperature rise is instantaneous, as the time-scale for thermal relaxation is much shorter than the time required for phonons to propagate along the optical absorption length, this establishes an isotropic thermal stress denoted by,

$$\delta\sigma = -3B\beta\Delta T(z) \tag{2.3}$$

where B is the material bulk modulus and β is the linear thermal expansion coefficient. The generated stress is hydrostatic and compressive for positive β and $\Delta T(z)$. We have assumed thus far that the material is elastically isotropic and that the heating is instantaneous and approximately uniform at the surface and subsurface levels, an assumption that can be safely made despite the Gaussian energy profile of the pump pulse due to the relative width of the beam spot, $\sim 100\,\mu$m, compared to the thickness of the studied films which are of the order of hundreds of nanometres. Consequently the atomic displacement u along the x- and y-coordinates is consistent on a planar basis and, given that the strain is the derivative of the displacement, it must equal zero [61]. It then follows that $\Delta T = \Delta T(z)$ is a function dependent only on the depth z and the only non-zero component of the strain tensor is η_{zz}. Hence the equations of

elasticity are established in the form [62, 80],

$$\sigma_{zz} = \rho_s v_s^2 \eta_{zz} - 3B\beta\Delta T(z), \tag{2.4}$$

$$\frac{\partial \sigma_{zz}}{\partial z} = \rho_0 \frac{\partial^2 u_z}{\partial t^2}, \tag{2.5}$$

$$\eta_{zz} = \frac{\partial u_z}{\partial z}, \tag{2.6}$$

where v_s is the longitudinal acoustic (LA) velocity and ρ_s the density in the substrate. η_{zz} and u_z are the strain and displacement in the z-direction respectively. The initial conditions are such that for $t < 0$, stress, strain and displacement are zero everywhere and the elastic boundary conditions requiring that $\sigma_{zz} = 0$ at $z = 0$ as there can be no restoring force at the free surface. Solving for the strain induced in the transparent film after it has been transmitted from the substrate [65],

$$\begin{aligned} &\text{for } z < vt, \ \frac{\eta}{\eta_0} = exp\left[\frac{(z - v_f t)}{\zeta_f}\right] \\ &\text{for } z \geq vt, \ \frac{\eta}{\eta_0} = 0 \end{aligned} \tag{2.7}$$

where $\zeta_f = \zeta(v_f/v_l)$ is the modified strain pulse length on transmission to the film, v_f and v_l are the film and substrate sound velocities and z is the distance from the film-substrate interface (see Fig. 2.1). The profile of the wavepacket is a unipolar truncated exponential of the same shape as the spatial absoprtion of the light pulse as shown in Fig. 2.2(a). This is unlike strain generated at a free surface, such as with a metal transducer, where reflection at the metal/air boundary produces an asymmetric bipolar strain pulse [66, 81]. Transmission across an interface is governed by acoustic mismatch theory such that the strain reflection r and transmission t coefficients are, respectively,

$$r = \frac{Z_f - Z_s}{Z_f + Z_s}, \tag{2.8a}$$

$$t = \frac{2Z_f}{Z_f + Z_s}, \tag{2.8b}$$

assuming that transmission is independent of frequency. $Z_f = \rho_f v_f$ and $Z_s = \rho_s v_s$ are the corresponding acoustic impedances of the film and substrate. The strain pulse

undergoes a phase change of π radians on reflection, under the condition that $r < 0$ i.e. $Z_f < Z_s$. The phase change has the effect that tensile strain becomes compressive and vice versa. Expressions describing the strain pulse after further reflections may be obtained by adding terms in an iterative manner [65]. The amplitude of the initial strain pulse η_0 injected into the film is given by,

$$\eta_0 = -\left[Z_f/(Z_f + Z_s)\right](\frac{\delta\sigma}{\rho_f v_f^2}). \tag{2.9}$$

The amplitude of the strain pulse η_0 is proportional to the thermal expansion coefficient β with $\eta_0 < 0$ corresponding to a compressive wave.

2.1.2 Generated Phonon Spectrum

It is beneficial to understand how the spectral transformation functions relate the frequencies contained within the optical pulse to the acoustic frequencies generated within the strain pulse. If we take the origin of the spatial coordinates as the leading edge of the strain pulse, then the Fourier transform of this propagating wavepacket is [80]

$$\int_{-\infty}^{\infty} \eta(z,t)exp(i\omega t)\mathrm{d}t = \eta_0 \frac{i\omega}{\omega^2 + 1/\tau^2} \tag{2.10}$$

where ω is the acoustic angular frequency, the characteristic time $\tau = \xi/v$ is equal to the duration of propagation for longitudinal acoustic phonons along the optical absorption depth. Fig. 2.2(b) illustrates the calculated modulus of the frequency spectrum produced for an excitation energy of 375 nm (3.3 eV) incident on GaAs, in which case $\xi \approx 15\,\mathrm{nm}$ and $v_s = 5\,\mathrm{km\,s^{-1}}$.

It follows from Eq. (2.10) that for optimal excitation of high frequency phonons the material or pump wavelength must be chosen such that the imaginary part k_g'' of the optical wavenumber $k_g = k_g' + ik_g''$ is maximised and thus the light is weakly penetrating. The index "g" here refers to the generation process. Providing that supersonic diffusion of energy is inhibited, the spectrum of efficiently generated phonons may extend to frequencies where the acoustic wavenumber is equal to the optical intensity absorption coefficient i.e. $k_a(\omega) = \omega/v_s = \alpha = 2k_g''$ [82].

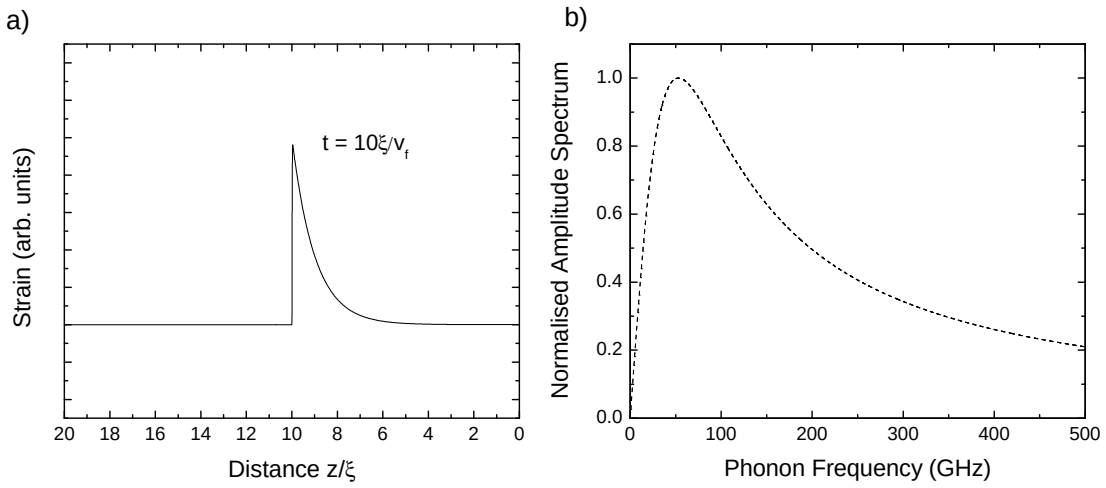

Figure 2.2: (a) Plot of the longitudinal strain pulse η_z injected into the transparent film after optical absorption in a depth ξ propagating with velocity v_f (b) Plot of the calculated phonon frequency distribution present in a strain pulse excited by ultrashort light pulse of photon energy 375 nm $\xi = 15$ nm.

2.1.3 Deformation Potential

In the previous section the effects of thermal and carrier diffusion on the profile of the generated strain pulse were neglected, if these are accounted for the strain pulse is broadened as the generation of strain is distributed in both time and space. Furthermore the strain produced in semiconductors depends additionally on the free carrier density in the form of a deformation potential contribution [83]. The deformation potential is the term which relates the variation in the electronic band structure to strain in the solid. The interatomic forces are totally dependent on the electronic distribution, thus if this is altered the equilibrium position in the lattice is equivalently changed, leading to crystal deformation and hence phonon emission.

Here we analyze the effects of an expanding e-h plasma in GaAs on the deformation potential stress profile. Previously we considered the effects of thermoelastic strain imparted to the lattice by the band relaxation of excited carriers, in semiconductors these excited e-h pairs may have a direct impact on the photoinduced stress which is directly proportional to the local population of photoexcited carriers [80]. It has been shown that the relaxation of excited carriers in bulk GaAs to the band edge occurs within around 100 fs or near instantaneously in the linear regime i.e. for moderate pump fluences [84]. The rate of non-radiative recombination of electron-hole (e-h) pairs, which results in the thermalisation of the band gap energy to the lattice, is strongly linked

to the e-h plasma density. At higher pump fluences the effect of the thermoelastic contribution may be more closely related to time dependent carrier diffusion processes as non-radiative recombination mechanisms, such as Auger recombination, begin to dominate. Consequently the thermoelastic strain profile will be altered. Eq. (2.4) must then be modified to include an additional term describing the electronic stress,

$$\sigma_{zz} = \rho_s v_s \eta_{zz} - 3B\beta\Delta T(z) + \sum_k \frac{\partial E_k}{\partial \eta_{zz}} N_k \tag{2.11}$$

where $\partial E_k/\partial \eta_{zz}$ is the deformation potential and N_k is the carrier density for a carrier of energy E_k and wave vector k. The deformation potential can be the primary mechanism in semiconductors, especially at lower pump fluences or for photon energy comparable to the band gap, as the carrier lifetime is comparable to the duration of the strain pulse. It has been shown that for GaAs (100) excited at a wavelength of 375 nm the electronic stress is 6 times greater than the thermoelastic contribution and of the same sign [85].

In the static regime it is assumed that the phonons are generated only from the point of optical absorption. In comparison to the static regime, if the initial velocity of the e-h plasma exceeds the speed of longitudinal sound i.e. $v_{eh} > v_s$, then the leading edge of the strain pulse cannot escape the expanding plasma until such time as $v_{eh} \leq v_s$. Therefore in this *supersonic* regime the trailing edge of the strain profile is drawn out and has smaller amplitude creating a strongly asymmetric strain profile. A representative sketch indicating the respective profiles for the points of origin for emitted phonons in the two regimes is shown in Fig. 2.3. The following equations are derived from work done by Young et al. [81] modelling picosecond strain pulses produced by optical excitation at the free surface of bulk GaAs. Moving forward the assumption is made that carrier diffusion across the GaAs/c-GaN boundary is negligible owing to the band discontinuity at the interface. Although the literature has proposed minimal conduction band offset, transport measurements across this interface have shown rectifying behaviour with very weak temperature dependence suggesting a tunneling process as the primary mechanism for conduction [86].

Considering only the e-h-phonon deformation potential, one can write the inhomogeneous one-dimensional wave equation for the particle displacement u is [81, 85]

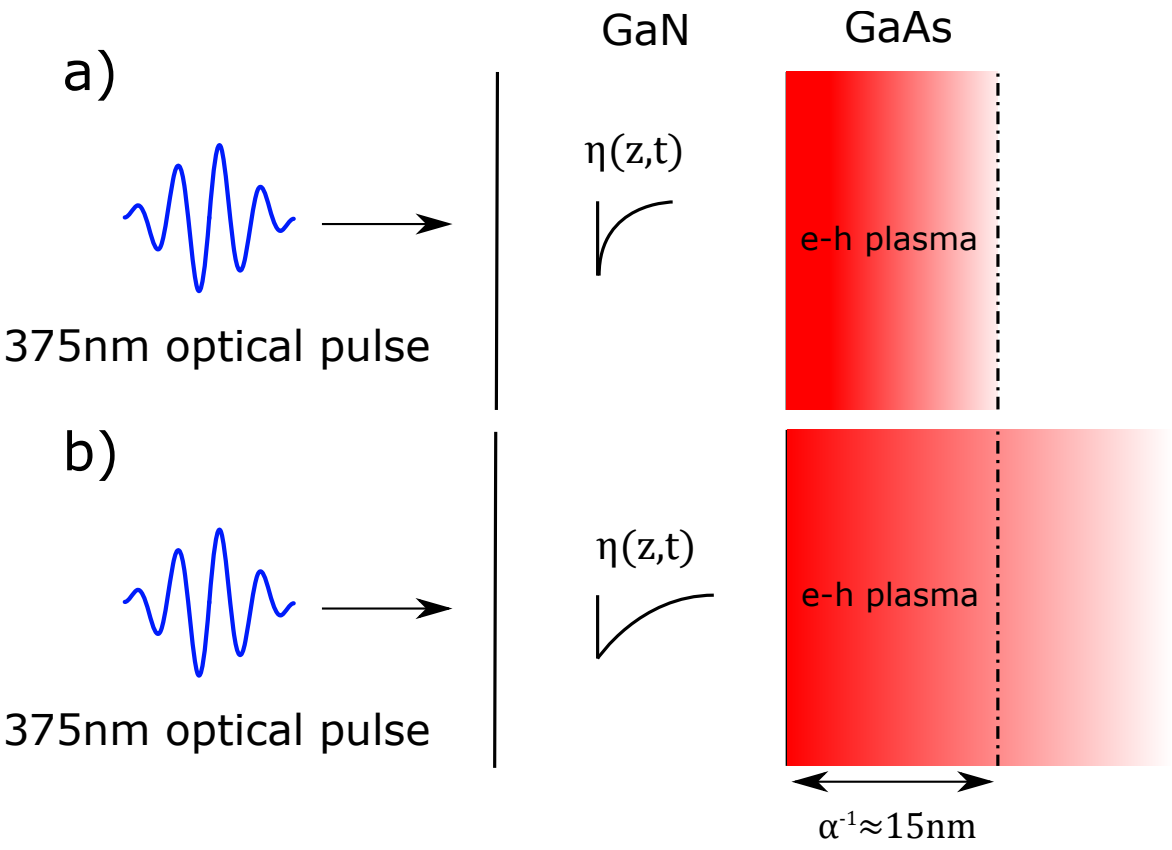

Figure 2.3: Representative schematic of the generation of strain pulses in the a) static and b) supersonic regimes when the optical excitation is absorbed within a length α^{-1}. As the e-h plasma initially expands faster than the speed of longitudinal sound the effective profile for strain transduction is altered resulting in a strain pulse with reduced maximum amplitude and an elongated trailing edge.

$$\rho\left(\frac{\partial^2 u_z}{\partial t^2} - v_s\frac{\partial^2 u_z}{\partial z^2}\right) = \Xi_{DP}\frac{\partial n_{eh}}{\partial z} \tag{2.12}$$

Where Ξ_{DP} is the deformation potential constant and n_{eh} is the concentration of the e-h plasma. The spatial-temporal evolution of this plasma field can be understood by looking at the initial population generated by a femtosecond laser pulse, the subsequent diffusion of the plasma and its reduction due to e-h pair recombination [79].

$$\frac{\partial n_{eh}}{\partial t} = D\frac{\partial^2 n_{eh}}{\partial z^2} + \alpha N\delta(t)exp(-\alpha z) - \frac{n_{eh}}{\tau_R} \tag{2.13}$$

where D is the ambipolar diffusivity, τ_R is the e-h pair recombination lifetime, α is the optical absorption coefficient and $\delta(t)$ is a Dirac delta function approximating the

femtosecond laser action as instantaneous. $N = (1 - R)W/h\nu$ is the sheet density of absorbed photons as a proportion of total laser fluence W absorbed per unit photon energy $h\nu$. The boundary conditions applied in this geometry are such that there is zero e-h plasma diffusion beyond the edge of the GaAs: $\frac{\partial n_{eh}}{\partial z} \underset{z=0}{=} 0$, and the plasma density is zero at infinite distance from the GaAs interface: $n_{eh} \underset{z=\infty}{=} 0$. It is subsequently possible to find the solution to the frequency spectrum and temporal profile of the strain pulse by transforming the partial differential Eqs. (2.12) and (2.13) into ordinary differentials and algebraic equations by Fourier transforming over time and subsequently taking the Laplace transform over the coordinate z. Such an analysis is outside the scope of this work, however the full derivations may be found elsewhere [81, 87] .

At the Γ-point in zinc-blende semiconductors there are four deformation potentials. Two correspond to the hydrostatic deformation potentials for the conduction band minimum and valence band maximum associated with the relative volume dilation [88]. The remaining two are valence band potentials dependent on shear strain in the [111] and [100] directions respectively. The deformation potential may be simply expressed as the result of the summation of the independent hydrostatic deformation potentials for the conduction and valence bands. This gives the expression

$$\frac{\mathrm{d}E_g}{\mathrm{d}\eta} = \Xi_{DP}. \tag{2.14}$$

Where the absolute values for each are known it is found that the conduction band potential is about ten times larger, that is, the effect is much stronger for electrons. For this reason where carrier mobility is rectified there may be significant variation in the shape of the resultant acoustic pulse. Although there are numerous methods for determining the value of the deformation potential experimentally, no such data exists for the deformation potential in zinc-blende GaN. An average of theoretical studies yields a value of $\sim -7.4\,\mathrm{eV}$, which is on the order of most typical direct band gap semiconductors [24].

2.1.4 Ripple Effect

In semiconductor nanostructures an important mechanism for electron-phonon coupling is the ripple effect whereby a strain pulse traversing the interfaces modulates the spatial dimensions of the structure resulting in a perturbation of the free carrier wave functions. The ripple effect has been observed to dominate over the deforma-

tion potential for quantum dots with a radius of the order of 50 nm, an effect which increases by orders of magnitude with the reduction in dimensionality [89]. In other low dimensional devices such as quantum wells the acoustic wave will cause a time variation in the effective well width, and hence a time variation in the quantised electron energy levels within. In the following analysis we focus on the dominant electron contribution. For a quantum well the magnitude of the shift in energy levels can be understood by looking at the expression for the ground state energy as it depends on the well thickness d_w [90].

$$E_1 = \frac{\hbar^2 \pi^2}{2m^* d_w^2}, \tag{2.15}$$

where m^* is the effective mass for the conduction band electrons in cubic GaN well $m^* \approx 0.15 m_0$ [20]. The derivative is taken with respect to the width of the well,

$$\frac{\mathrm{d}E_1}{\mathrm{d}d_w} = \frac{-\hbar^2 \pi^2}{m^* . d_w^3} \tag{2.16}$$

Consider now a strain pulse of maximum amplitude ε_m, propagating through the well structure. The variation in the well thickness due to the presence of the pulse is $\mathrm{d}d_w = \varepsilon_m d_w$. Substituting into Eq. (2.16) the shift in ground state energy is,

$$\mathrm{d}E_1 = \frac{-\hbar^2 \pi^2}{m^* d_w^2} \varepsilon_m \approx \Xi_R, \tag{2.17}$$

where Ξ_R may be understood as the ripple effect coupling constant. Evaluating this equation for a c-GaN quantum well of width $d_w = 5\,\mathrm{nm}$, $\Xi_R \approx 0.2\,\mathrm{eV}$ which is more than an order of magnitude lower than the contribution from Ξ_{DP} and may therefore be considered negligible.

2.2 Coherent Phonon Propagation

During the strain pulse propagation as it perturbs the crystal lattice the shape of the pulse is itself subject to anharmonic and dispersive effects which accumulate for the duration of travel. Such effects are significant at higher pump fluences as they have a non-linear relationship with increasing strain amplitude and frequency of the spectral components. Consequently the strain pulse propagation is non-linear and the amplitude, temporal profile and characteristic frequency content of the pulse are

not necessarily conserved over time. The relevant factors in understanding the time evolution of the CAP pulse are considered in detail in this section.

2.2.1 Phonon Attenuation

Attenuation of coherent phonons may arise in crystalline semiconductors by a variety of extrinsic and intrinsic processes. The extrinsic mechanism is dominated by phonon-scattering at lattice imperfections and impurities, including natural isotopes, which act to reduce the mean free path of the phonons and the process is temperature independent [91]. In high quality crystals this impurity and defect scattering will be minimal, however in cubic GaN the defect densities are routinely on the order of $10^9 - 10^{10}\,\mathrm{cm}^{-2}$ which is enough to make a significant impact on the phonon coherence length. For the ternary alloys it is simplest to imagine the material properties as an average of the properties of the two binary constituents. However where there is considerable inhomogeneity in the alloy concentration, phonons may be scattered as they enter a region of different mass and elastic constant. Moreover, interface surface roughness at a heterojunction boundary such as GaAs/GaN may scatter the incident phonons resulting in a loss of coherence providing the surface roughness is on the order of the phonon wavelength [92].

The intrinsic acoustic loss is primarily as a result of incoherent scattering with the background population of thermal phonons [93–95]. This interaction occurs in one of two regimes depending on the acoustic frequency and temperature conditions. In most applications CAPs are subthermal ($\hbar\omega \ll k_b T$) and the angular frequency ω is significantly less than the thermal phonon lifetime τ_{th}. This is equivalent to the condition $\omega\tau_{th} \ll 1$ and corresponds to the case where the wavelength of the acoustic phonon is much longer than the mean free path of the thermal phonon. In this instance a macroscopic relaxation damping model of attenuation is valid, whereby the acoustic wave couples elastically to the thermal phonon population, as their frequency is strain dependent and shifted from equilibrium by the acoustic pulse. The attenuation is then linked to an irreversible increase in entropy associated with the thermal phonon collisions as the system returns to equilibrium [93].

For ultrasonic waves with spectral components at high frequencies such that $\omega\tau_{th} \gg 1$ the relaxation damping will be independent of phonon frequency and a quantum mechanical three phonon (one acoustic and two thermal phonons) process predomi-

nates, the so-called Landau-Rumer mechanism. This model was further developed by Herring who considered the collisions allowable under the crystalline anisotropy and showed that the attenuation factor varies with frequency and temperature according to $\omega^a(k_BT/\hbar)^{5-a}$, where $a = 2$ for cubic crystals. This dependence was confirmed for hexagonal GaN at 470 and 940 GHz [95].

As a result of these behaviours picosecond ultrasonic experiments are often carried out at cryogenic temperatures in order to eliminate thermal noise and attenuation effects, especially when the strain pulse is required to traverse significant distances before detection [75, 81]. As in this case the optically generated acoustic phonons are not required to be particularly long lived, for experiments detailed in this thesis, attenuation is not a substantial factor in the results.

2.2.2 Non-linear and Dispersive Propagation

High amplitude strain pulses may no longer be adequately described by the equations of motion derived previously [cf. Eq. (2.5)]. These equations are based on a model with the atoms of the lattice as hard spheres and the interatomic forces represented as springs connecting them, obeying Hook's law, that linearly relates stress and strain. These expressions no longer apply in the limit case of strong deformation (displacement). Moreover, as the wavelength of the phonons approach the length scale of the crystal unit cell, anharmonic effects predominate due to the periodicity of the lattice. The consequences of this may be observed in the phonon dispersion relation for zinc-blende GaN seen in Fig. 2.4 illustrating the acoustic and optical phonon branches in the reduced zone scheme with $|q| = ka/2\pi$. The phonons are classified by their polarisation: if the displacement is parallel or perpendicular to the direction of the phonon wavevector $\vec{q}$, then the phonons are denoted longitudinal and transverse, respectively. Crystals with more than one atom per primitive unit cell may experience vibrations where neighbouring atoms are oscillating in anti-phase. These are referred to as optical phonons, in contrast to acoustic phonons where adjacent atoms move in phase with each other, because they interact with electromagnetic fields more readily. The relevant branches in this work are the longitudinal modes in the [100] orientation, which correspond to the leftmost panel between the Γ and K-points.

The propagation speed of a phonon is $\frac{\partial\omega}{\partial k}$. Close to the zone center where $q \ll \pi/a$ the longitudinal acoustic (LA) branch obeys an approximately linear dependence be-

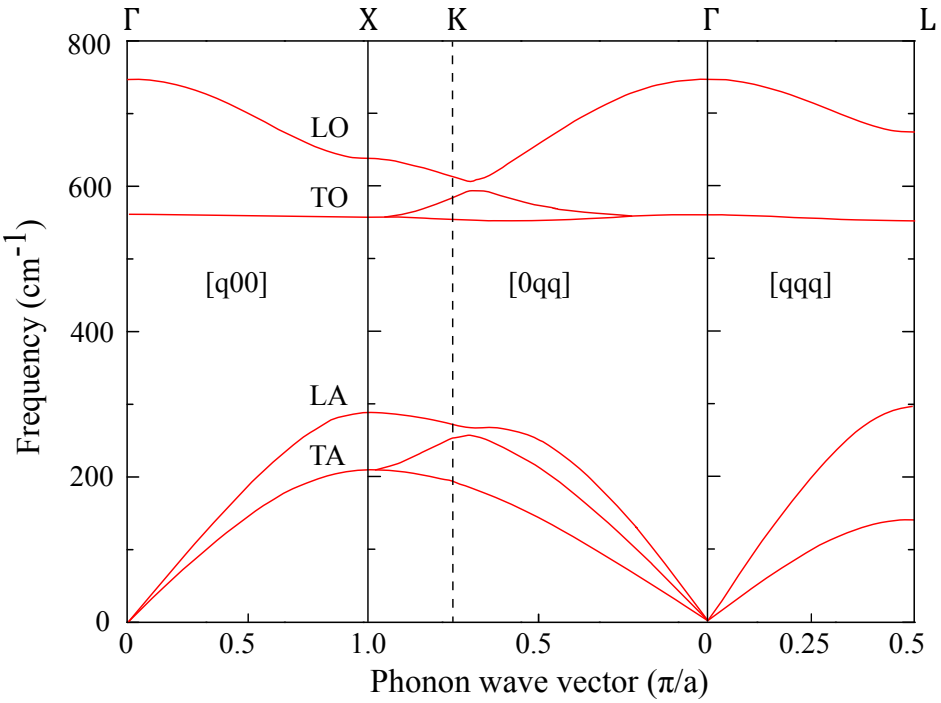

Figure 2.4: Zinc-blende GaN dispersion curve along several high symmetry directions in the first Brillouin zone plotting phonon wavenumber versus wavevector after Zi et al. [96]. Both optical (O) and acoustic (A) branches are depicted with one longitudinal (L) and two transverse (T) branches each, in certain high symmetry directions the transverse branches are degenerate. As phonon propagation is solely along the [100] direction in this work, only the leftmost section of the diagram, between the Γ and K-points, is considered further.

tween frequency and wave vector such that $\omega_k = v_{LA}k$ where ω_k is the phonon angular frequency and v_{LA} is the longitudinal acoustic sound velocity. In the low frequency linear regime the group velocity is identical and so the phonons will not be subject to dispersion. Towards the boundary of the first Brillouin zone the gradient of the dispersion for both the LO and LA modes flatten out and the group velocity tends toward zero i.e. a standing wave is formed.

Introducing higher orders of strain tensor into Eq. (2.5), to account for finite deformation limits, leads to a modified equation of motion. Continuing to assume an isotropic medium as well as stress and displacement only along the z-axis, the solution is

$$\rho\frac{\partial^2 u_z}{\partial t^2} = \frac{\partial^2 u}{\partial z^2}\left(C_2 + \frac{\partial u}{\partial z}C_3\right) \tag{2.18}$$

where C_2 is a combination of second order elastic constants and associated with the linear propagation while C_3 also contains third order elastic constants and describes the non-linear propagation [97]. It then follows that the sound velocity is no longer consistent as it depends on the amplitude of the strain ($\eta = \partial u/\partial z$). In most solids the value of C_3 is negative leading to an increased and reduced speed of sound for compressive ($\eta < 0$) and tensile ($\eta > 0$) strain respectively. This non-linearity modifies the pulse shape and leads to frequency upconversion of the wavepacket spectrum where shockwaves form at the leading and trailing edges.

The experiments described in the fourth and fifth chapters of this thesis involve only the case for acoustic strain excited directly adjacent to, or within thin epitaxial films with moderate pump fluence. In such a case the propagation distance ($\sim$350 nm) is not sufficient for these non-linear effects to make a significant contribution to the results.

2.3 Optical Strain Detection

Conventionally strain is detected in the sample some time after generation through various optical techniques measuring the variation in apparent reflectivity or transmission. These techniques range from piezoreflectance measurements at the near surface of opaque materials [61, 62, 85] to interferometric reflectivity changes due to the interference of multiple reflections from propagating strain pulses [65, 75, 98]. Optical detection of the acoustic strain is an obvious development, as the generation of the strain already involves the use of femtosecond laser pulses and is sufficient to provide the requisite temporal resolution. As discussed previously in Section 2.1.2 the acousto-optic (AO) transformation functions are frequency dependent and so determine how efficiently different regions of the phonon spectrum couple to the intensity variation of the reflected probe beam. However, in the reverse case the sensitivity depends not on the penetration depth of the probe pulse but the spatial distribution of the laser electric field. Consequently the characteristic acoustic frequency ω_d is determined by the equivalence of the acoustic wave number $k_a(\omega) = \omega/v_a$ and twice the laser wavenumber $2(k_d'' - ik_d')$ where the index "d" refers to the detection process. Therefore in order to have a broad frequency bandwidth of AO detection it is necessary to maximise the probe optical wavenumber. Typically this is achieved by increasing the imaginary component k_d'' by utilising an optical probe quanta with high absorption coefficient.

Two characteristic time scales are established in the transient reflectivity response measured in the time domain. The first one is related to the time required for the strain pulse to traverse the laser probe penetration depth $\tau_d'' = (\omega_d'')^{-1} = (2k_d'' v_a)^{-1}$, while the second is equal to the time required for the acoustic pulse to cross the probe wavelength in the material $\tau_d' = (\omega_d')^{-1} = (2k_d' v_a)^{-1}$. The latter is the focus of interferometric experiments in this work and will be elaborated upon in the following section.

2.3.1 Photoelastic Effect

The photoelastic effect in semiconductors couples the strain in the medium to the optical properties of the material via a modification of the dielectric constant, and hence the optical refractive index. In perturbed crystal lattices there are numerous physical origins for this phenomena, such as shifting of the electronic band structure, spatial redistribution of the atomic orbitals or the piezoelectric effect. One important application is that strain may turn optically isotropic materials anisotropic, termed birefringent, and so the strain field in complex geometries may be analysed. The dielectric function is given by a second rank tensor ϵ_{ij} which is a 3x3 matrix. The strain induced change in the dielectric impermeability tensor (inverse dielectric function) due to strain, for photons of energy E, is mediated by the fourth rank Pockels photoelastic tensor $p_{ijkl}(E)$

$$\delta\left(\epsilon^{-1}(E)\right)_{ij} = \delta\left(\frac{1}{n^2(E)}\right)_{ij} = p_{ijkl}(E)\eta_{kl} \tag{2.19}$$

where η_{kl} is the strain tensor. The symmetry of the index ellipsoid in i and j, and the strain tensor in k and l limits the number of independent elements of $p(E)$. It reduces to a symmetric matrix with only three non-zero components for cubic semiconductors zinc-blende (Al)GaN and GaAs studied here. Moreover, these materials are optically isotropic and so ϵ becomes a scalar value. Given that the acoustic pulse only generates uniaxial strain η_{zz} in the [001] direction, the number of indices are further reduced such that only two photoelastic coefficients may adequately describe the change in refractive index. As the optical index perturbations due to the photo-elastic effect are relatively small Eq. (2.19) may be rearranged

$$\delta\left(n\right)_{ij} = -\frac{n^3}{2} P_{ijkl}\eta_{kl} \tag{2.20}$$

Thus the variation in the refractive index is directly proportional to the magnitude of the mechanical strain and providing that the relevant photo-elastic tensor elements are non-zero. In this work we investigate the time-resolved measurements of reflectivity arising from transient variations in the dielectric permittivity $\delta\epsilon$ with photon energies close to the band gap. Under these conditions where the variation in the complex index of refraction $n^* = n + i\kappa$, where n is the real part and indicates the phase velocity while the imaginary κ is the extinction coefficient and describes the attenuation of the electric field as it propagates, is mostly due to shifting of the electronic band structure the change may be approximated by

$$\delta\tilde{n} = \frac{\partial n^*}{\partial E}\frac{\partial E}{\partial \eta}\eta = \left(\frac{\partial n}{\partial E} + i\frac{\partial \kappa}{\partial E}\right)\frac{\partial E}{\partial \eta}\eta \tag{2.21}$$

where $\frac{\partial E}{\partial \eta} = \Xi_{DP}$ is the deformation potential [cf. Eq. (2.14)], while $\frac{\partial n}{\partial E}$ and $\frac{\partial \kappa}{\partial E}$ are the energy dispersions of the refractive index and the optical extinction coefficient respectively [68].

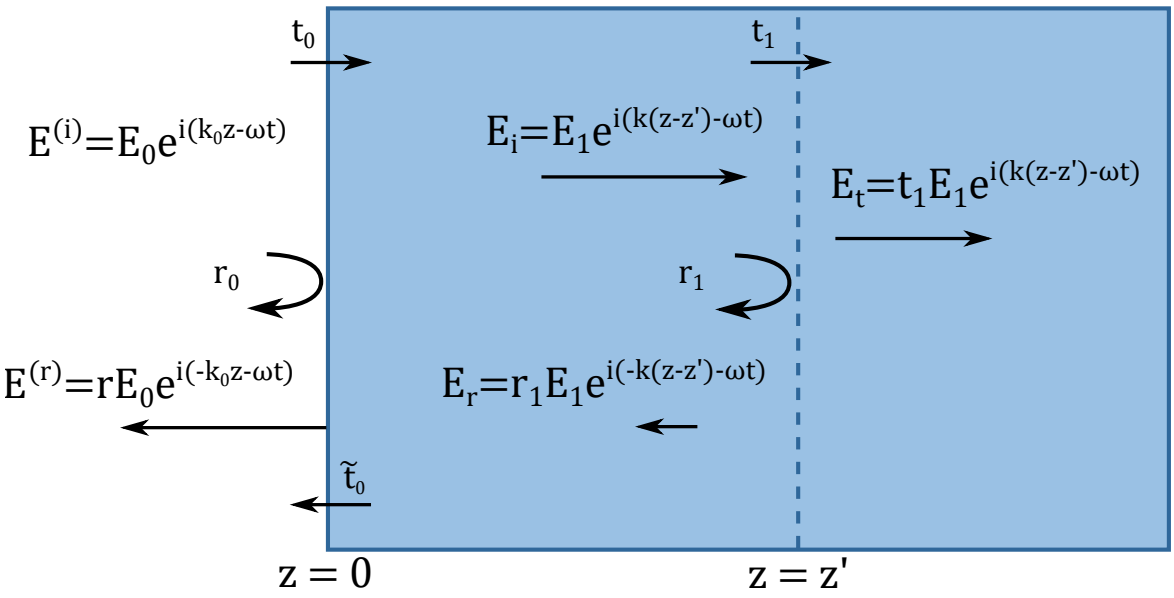

Figure 2.5: Diagram illustrating the electric fields present in an isotropic semiconductor with strain pulse at position $z = z'$ when a normally oriented monochromatic e-m wave with linear polarisation is incident.

To model the reflectivity response from a localised strain induced disparity in permittivity $\Delta\epsilon(z) \ll \epsilon$ consider a plane electromagnetic wave propagating at normal

incidence through a lossy dielectric medium as depicted in Fig. 2.5. When the strain is zero the electric field at position z and time t for the incident EM wave is

$$E^{(i)}(z,t) = E_0 e^{i(k_0 z - \omega t)}, \tag{2.22}$$

where ω is the optical angular frequency. The wave is subject to reflection at the film surface where the optical reflection and transmission coefficients are analogous to those described for the acoustic mismatch theory [cf. Eqs. (2.8a) and (2.8b)]. One simply substitutes the acoustic for optical impedance giving the Fresnel equations for the simplest case normal incidence ,

$$r_0 = \frac{k_0 - k}{k_0 + k} = \frac{1 - n - ik}{1 + n + ik}, \tag{2.23a}$$

$$t_0 = \frac{2k_0}{k_0 + k} = \frac{2}{1 + n + ik}, \tag{2.23b}$$

where $k = n^*\omega/c$ and $k_0 = \omega/c$ are the wave numbers in the medium and free space respectively. At normal incidence the fields are always perpendicular to the surface regardless of orientation and so there is no distinction between s- and p-polarisation. This generates reflected and transmitted waves

$$E^{(r)}(z,t) = r_0 E_0 e^{i(-k_0 z - \omega t)}, \tag{2.24a}$$

$$E^{(t)}(z,t) = t_0 E_0 e^{i(kz - \omega t)} = t_0 E_0 e^{i(knz - \omega t)} e^{-k_0 \kappa z}. \tag{2.24b}$$

It can be seen that the electric field undergoes an exponential decay as the wave travels in the layer, with decay constant equivalent to the attenuation coefficient. By solving Maxwell's equations inside the film where the dielectric constant varies by position the wave equation for normal optical incidence becomes

$$\frac{\partial^2 E^{(t)}}{\partial z^2} = -\frac{\omega^2}{c^2}\left[\epsilon + \Delta\epsilon(z,t)\right] E^{(t)}, \tag{2.25}$$

where ϵ is the dielectric constant in the unstrained material and $\Delta\epsilon(z,t)$ is the strain induced response. Solving first for the case where the strain induced variability in optical permittivity is simulated by a spatial δ-function at position $z = z'$ from the interface, let $\Delta\epsilon = F\delta(z - z')$. In the figure the electric field incident on the strain pulse

is defined such that the incoming electromagnetic wave is then partially reflected from this discontinuity. The reflection coefficient is obtained by the integration of Eq. (2.25) as

$$r_1 = \frac{ik_0^2}{2k} F. \tag{2.26}$$

For as long as $r_1 \ll 1$ one does not need to account for the multiple reflections between the film surface and the strain pulse. Part of this wave then crosses the interface again and contributes to the total reflectance, giving the total reflected electric field from the material surface

$$E^{(r)}(z,t) = rE_0 e^{i(-k_0 z - \omega t)} = (r_0 + t_0 r_1 \tilde{t_0} e^{2ikz'}) E_0 e^{i(-k_0 z - \omega t)}, \tag{2.27}$$

where $\tilde{t_0}$ is the transmission coefficient moving from the film into vacuum. Knowing the response for a single δ-function distribution in permittivity allows for the calculation of the contribution from a more general case by integrating the sum of many such functions. For arbitrary $\Delta\epsilon(z,t)$ the reflection coefficient r is

$$r(t) = r_0 + \frac{ik_0^2}{2k} t_0 \tilde{t_0} \int_0^\infty \Delta\epsilon(z,t) e^{2ikz} dz \equiv r_0 + \delta r, \tag{2.28}$$

where $\Delta\epsilon$ is related to the strain induced changes in the refractive index by

$$\begin{aligned} \Delta\epsilon\,(z,t) &= \Delta\,(\tilde{n})^2 \cong 2\tilde{n}\Delta\tilde{n} \\ &= 2(n+i\kappa)\left(\frac{dn}{d\eta} + i\frac{d\kappa}{d\eta}\right)\eta(z,t) = a \times \eta(z,t). \end{aligned} \tag{2.29}$$

where a is a coefficient proportional to the strain dependence of the optical constants. The strain pulse can itself be expressed in terms of its Fourier components η_q

$$\eta(z,t) = \int_{-\infty}^{\infty} \eta_q \exp[i(qz - \omega_q t)] \exp(-\gamma_q t)\, dq, \tag{2.30}$$

where ω_q and γ_q are the frequency and damping respectively of the component q. The absolute change in power reflectivity is

$$\Delta R(t) = |r_0 + \delta r|^2 - |r_0|^2 = 2Re\left(r_0^* \delta r\right). \tag{2.31}$$

Combining the above equations and solving for the time-dependent components of $R(t)$ then

$$\Delta R(t) = 2\pi r_0^* a \eta_K \exp(-i\omega_K t)\exp(-\gamma_K t) + \text{complex conjugate}, \tag{2.32}$$

where K is $2k$ [99]. From this derivation it can be seen that $\Delta R(t)$ is an oscillatory function of the separation in time t of the pump and probe pulses. These transient oscillations of the reflectivity intensity are termed Brillouin oscillations and have been well studied in c-GaN [75, 76]. Moreover, an important feature of this result is the fact that the reflectivity depends only upon one particular Fourier component η_K of the strain pulse. The temporal shape and duration of the strain pulse are inconsequential, for the observation of these harmonic signals the only requisite is the presence of phonons with wavenumber K in sufficient number.

2.3.2 Interface Displacement

In multilayered transparent structures there is another interferometric contribution that relates to the displacement of interfaces as the strain pulse propagates across them and into different layers, an effect first documented by Wright et al. [65]. The total reflectivity of the sample is the sum of all reflections from each interface, when these are shifted it results in a phase transition with respect to the other unperturbed reflections due to the change in effective optical length $\Delta\delta$. This becomes observable in the relative reflectivity response $\Delta R/R$ as a function of the modulation of various interference terms. The mathematical model put forward by Devos et al. [100] describes it in terms of the integral of the strain relative to the unperturbed structure.

$$\Delta\delta^{(d)} = n\Delta d = n\int_0^d \eta(z)dz \tag{2.33}$$

The integral of the strain is equivalent to the displacement, when a monopolar strain that is purely compressive (negative) or tensile (positive) enters a film it engenders a slight increase or decrease in the film thickness respectively as the integral is non-zero. Another factor affecting the optical path length, as described above, the strain induces a change in the local optical index by the photoelastic effect

$$\Delta\delta^{(n)} = \int_0^d \delta n(z)dz = \int_0^d \frac{\partial n}{\partial \eta}\eta(z)dz = \frac{\partial n}{\partial \eta}\Delta d \tag{2.34}$$

In general, both the photo-elastic effect and interface displacement impact the modulation of ΔR since the phenomena are interlinked and one cannot exist without the other. It is possible to tune the experimental conditions such that the reflectivity response is preferentially coupled to either one of the mechanisms by carefully selecting the optical wavelengths of the pump and probe.

2.4 Confined Coherent Acoustic Modes

In the previously described experiments, it is understood that the width of the strain pulse is significantly smaller than the film in which it propagates. If, however, the thickness of the layer is reduced to the order of the optical penetration depth, or vice versa, it becomes possible to observe the vibrations of quantised modes which correspond to a periodic variation in the whole of a film or discrete layer within the structure. These longitudinally confined modes are generally quantised in one dimension, the growth direction, as the layer thicknesses may be as thin as several nanometers or on the same length scale as the wavelength of GHz/THz phonons, while the area of the plane surface is typically on the order of square millimetres.

2.4.1 Membrane Thickness Oscillation

This section will briefly review the mathematics governing the mechanics of motion for the simplest case of a free standing single layer membrane, following the theory laid out in Ref. [101]. Phonon quantisation only takes place if the excited layer is strongly acoustically decoupled from the surrounding materials, therefore free-standing membranes are ideal for the detection of these longitudinally confined modes. The type of eigenmodes present are conditional on the acoustic mismatch at the boundaries, for a free-standing film or supported film with greater acoustic impedance (Z_f) than the substrate (Z_{sub}) i.e. $Z_f < Z_{sub}$, then the modes are analogous to those of an organ pipe with two open ends. If the film is acoustically softer than the substrate then the modes resemble those of an organ pipe with one closed end [102]. The order of the observed modes are also contingent on the detection process which will be unpacked shortly. After the excitation of the membrane the boundary conditions at the free surfaces produce standing waves, much like in an optical resonator, with the eigenmode

frequency, $f = mv/2d$, related to the phonon round trip time, where d is the film thickness, v the speed of sound and $m = 0, 1, 2, 3...$ an integer denoting the order of the mode. These confined longitudinal acoustic modes have been studied in supported films [102], free-standing membranes [76, 103, 104], and other acoustic cavities [105].

Consider a membrane bound by two free surfaces at $z = \pm z_0$ with respect to the centre plane of the membrane. When the membrane material is isotropic the equations of motion governing the thickness modes from the inhomogeneous 1D-wave equation [c.f. Eq. (2.18)] reduce to

$$C_{33}\frac{\partial^2 u_z}{\partial z^2} = \rho\frac{\partial^2 u_z}{\partial z^2}, \tag{2.35}$$

where C_{33} is the elastic constant mediating longitudinal stress and strain i.e. Young's modulus. For plane harmonic waves with a time factor of $e^{i\omega t}$ this becomes

$$\frac{\partial^2 u_z}{\partial z^2} + \frac{\rho\omega^2}{C_{33}}u_z = \frac{\partial^2 u_z}{\partial z^2} + \gamma^2 u_z = 0. \tag{2.36}$$

The solution to this equation is $u_z = Asin(\gamma z) + Bcos(\gamma z)$, where A and B are amplitude constants. The free surfaces are traction free so the boundary conditions require that $\sigma_{zz} = 0$ at $z = \pm z_0$ so the displacement becomes

$$u_z = Asin(\frac{m\pi}{2z_0}z),\ m = 1, 3, 5...,\ B = 0, \tag{2.37a}$$

$$u_z = Bcos(\frac{m\pi}{2z_0}z),\ m = 2, 4, 6...,\ A = 0. \tag{2.37b}$$

The surface displacement profile of the first four orders of thickness vibrations are depicted in Fig. 2.6. The odd modes correspond to a symmetric variation of the surface position with respect to the centre plane of the membrane parallel to the surface while the even modes designate vibrations antisymmetric to the middle plane. These vibrations are termed confined longitudinal acoustic phonon modes, thickness osciallations or dilatational modes. Thus, neglecting the photoelastic effect, only the odd modes affect the total optical thickness of the membrane and contribute to the transient interferometric reflectivity via constructive and destructive interference from the two free surfaces [76, 104].

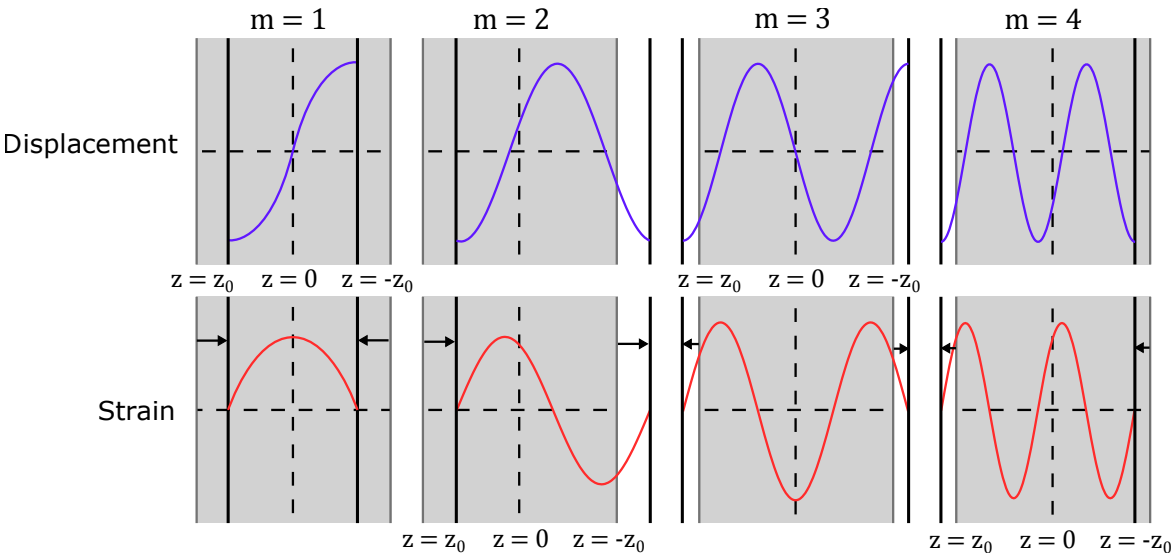

Figure 2.6: The displacement and strain profiles of the first four dilatational modes of a single layer membrane. The shaded area indicates the unperturbed position of the membrane. The blue and red sine-like curves signify the relative magnitude of strain and displacement respectively relative to the position of atoms on the z-axis.

2.4.2 Acoustic Properties of Superlattices

Following advances in miniaturisation techniques the growth of multilayer nanostructures with dimensions similar in scale to the optical wavelength of visible light has become viable. Photonic crystals contain regularly repeating regions with varying dielectric functions, thereby reducing the number of allowed states and defining regions of forbidden energy levels. The applications of photonic crystals have been extensively studied for use as optical mirrors, filters and resonators among others. The same concepts have been applied in the development and utilisation of phononic crystals [105]. In phononic crystals the relevant parameters governing the transmission and reflection at each interface are the mass density and speed of sound of each material. The simplest phononic devices are superlattices (SLs), which are structures made of periodic stacks of a bilayer with varying material properties. The electronic band structure then rearranges into a series of quantum wells and barriers with thickness d_w and d_b respectively. The acoustic field is modulated by the additional artificial periodicity, much longer than the inter-atomic spacing, of the lattice leading to a folding of the acoustic dispersion relation [c.f. Fig. 2.4] and the formation of a new mini-Brillouin zone defined by the period of the SL. Fig. 2.7 depicts the structure of an ideal superlattice and the resultant folding of the dispersion into a reduced zone scheme. Stop bands open

up at the mini-zone centre ($q = 0$) and boundary ($q = \pi/d$) due to Bragg reflections at interfaces in the structure, similar to formation of band gaps in the free-electron dispersion of semiconductors. Phonons with wavevectors satisfying these conditions are then forbidden from propagating in an ideal SL as they decay exponentially. It can be seen in the dispersion that the position of the gap is related to the dimensionality of the SL, while the size of the gap is defined by the magnitude of acoustic mismatch between the layers.

A consequence of the periodic variation of material properties is the possibility for preferential absorption of the optical pump in the well region of the SL, generating a strain profile varying with the period of the SL. In this way SLs become very effective AO transducers of quasi-monochromatic acoustic waves with frequencies defined by the SL period, which may extend well into the THz regime. The displacement field in the general case becomes a Bloch wave that satisfies the periodicity condition $u(z) = u(z + D)$. The availability of such high frequency coherent acoustic sources would be of considerable use in high resolution acoustic microscopy and phonon spectroscopy.

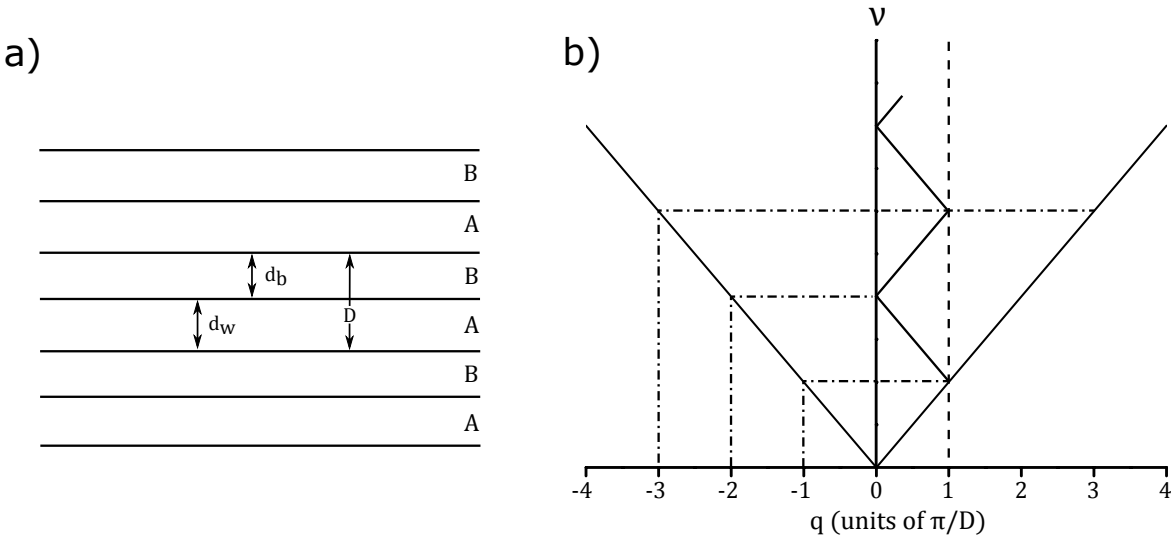

Figure 2.7: a) Schematic diagram of an ideal (infinite) SL made of alternating layers of materials A and B. The well and barrier widths d_w and d_b are shown as they relate to the SL period D. b) Folded dispersion for an arbitrary SL in terms of the period. Phonons with wave vector $m\pi/D(m = 1, 2, ...)$ meet the conditions for Bragg reflection in the SL.

The folded phonons have been extensively studied by Raman spectroscopy [106] and ultrafast optical pump-probe measurements [69,70,77]. Most of the research conducted to date has been on GaAs/AlAs system owing to the ease of manufacture. Chen et al. recorded the first observation of the folding of the acoustic branches of the phonon dispersion in hexagonal GaN/$Al_xGa_{1-x}N$ [106]. Measurements of the acoustic output of nitride superlattices propagating across millimetre distances were first performed using superconducting bolometers for detection [107]. A numerical analysis of cubic GaN/AlN nanowire phonon modes showed that it was theoretically possible to develop such a structure posessing the phononic bandgaps, despite the propensity of the characteristic nanowire mode sub-bands to be folded into the mini-Brillouin zone as well and straddle the gap [108]. Coherent detection of folded acoustic phonons in a cubic nitride superlattice, to the best of the authors knowledge, has yet to be reported. Further discussion of the elastic theory of semiconductor superlattices will be provided in Chapter 5.

Chapter 3

Sample Preparation and Experimental Techniques

This chapter details the experimental procedures and microfabrication techniques employed in the study of the cubic nitrides. Firstly the mechanism and general conditions for the optimal growth of the studied samples will be discussed, the dimensions of specific studied samples may be found in Chapters 4 and 5. Subsequently a general overview of the processes required for sample preparation will be given. Finally the details of the various experimental arrangements and methodology used to obtain the optical and elastic parameters will be provided.

3.1 Growth of Cubic Nitrides

For the purposes of sample growth in this work a commercial Veeco Instruments MODGEN II system was used by Prof. Sergei Novikov to grow nitride samples on the (001) face of GaAs substrates at the University of Nottingham by plasma assisted molecular beam epitaxy (pa-MBE). By first growing a small buffer layer of GaAs the presence of a residual flux of arsenic is used as a surfactant to initiate and encourage growth in the cubic phase. Work examining the surface reconstructions of cubic GaN layers grown under varying arsenic overpressure by Feuillet et al. [109] identified the process whereby the cubic phase growth is mediated by a continuous interchange between the mobile active nitrogen and arsenic atoms occupying the group-V position of the lattice. Considering that the relative bond strengths of gallium to nitrogen are higher than gallium to arsenic the nitrogen is expected to replace the arsenic which forms a dimer with another free arsenic atom and desorbs from the lattice. This process is dependent on a minimum growth temperature to increase the nitrogen mobility sufficiently to prevent arsenic inclusions.

It has been shown that the optimum operating conditions for the stable growth of the cubic nitrides requires an excess flux of group III elements. For both the binary and ternary compounds this was achieved with an excess flux of gallium. The excess gallium pools on the growth surface of the wafer in a film several monolayers thick, this film prevents oxidation of the growth surface and increases the mobility of aluminium as it is incorporated. As above the aluminium atoms preferentially bond with the active nitrogen from the Al-Ga liquid on the surface, therefore the inclusion rate of aluminium in the ternary compounds can be controlled only by varying the availability of the more mobile aluminium atoms. A cubic GaN buffer layer was put down before the cubic AlGaN to help initiate growth in the cubic phase. The GaAs substrate is maintained at a high temperature throughout growth during which time there is a potential for unintentional As doping due to diffusion. Secondary ion mass spectrometry (SIMS) and electron probe micro-analysis (EPMA) investigations concluded that the arsenic penetration was limited to the first hundred or so nanometers as a result of the initiation phase of cubic GaN growth which uses arsenic as a surfactant [53].

An HD25 RF activated plasma source was used as the source of activated nitrogen. Conventional solid effusion cells were used to provide the metallic group III elements aluminium and gallium. To reduce the proliferation of unintentional dopants and defect states the highest possible purity sources are used. Growth temperatures of approximately 700 °C were used and the temperature monitored with an optical pyrometer. Samples were studied during growth *in situ* using reflection high-energy electron diffraction (RHEED). Post growth analysis on MBE grown c-GaN films under 1 µm by XRD, although the technique is not sensitive to very low rates of inclusion, and RHEED measurements showed no characteristic results indicating the presence of hexagonal inclusions [38]. As the films studied in this work do not exceed the critical thickness it can be confidently stated that the hexagonal inclusions represent less than a fraction of a percent of the whole material studied.

3.2 Sample Processing and Preparation

Once the epitaxial layers have been grown they will all require some level of processing before experimentation can begin. All sample preparation and fabrication was performed by the author. The following section outlines the microfabrication processes required to be undertaken before the grown samples may be studied. Stages involv-

ing scribing, solvents, photoresists and developers, etchants, and other chemicals were performed on ventilated wet decks to prevent inhalation of toxic fumes and/or particles. Once finished the samples were affixed to 1 inch diameter copper plates with GE varnish for use with the sample holders in the optical setup.

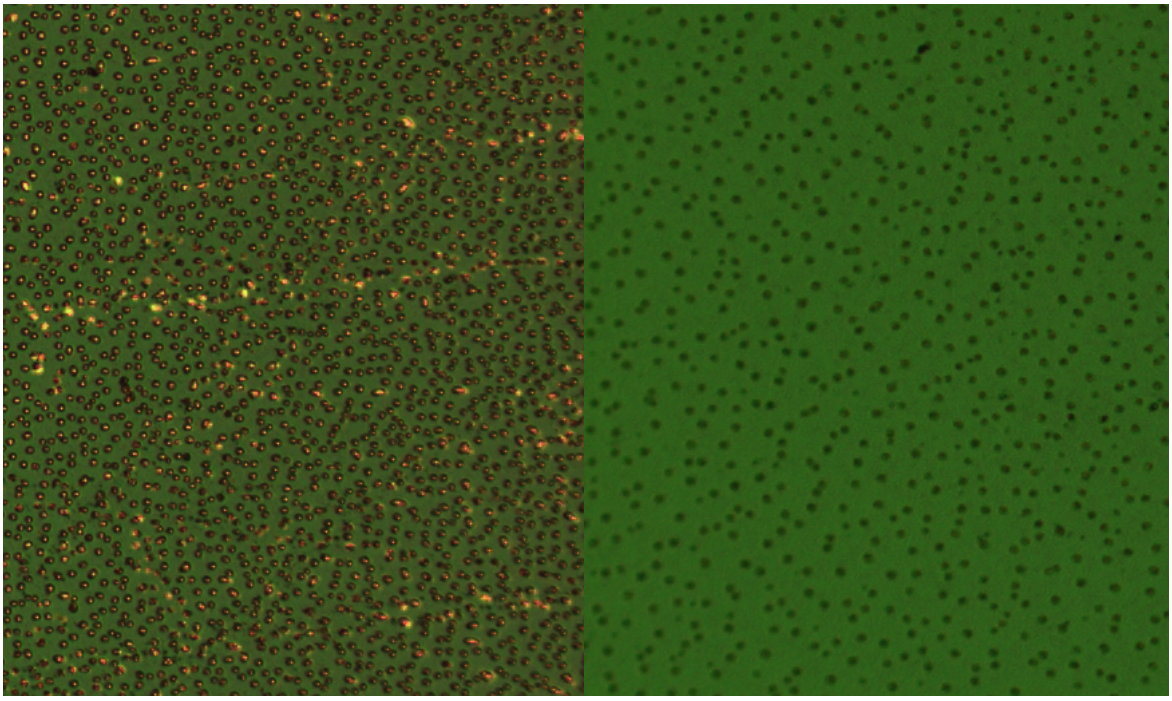

Figure 3.1: Optical microscope image of the surface of an AlGaN sample before (left) and after (right) acid treatment. The yellow dots seen to disappear are the gallium droplets.

3.2.1 Wafer Scribing

The structures used in this work were grown on commercial 3" GaAs substrates and so samples must be reduced to a more convenient size. A diamond-tip scribing tool is used to scribe and cleave the wafer perpendicular to the crystallographic planes into pieces approximately $5x5mm^2$. A fitted respiratory mask is worn during this stage to prevent inhalation of toxic GaAs dust and waste material is disposed of in accordance with environmental regulatory procedure.

3.2.2 Surface Cleaning

A consequence of maintaining an excess of gallium during MBE growth is that it is present on the surface after growth and gallium-rich droplets are formed on the surface of the wafer after post-growth cooling, these must be removed before characterisation to prevent interference with optical absorption and surface mechanics of the sample. This was accomplished by submersing all samples in 1:1 $H_2O : HCl$ for several hours before processing begins. Where appropriate between fabrication stages the sample surface was subjected to a four solvent clean to remove unwanted organic compounds, these were, in order: ethyl lactate, acetone, methanol, and isopropyl alcohol (IPA). More robust samples were immersed in an ultrasonic bath while the more delicate samples were subject to gentle mechanical agitation. Afterwards samples were removed from the solvent and flushed with IPA to remove immersion residue. The samples were dried off in an inert gas environment provided by a pressurised nitrogen gun.

3.2.3 Photolithography

Optical photolithography is the process by which a desired pattern may be transferred to the sample surface preceding a subsequent fabrication stage such as chemical etching or metallisation by thermal evaporation. It is realised by applying photoresist in an even layer to the sample surface, solidifying it by baking, and then selectively exposing areas of the surface to ultra-violet light. Depending on whether the photoresist is "positive" or "negative", exposure to UV radiation will cause the organic material to degrade and destabilise or polymerise/cross-link and become more resistant to exposure to developing agents. The less chemically stable regions are therefore preferentially etched on immersion in a developing solution and removed to leave the desired pattern. BPRS 150 positive photoresist supplied by Olin Hunt Speciality Products, Inc. USA, and AZ 400 K Developer from AZ Electronic Materials GmbH, Germany were used for photolithography in all cases.

3.2.4 Membrane Fabrication

In this work the characterisation of free-standing thin semiconductor films is undertaken. The fabrication process for the membranes is as follows: First, the sample is adhered substrate side up to a small piece of alumina by manually applying BPRS 150 photoresist with a micro pipette syringe and baking for 30 minutes at 110 °C.

Next the sample is vacuum mounted to a Solitec Spin Coater and another layer of the same is spin coated to a thickness of roughly 1 µm on the top surface by revolving at 4000 RPM for 30 s and baked again. A patterned array of circles with radius ∼ 0.5 mm are transferred to the substrate by standard UV photolithography techniques detailed above with the aid of a shadow mask. The sample is then immersed in a citric acid/hydrogen peroxide solution 2 $C_6H_8O_7$ (50% by weight)/1 H_2O_2 (30%) for ∼24 hours or until the entirety of the substrate has been etched away. The III-Nitride compounds are strongly resistant to most forms of wet chemical etching and so serve as a natural stop point. There is a clear visual distinction between the substrate and transparent thin film that shows the etch is complete shown in Fig. 3.2. The photoresist is then removed by soaking in warm acetone and the free-standing membranes are ready for mounting. An illustrated sequence of the processes can be seen in Fig. 3.3.

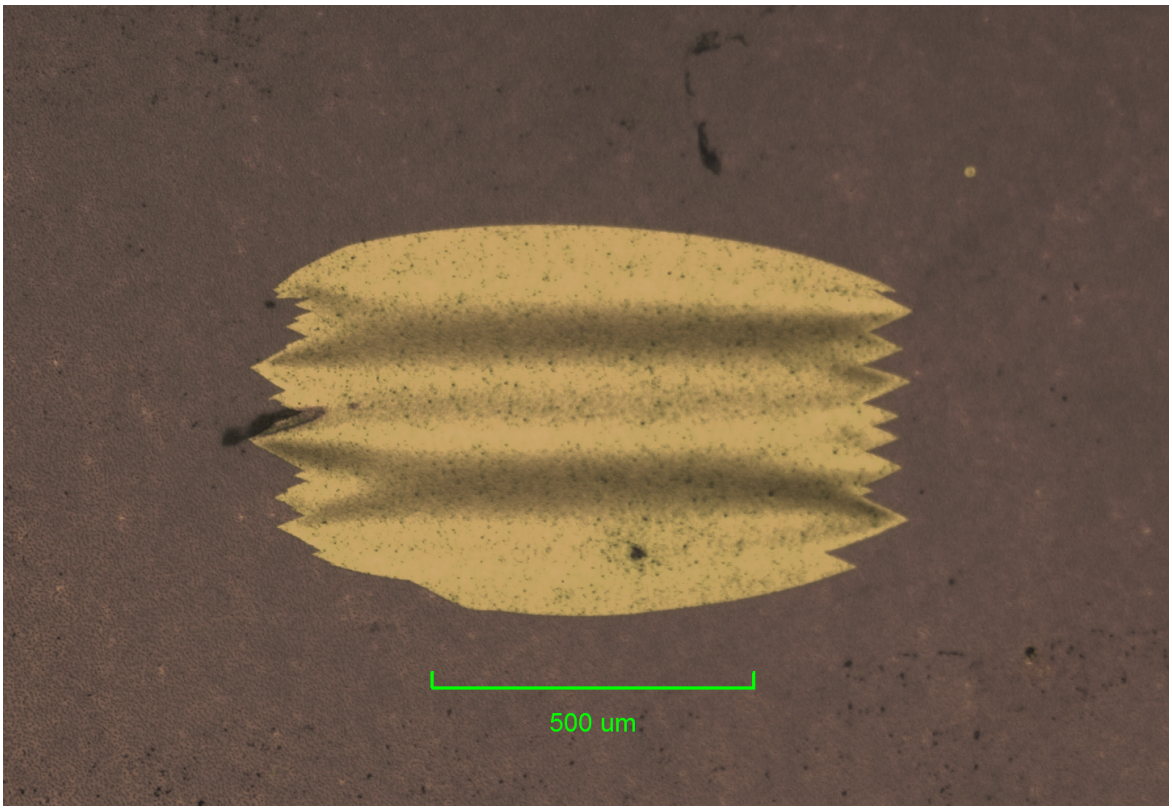

Figure 3.2: Optical microscope image of free-standing cubic AlGaN membrane.

Due to the substantial lattice mismatch between our pa-MBE grown epilayers and the substrate there is considerable strain in the sample. Previous work on the production of a free-standing cubic GaN substrate for growth applications at the University

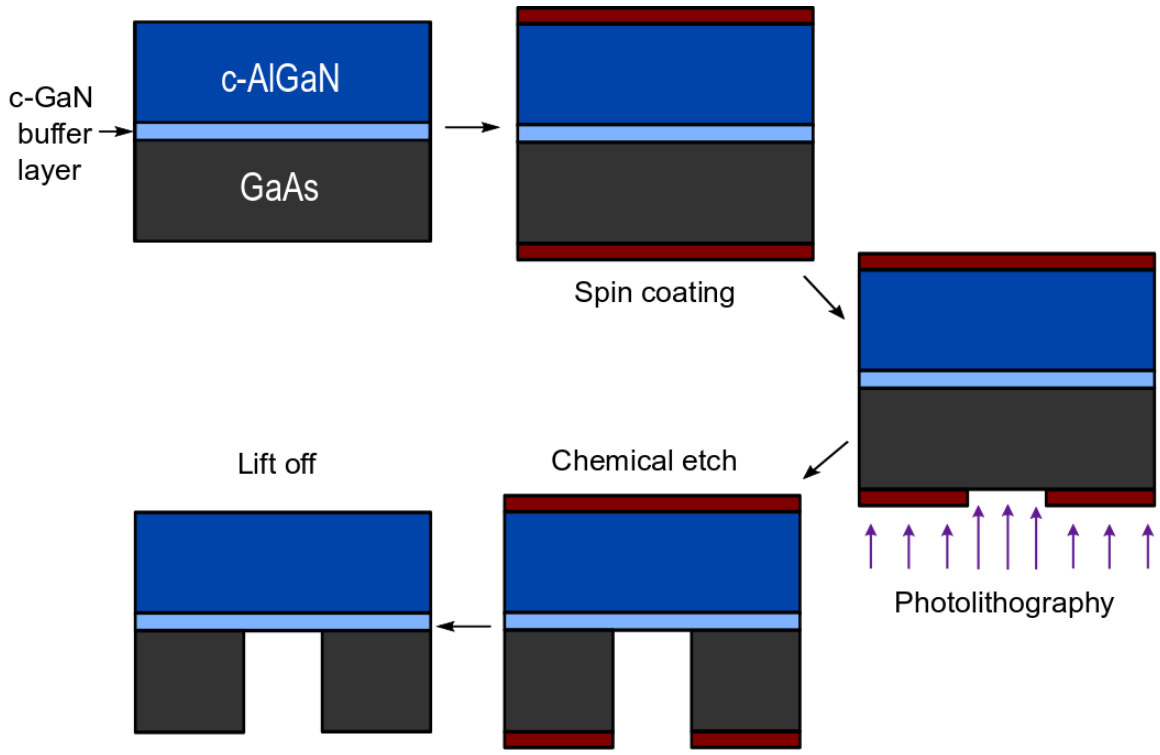

Figure 3.3: Fabrication process of the free-standing cubic AlGaN membranes

of Nottingham showed that for films of thickness <1 µm release from the interfacial strain caused the layers to crack and bend into rolls [38]. The resulting non-uniform topography of the membrane can be observed in Fig. 3.2. There are not any anticipated negative effects as a result of this due to the much larger length scale of the apparent variations in the film compared to the size of the optical spots in the pump probe experiments.

3.3 Experimental Methodology

In this section the main experimental techniques applied in the course of this work are detailed. The first section consists of a comprehensive description of the generic optical bench setup and the commonalities between all the pump-probe experiments conducted. Further sections outline specific characterisation techniques used to extract physical parameters from samples to aid in analysing the pump-probe data.

3.3.1 Reflection Pump Probe Technique

All the key experiments detailed in this work are based on the ultrafast optical pump-probe technique, the principles of which were explained in the previous chapter (Section 2.1). There are slight variations in the experimental setups used in the course of this work; a discussion of that which remains constant and a typical optical bench configuration will be presented here with any differences addressed in their respective sections further on. In each experiment the samples are optically excited to generate acoustic waves with a femtosecond optical pulse. The time evolution of the sample transient reflectivity response is then monitored with a second weaker probe pulse. The advantages of the pump probe technique are that it can be used to measure the sample response to strain effects with femtosecond resolution without the need for ultrafast electronics, using only comparatively slow photo-detectors and signal acquisition equipment. The upper boundary on temporal resolution is consequently limited by the temporal width of the probe pulse, which is dependent on the bandwidth of the laser gain medium and the number of phase locked modes in the optical cavity. The standing wave modes in the cavity are set with fixed phase differences such that they periodically constructively interfere creating an intense pulse of light. The phase difference is set with an active mode locker that modulates the light in the cavity with an acousto-optic modulator (AOM), if the modulation rate is synchronised to the cavity round-trip time then a single pulse of light will rebound back and forth in the cavity.

A diagram of the typical experimental arrangement can be seen in Fig. 3.4. The excitation source is a Spectra-Physics Tsunami Ti:Sapphire oscillator pumped by a Spectra-Physics Millenia Xs Nd:YVO_4 continuous wave diode laser. The wavelength is calibrated by the use of a prism sequence and slit arrangement. The prisms diffract the beam spatially separating the constituent wavelengths and enabling the position of the slit to select the desired energy. The pulse width is tuned using prism pairs which introduce a net negative group velocity dispersion of the beam to offset the positive dispersion from other optics in the cavity. The oscillator operates at 82 MHz with pulse durations of ∼130 fs. The fundamental output of the excitation beam may be tuned within the range 700-1080 nm with an output power of ∼1W at 750 nm which was standard for our experiments. The beam is then directed into a Harmonixx FHG frequency multiplier and converted to second and third harmonic using non-linear crystals. The generated second and third harmonics are used interchangeably as the pump and probe sources depending on the chosen fundamental frequency and the sample structure under study. In this thesis two optical configurations are employed, both of

them in the reflection geometry. The first is UV/blue as illustrated in Fig. 3.4. The second is a single colour pump-probe setup, in which case either the second or third harmonic is divided with a beam splitter immediately after output from the harmonic generator.

The pump beam was passed through two variable apertures which are used to align the path parallel with the motion of the retroreflector. Any misalignment will cause the beam to wander as the stepper motor moves the stage back and forth. The variable delay is placed in the pump path as any unintentional movement will only affect the intensity of the strain seen by the probe and not reflect any inhomogeneities in the sample itself. The position of the retroreflector can then be manipulated to adjust the total path length of the pump beam and therefore the time of arrival at the sample of the pump and probe pulses. The pump and probe pulses are then focused to the same point on the sample surface with the aid of a digital microscope camera system. The pump beam falls on the sample normal to the surface while the probe pulse reflects with an incident angle of approximately 30°. The reflected probe light is collimated and passed through a polariser to eliminate the effect of scattered pump light from the measurement. The second and third harmonics are naturally polarised perpendicular to one another as a consequence of the harmonic generation process so the elimination of interference from scattered light is trivial. Depending on the wavelengths a band pass filter was employed instead of the polariser where appropriate.

The strain dependent variation in reflectivity is extracted from the equilibrium and strained reflectances with a phase-sensitive detector (lock-in amplifier) as a function of stepper position. By incrementally translating the retroreflector stage, a series of snapshots depicts the time evolution of the strain induced reflectivity changes in the sample. An AOM is used to modulate the pump beam by periodically generating an acoustic field in the crystal in the device. This acoustic field controls the intensity of light emitted at the Bragg diffraction angle, which serves as the pump. The AOM is driven by a pulse generator which also serves as a reference signal for the lock-in amplifier. The pump beam was modulated at 200kHz in all experiments described in this work. As the signal amplitude was highly sensitive to the calibration of the system a graded attenuator was used to moderate the beam power incident on the samples.

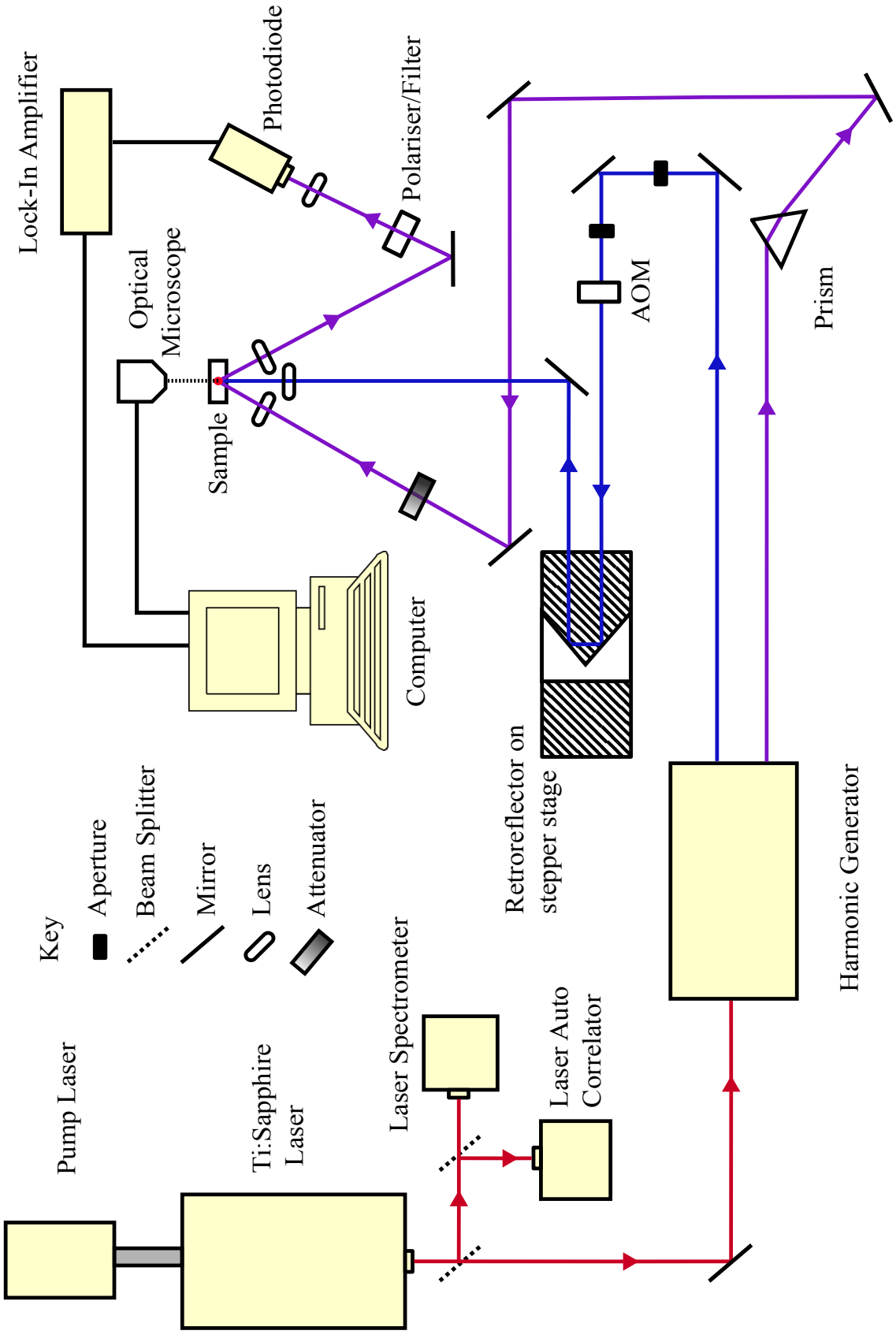

Figure 3.4: Optical bench setup for pump-probe experiments in reflection geometry. The blue and purple lines depict the paths of the pump and probe beams respectively.

3.3.2 Atomic Force Microscopy

The surface morphology of cubic (AlGa)N samples were investigated in the course of this work by atomic force microscopy (AFM) on an Asylum Research MFP-3D system. The advantages of AFM over other imaging techniques for surface reconstruction such as scanning electron microscopy (SEM) are the enhanced resolution and the ease of use; SEM requires the sample to be sputtered with a conductive coating of metal or carbon and necessitates operating under vacuum.

The operating principle behind AFM is described as follows: First the sample is placed on the scanner stage, the position of which can be manipulated on the order of nanometers by applying a voltage to the piezoelectric actuators controlling the position of the stage. Next, the atomically sharp tip on the end of a cantilever is brought into proximity with the surface of the sample via a feedback loop between actuator and position sensor. If the tip crashes into the surface it may damage the sample and become blunt; the sharpness of the tip is crucial to the quality of the resulting image.

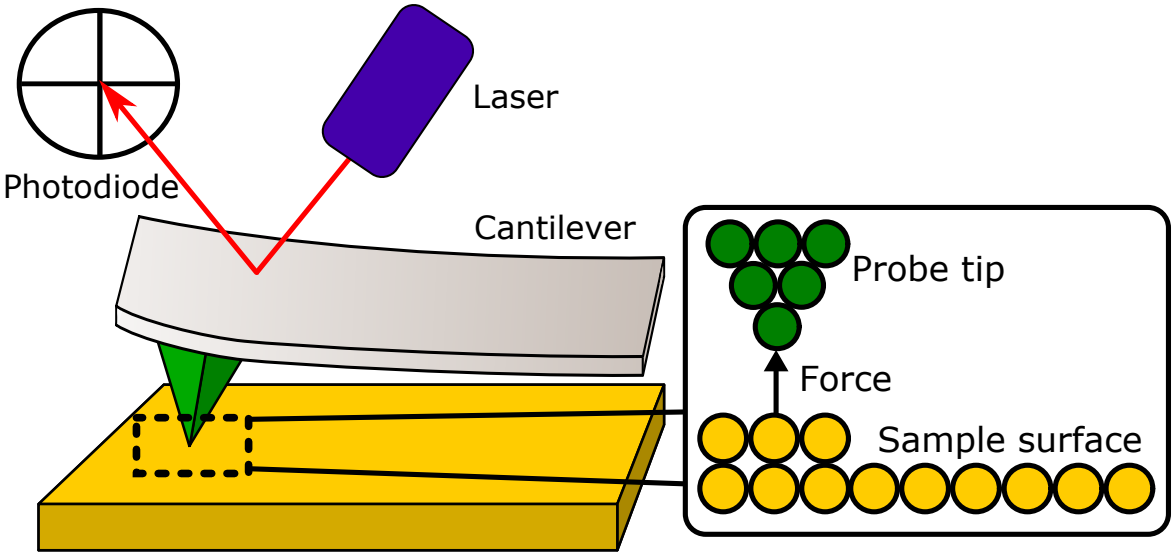

Figure 3.5: Simplified schematic diagram of AFM measurement system.

The software which controls the stage movement and analyses the tip response is provided by the manufacturers of the AFM system and written in the Igor Pro environment. Fig. 3.5 shows the standard operating principle for AFM measurements. In scans performed in this work the AFM is operating under tapping mode which measures a the variation in the resonant frequency of the cantilever as a function of

tip position due to surface forces on the end of the tip. In the constant amplitude regime the tip is rastered across the sample surface and changes in the vertical (z-axis) position of the tip equate to a change in the topography of the sample surface. The deflection of the cantilever is monitored by a laser reflecting off the end of the tip into a split photodiode. Scans were performed in a 5x5 µm area with sub-nanometer resolution. The probes employed were Multi75Al-G cantilevers with a nominal spring constant of $\sim 2.8\,\mathrm{N\,m^{-1}}$. The AFM results were evaluated with the aid of open source software Gwyddion for data visualisation and analysis.

3.3.3 Variable Angle Spectroscopic Ellipsometry

Variable angle spectroscopic ellipsometry (SE) was used in the course of Chapter 4 as a tool for comparative analysis with the results from picosecond acoustics experiments. Acquisition of SE data was performed under the supervision of Dr. Chris Mellor who also fit the data to a theoretical model of the sample to extract the optical parameters.

An ellipsometer can be used to determine physical and optical constants of thin films and bulk samples by monitoring the change in polarisation undergone by two linearly polarised beams of light as they reflect from the sample structure. The surface differentiates between the p- and s-plane light resulting in a shift in phase separation (Δ) and relative amplitude ratio (Ψ) which is measured as a function of incident photon energy. The ellipsometric parameters Δ and Ψ are defined by

$$\frac{r_p}{r_s} = \tan\Psi \exp\left(i\Delta\right), \tag{3.1}$$

where r_p and r_s are the complex Fresnel reflectance coefficients. Ellipsometric measurements are generally performed at high angles of incidence where the difference between r_p and r_s is greatest. An illustration of the measurement geometry can be seen in Fig. 3.6 where E represents the electric field vector, which is elliptically polarised after reflection from the sample. Ψ and Δ are dependent on and therefore contain information relating to key parameters such as refractive index, surface roughness, film thickness and extinction coefficient. A more thorough analysis of the theory and applications of ellipsometry may be found in Ref. [110].

The ellipsometry measurements were taken on a JA Woollam Inc. M2000-DI in-

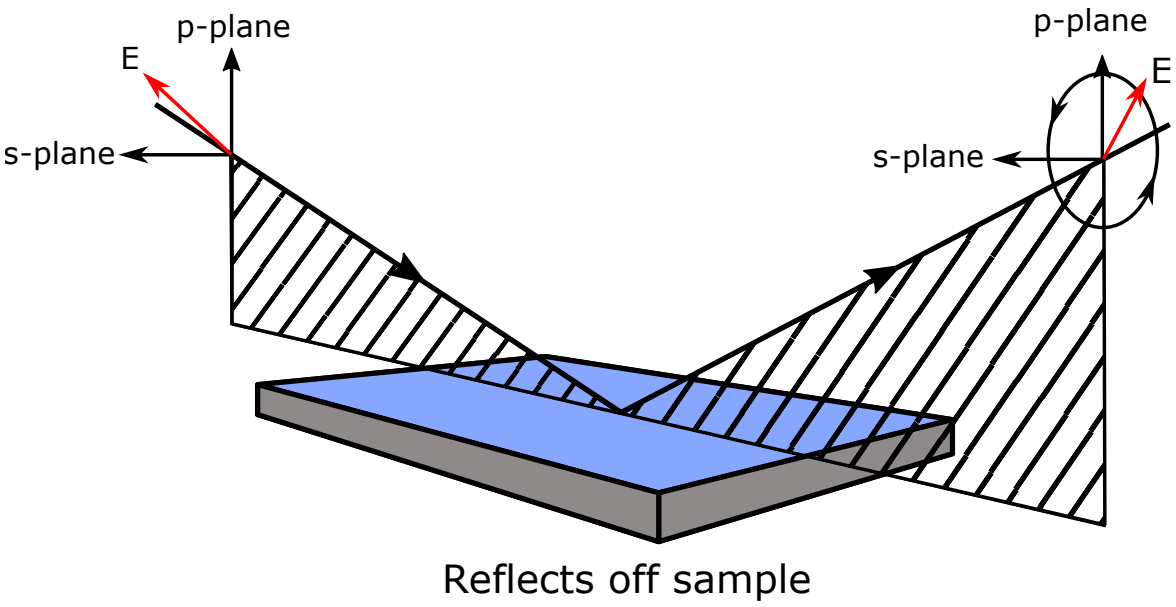

Figure 3.6: Operating principle of spectroscopic ellipsometry.

strument (193-1690nm) and the data was analyzed using the manufacturer's software CompleteEase v5.19. The measurements were made using focusing probes at incident angles of 55°, 60° and 65° over a photon energy range from 0.7 to 6.5 eV. The probes reduce the possibility that reflections from the rear surface of the substrate, at photon energies less than 1.3 eV, interfere with the interpretation of the data. The samples measured were gallium arsenide wafers on which a GaN buffer and $Al_xGa_{1-x}N$ layer had been grown sequentially. To obtain the optimal fit the optical response of both the GaN layer and the AlGaN layer were modelled using Kramers-Kronig consistent functions; the optical response of the gallium arsenide was taken from the JA Woollam materials library.

For modelling the unknown complex optical functions of the layers a dispersion relationship is applied to fit the optical constants dependence on wavelength. For the GaN buffer layer the JA Woollam 'Psemi-tri' parametric model was used, which is designed to model the asymmetric optical response close to a semiconductor band edge in conjunction with a Gaussian oscillator which accounts for the absorption in the non-transparent regime. The $Al_xGa_{1-x}N$ layer was simulated with two Gaussian oscillators and a UV pole function that captures the effects of the dielectric function at energies above our measurement range.

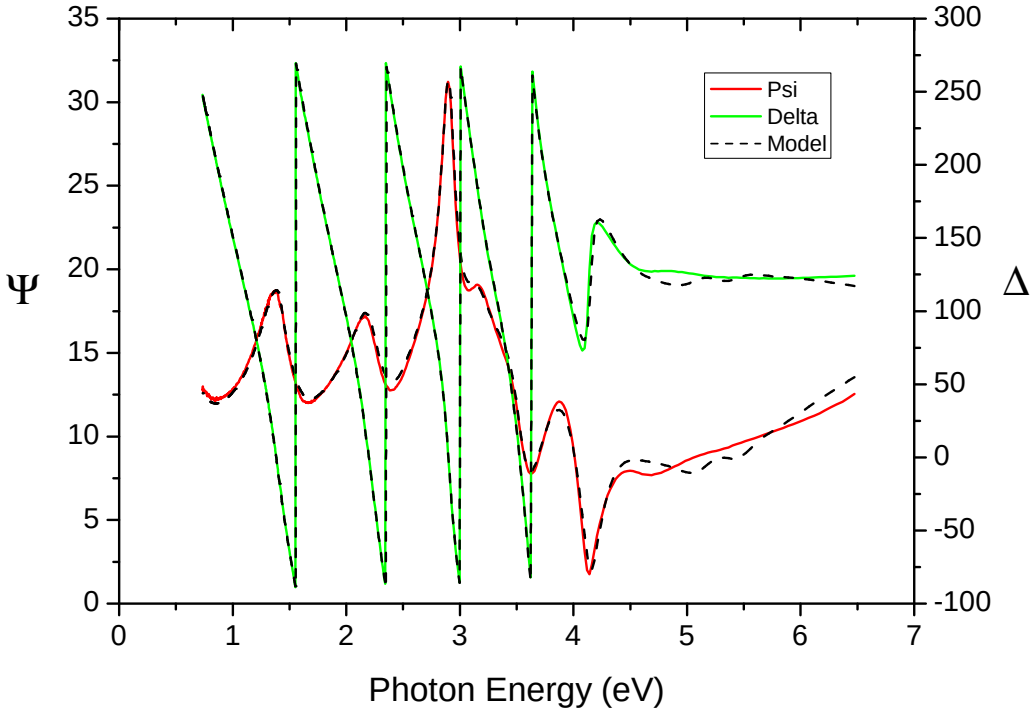

Figure 3.7: Spectroscopic ellipsometry parameters of Ψ and Δ measured at 65° incidence and fit with the model described in the text for the sample with $x = 0.49$.

To illustrate the approach to modelling the SE response the measured data along with the fitted curve for the sample with $x = 0.49$ taken at 65° is shown in Fig. 3.7. An additional complication is the fact that the mean square error (MSE) is significantly reduced by introducing a gradient in the optical density of -9.5% (i.e. the optical density decreases as the free surface is approached) and a surface roughness parameter of several nm. The MSE of this model is 7.9.

Chapter 4

Characterisation of Cubic (AlGa)N Bulk Layers

This chapter will present the results of characterisation studies by picosecond acoustic spectroscopy of cubic c-$Al_xGa_{1-x}N$ epilayers both adhered to and separated from the epitaxial substrate. In this work the basic elastic and optical constants for a series of c-$Al_xGa_{1-x}N$ films were investigated. The studied layers and their associated growth and physical parameters can be seen in Table 4.1. These wafers were all grown by molecular beam epitaxy on GaAs (100) substrates and the film thicknesses were measured post-growth by ellipsometry. The aluminium incorporation was controlled by varying only the temperature of the aluminium effusion cell during growth. The aluminium fraction was determined by electron probe microanalysis (EPMA) using a Cameca SX100 system [111]. It was found that the inclusion rate of aluminium did not vary significantly with depth, and the fractional error for x did not exceed 2%. The films are unintentionally doped with an n-type conductivity, most likely due to incorporation of oxygen impurities during the growth process. The viable aluminium fractions for study were limited by the potential pump and probe excitation energies available from our laser system and the sensitivity of the detection scheme to these frequencies.

A detailed knowledge of the optical and acoustic properties of zinc-blende c-$Al_xGa_{1-x}N$ is of fundamental interest for the engineering of finely tuned optoelectronic and nanomechanical devices. A comparative wealth of information is available on the binary nitrides and their behaviour is well understood but there remain large gaps in the data for the physical properties of the alloys. Optical studies of c-AlGaN have been previously conducted by photoluminescence (PL), cathodoluminescence, reflectance spectroscopy and ellipsometry [49, 111–114]. These studies are mostly concerned how-

ever, with discerning the fundamental band gap of the alloy and to date there has not been a picosecond acoustic study of the elastic constants.

Measurements of the dynamical interference of the strain pulse with the probe beam (so-called Brillouin oscillations) allow for the derivation of the complex refractive index and an estimate of the photoelastic constants with respect to their dependences on optical wavelength. Experiments conducted on free standing membranes provide the relation of the longitudinal sound velocity to aluminium content for a series of samples with x ranging from 0.08 to 0.66.

Wafer No.	$\boldsymbol{x}$	**Al Effusion Cell Temperature (°C)**	**c-GaN Buffer Thickness (nm)**	**c-$\mathbf{Al_xGa_{1-x}N}$ Thickness**
SN437	0.08	945	52	229
SN434	0.16	975	89	359
SN442	0.23	996	44	300
SN438	0.42	1020	59	300
SN444	0.49	1028	52	292
SN439	0.66	1043	53	294

Table 4.1: Sample specifications for all studied $c - Al_xGa_{1-x}N$ epilayers.

4.1 Characterisation of Bulk AlGaN on GaAs Substrates

For the characterisation of epitaxial thin layers *in situ* on the growth substrate the picosecond strain pulse is excited by pumping the samples with a femtosecond laser pulse of wavelength $\lambda_{pu} = \lambda_0/2 = 380\text{-}450\,\text{nm}$. For this range of frequencies the epitaxial c-(AlGa)N layer is transparent to the pump pulse, it being below the band edge, and the pump is absorbed within a short distance ($\sim$15 nm) at the interface between the GaN buffer layer and the GaAs substrate, as seen in Fig. 2.1. The energy absorbed in the c-GaN buffer layer, which has a band gap of 3.2 eV (corresponding to 388 nm), may be neglected due to the small thickness and comparatively weak absorption at these energies. The result of this excitation is the propagation of two strain pulses in opposite z directions, into the GaAs substrate (positive) and towards the free surface (negative) through the alloy layer [62]. The negative part of the compressive strain pulse $\eta_{zz}(z,t)$

is partially reflected at the interface and partially injected into the c-(AlGa)N layer where it propagates there with velocity s_a. The acoustic reflection coefficient at the interface moving from the substrate into the film is $R = 0.76 \pm 0.01$ following acoustic mismatch theory [75]. The pulse has a temporal width of several picoseconds and an approximately Gaussian spatial profile. The detection of this strain pulse is realized by using a probe femtosecond laser pulse of wavelength $\lambda_{pr} = \lambda_0/3 = 250\text{-}300\,\text{nm}$ and measuring the change in reflectivity $\Delta R(t)$ incident on a UV enhanced silicon photodiode. The average power of the pump and probe beams throughout were 10 mW and 1 mW respectively.

Three layers, of varying aluminium fraction, have been studied by observation of the Brillouin oscillations as the strain pulse travels from the substrate towards the surface of the grown layer. The frequency of the Brillouin oscillations are dependent on the incident probe photon energy and the refractive index of the material, we thereby obtain the data for the refractive index as a function of wavelength. The raw reflectivity measurements for layers of $x = 42\%$, 49% and 66% can be seen in Figs. 4.1a–4.1c. Vertical dashed-dotted lines at $t = 0$ denote the time at which the pump pulse excites the GaAs substrate. The vertical dashed lines correspond to the times at which the strain pulse enters the alloy layer and encounters the free surface of the sample respectively. Measurements were taken at a variety of probe wavelengths within the transparency window for samples and below the limit at which significant absorption in the AlGaN layer begins.

The signal $\Delta R(t)$ is dependent upon two discrete mechanisms: the displacement of the interfaces and free surfaces in the sample and the photoelastic effect. Both mechanisms are defined by their modulation of the interference terms for the probe beams reflected at the interfaces and perturbations of the complex refractive index $\tilde{n}$. This leads to a harmonic modulation of the reflectivity, the period of which is directly related to the photoelastic properties of the sample [99]. There are no rapid reflectivity jumps associated with a change in the film thickness as the strain pulse crosses the interfaces at times t_1 and t_2. This suggests that the detection scheme is simply not sensitive to the displacement effect and so the focus of this chapter will remain on the photo-elastic contribution. The oscillation frequency, f_B, derived from performing the fast fourier transform (FFT) after subtracting the slow varying electronic background signal from $\Delta R(t)$ allows for the calculation of the room temperature refractive index for the cubic AlGaN samples at the probe wavelengths. For $\kappa \ll n$:

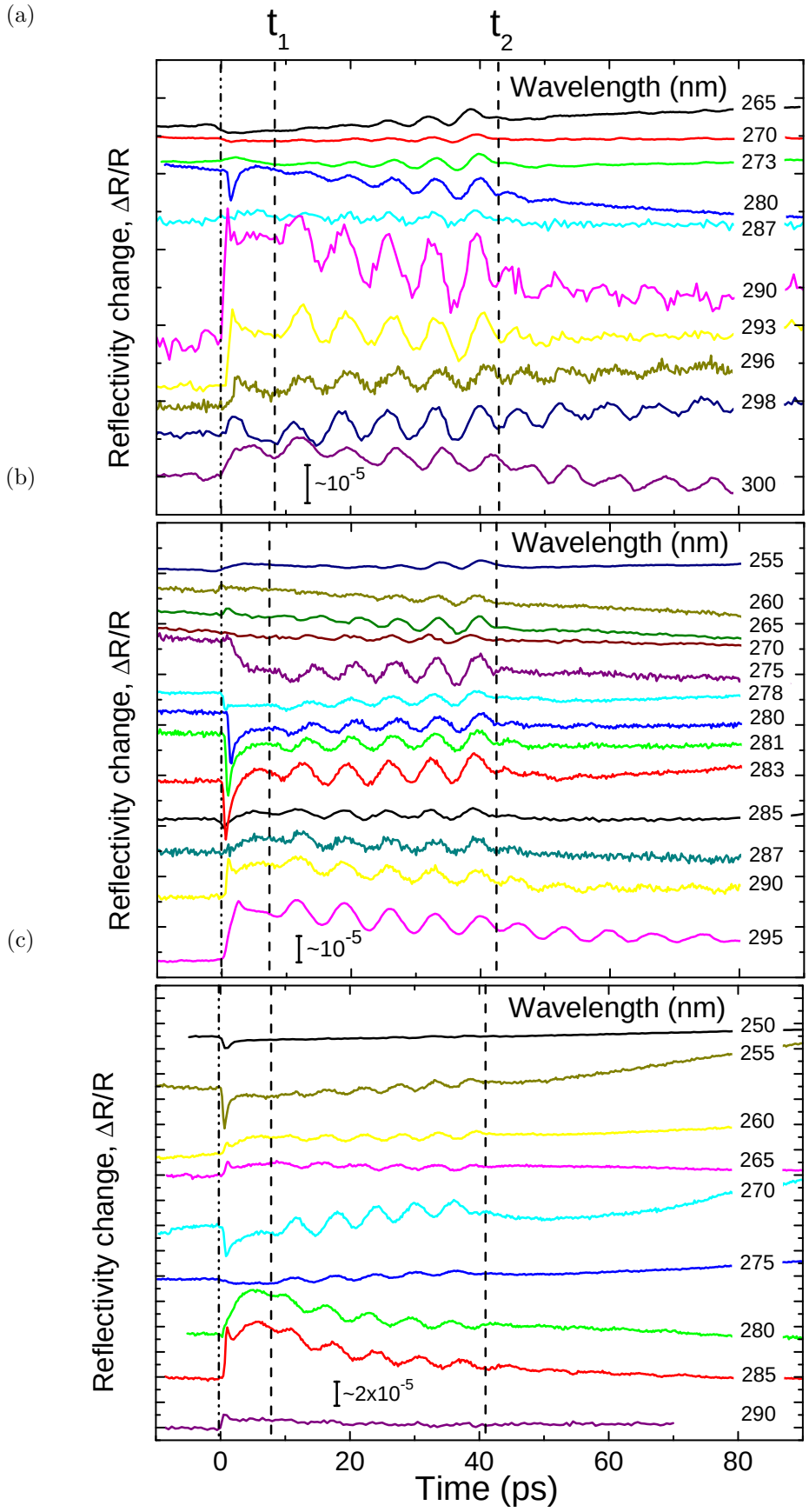

Figure 4.1: Pump-probe response for $c - Al_xGa_{1-x}N$ films with x = (a) 0.42, (b) 0.49 & (c) 0.66 at different probe wavelengths. The dashed lines show the beginning and end of strain pulse propagation in the AlGaN epilayer. Time = 0 has been set to the moment of coincidence between pump and probe pulses.

$$f_B = \frac{2s_a}{\lambda_{pr}}\sqrt{n^2 - \sin^2\theta}, \tag{4.1}$$

where $\theta = 30°$ is the angle of incidence of the probe beam on the sample in the experimental conditions described in this work. The speed of longitudinal sound in the c-AlGaN compounds s_a is derived from a simple interpolation between the speed of sound measured in c-GaN [75,76] and the theoretical speed of sound in c-AlN based on elastic constants obtained from density-functional-theory calculations [115]. It can be seen from Eq. (4.1) that the strain pulse acts as a partially reflecting mirror within the sample moving towards the free surface and that maximum interference occurs when Bragg's condition is met.

The high amplitude transient reflectivity response in the first few picoseconds after the pump is absorbed can be attributed to the electronic background from the large concentration of non-equilibrium carriers which reduces to zero as the carriers migrate to the band edge and recombine in addition to the more slowly decaying thermoelastic contribution which relaxes proportionally to the thermal conductivity. The acoustic contribution in the form of Brillouin oscillations can be seen between times $t_1 \approx 10\,\text{ps}$ where the strain pulse enters the alloy layer and $t_2 \approx 40\,\text{ps}$ at which time the strain pulse hits the semiconductor-air interface and is under certain conditions observed after the reflection. Discussion of the scattering of the strain pulse at the free surface is covered in greater detail further in Section 4.1.3. Brillouin oscillations are not observed in the initial few picoseconds while the strain pulse traverses the GaN buffer layer as the probe beam is not sensitive to the photo-elastic changes due to the relatively weak absorption. This section consists of a discussion of the measured complex refractive index by picosecond acoustic (PA) techniques and a comparison of the results with those obtained by spectroscopic ellipsometry (SE) here and elsewhere. The focus then moves to the photoelastic effect and its associated parameters, which define the amplitude and phase of the Brillouin oscillations. Finally the reflection of the strain pulse at the free surface is discussed.

4.1.1 Complex Refractive Index

The correlation between refractive index in a semiconductor and the energy of incident photons typically obeys an exponential relationship where the phase velocity of higher frequency waves are more greatly reduced by the dispersion in the material

at wavelengths greater than the fundamental absorption edge. Additional features in the dispersion of the refractive index appear at energies corresponding to inter- and intra-band transitions. The complex refractive index is the sum of the real and imaginary components, the index of refraction n and extinction coefficient k. All e-m waves travelling in any medium will be attenuated as an exponential function of path length, the degree of attenuation is wavelength dependent and in semiconductors increases rapidly at the band-gap energy. The two components are Kramers-Kronig consistent and may be written together as

$$\tilde{n} = n + i\kappa. \tag{4.2}$$

As the energy of the incident light approaches the band edge of the semiconductor in question there is a local maxima in the wavlength dependence of the refractive index at photon energy E_0 as is typical in III- V semiconductors [114]. The position of this local maxima closely follows the position of the band edge as shown in Figs. 4.2a–4.2c. The width of the maximum in the studied alloys is around 20 nm (∼300 meV) which is typical for the cubic nitrides [26, 112]. Likewise the extinction coefficient shows an increase with decreasing wavelength which is standard semiconductor response in the vicinity of the direct band gap energy. The tertiary alloys commonly display broader features in the optical and electronic parameters than the binary alloys due to random spatial fluctuations in the atomic composition which maximise when the group-III atoms are roughly at parity with each other [111]. These compositional variations translate to local variations in the electronic band structure broadening the absorption edge as the minimum energy for valence-conduction band transition is non-uniform in the material. The peak position in the wavelength dependence of n is tightly correlated with the onset of the first optically induced electron-hole transitions across the band gap energy i.e. $E_0 \approx E_g$. This is a reliable approximation, as has been demonstrated in previous studies of c-GaN [116], c-AlN [27] and c-AlGaN [114] alloys by ellipsometry. The values obtained for E_g in this way are presented in Table 4.2.

Because zinc-blende GaN is a direct ($\Gamma_c \rightarrow \Gamma_v$) band gap semiconductor and zinc-blende AlN possesses an indirect ($\Gamma_c \rightarrow X_v$) fundamental energy gap, there is clearly a composition-dependent transition at which point the behaviour shifts from direct to indirect. The precise position of this behavioural transition is still somewhat controversial although it has been theoretically predicted to occur at around $x = 0.7$, close to the value of the highest Al content sample studied here. In any case, there is no

experimental evidence in this work to suggest that this boundary has been crossed. This does not preclude the existence of an indirect band gap at around 5 eV, however a definite conclusion would require rigorous studies beyond the scope of this work which concerns itself only with the elastic constants.

The values for the extinction coefficient for c-$Al_xGa_{1-x}N$ around the band edge have been calculated by finding the absorption depth from the attenuation of the amplitude of the observed Brillouin oscillations in Figs. 4.1a–4.1c. This is under the assumption that the amplitude of the Brillouin oscillations are linearly proportional to the incident probe light flux. The absorption length was determined by fitting an exponentially decaying harmonic oscillation with arbitrary phase constant to the picosecond acoustic data after subtracting the electronic background. Table 4.2 also displays the values of n, κ and hence E_g measured by ellipsometry in this work. The ellipsometry data for the three samples are presented in Fig. 4.3. Comparing the values obtained from picosecond ultrasonic and ellipsometry measurements [cf. values in Table 4.2] one observes that both techniques display the peak in the wavelength dependence for n. The values for n at the peak, and the position of the peak in terms of probe energy $E_0 = E_g$ are broadly similar to the results from picosecond ultrasonics and well within the estimated error. There is a far greater discrepancy in the values for the extinction coefficient κ: the values for κ measured by spectroscopic ellipsometry are in general significantly higher as compared to the picosecond ultrasonic experiments. The probable explanation for this is related to an attenuation of the strain pulse acting in opposition, with respect to sample depth, to the optical attenuation. The attenuation of phonons in the Brillouin frequency range by diffraction and scattering at defects and inhomogeneities as well as phonon-phonon interactions would cause the apparent amplitude of the Brillouin oscillations to decrease with time as the strain pulse moves towards the (AlGa)N surface. Although the distances travelled are relatively short for picosecond acoustic experiments, the high defect density in the material and room temperature experimental conditions nevertheless may cause significant attenuation in a short time frame. Neglecting these factors would lead to a consistent underestimate of the value of κ as is seen here and explains the discrepancy between the ellipsometry data.

Comparing the ellipsometry values obtained here with those reported earlier in other works [26, 112, 114]. There is a reasonable disagreement in the values returned for n and E_g in this work and the data measured in [26, 112], whereas the values reported

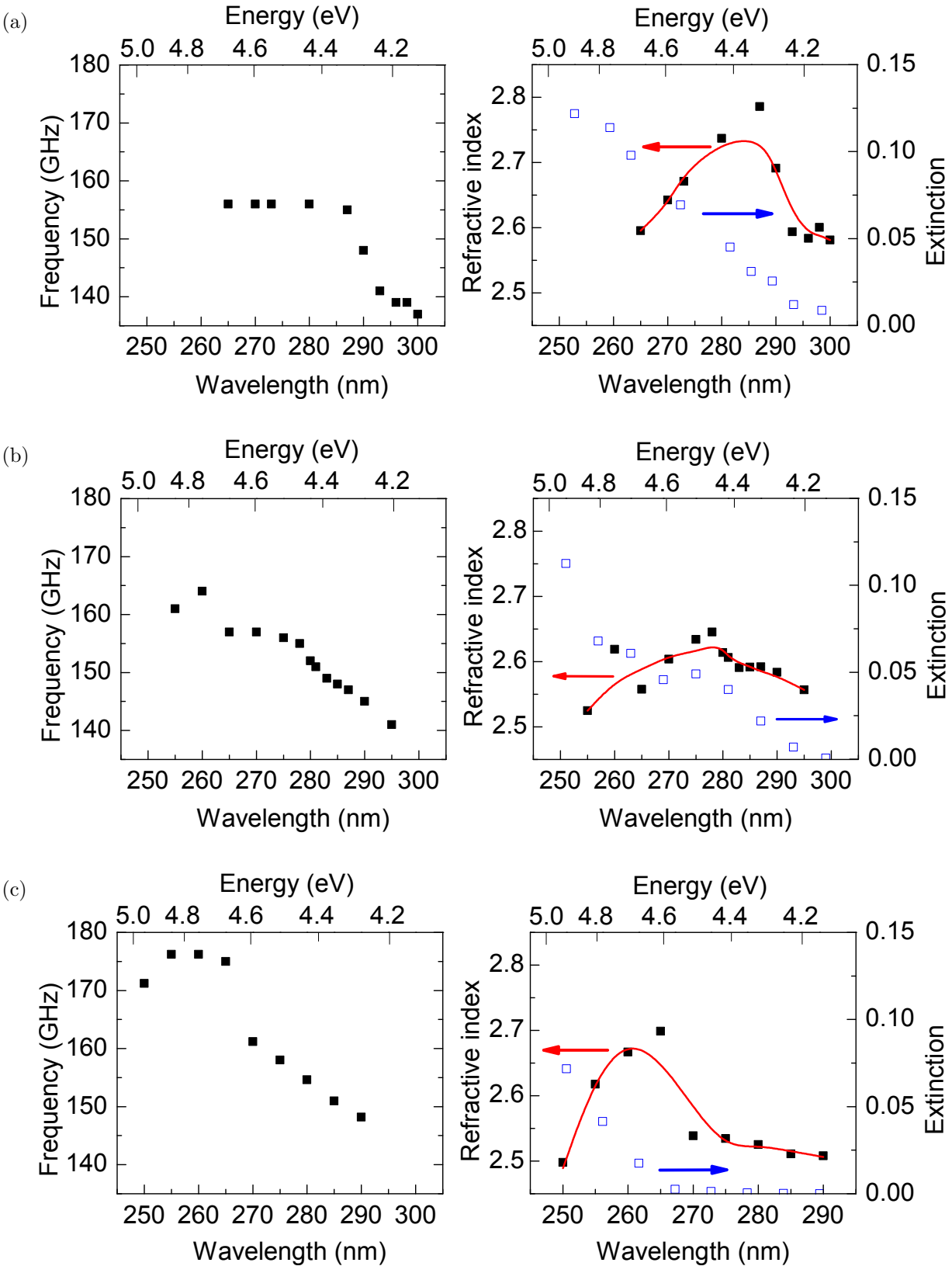

Figure 4.2: Dependence of refractive index, frequency of brillouin oscillations and extinction coefficient on wavelength for $c - Al_xGa_{1-x}N$ films with x = (a) 0.42, (b) 0.49 & (c) 0.66. In the right hand column the dependence of the real (closed squares) and the the imaginary (open squares) components of refractive index on probe wavelength are shown. The red line represents a smoothed fit of the data as a visual aid.

for κ are much more similar. The values of E_g measured in [114] are in far closer agreement and are notedly from a much more contemporary study. Moreover, there is an appreciable difference in the values reported for c-AlN in [26, 112] and those in more recent studies on c-AlN [27] and c-(AlGa)N [114]. The differences in the reported values in the literature could possibly be due to modern developments in growth technique, different epitaxial substrates and errors inherent in determining the aluminium content x. The effectiveness of the model used to analyse the SE data will also be important in manifesting any differences between the gathered results.

A more general point about the differences between SE and PA techniques is that the data analysis in SE experiments relies upon a smooth function to model the spectroscopic response, whereas the PA measurements record directly the response at a discrete set of photon energies. Another point is that the ellipsometric modelling software uses a parameter defining the surface roughness with a lateral length scale much shorter than the wavelength of the reflected light i.e. 100 nm. It is demonstrated in Section 4.1.3 that this is not a valid assumption for our samples, thus demonstrating the advantages of employing picosecond acoustic techniques in conjunction with ellipsometry.

4.1.2 Photoelastic Effect

This section will shift focus to an analysis of the photoelastic parameters which are responsible for the dominant contribution to the oscillations in the measured reflectivity $\Delta R(t)$. The Brillouin oscillations observed in the time period $t_1 < t < t_2$ when the strain pulse is propagating in the AlGaN layer, are due solely to the photoelastic effect which defines the phase and amplitude of the signal. When the photoelastic effect is the dominant mechanism the changes in reflectivity ΔR are a function of the changes in the complex refractive index, which is closely correlated to the value of the energy gap in the electronic band structure. For $\eta \ll 1$ we have [68]

$$\Delta\tilde{n} = \left(\frac{\partial n(E)}{\partial E} + i\frac{\partial \kappa(E)}{\partial E}\right)\frac{\partial E_g}{\partial \eta}\eta = p\eta, \tag{4.3}$$

where p is the photoelastic parameter. The efficiency of the photoelastic coupling is proportional to the deformation potential $\frac{\partial E_g}{\partial \eta} = \Xi_{DP}$, which has a value of $\sim$10 eV for direct band gap zinc-blende semiconductors [117], and the energy dispersions of n and κ. The effect is maximised around the band edge where the dispersions are at their

steepest. The sign of the photo-elastic parameter p and correspondingly the phase of the Brillouin oscillations are dependent on the value of the optical wavelength λ. The imaginary component $d\kappa/dE$ is always positive. For the spectral window studied here with a peak in the magnitude of n at $E = E_g$, dn/dE is alternatively positive at energies $E < E_g$ and negative where $E > E_g$.

It then follows that the phase of the light reflected from the strain pulse is dependent on the direction of the shift in local refractive index from the strain pulse and therefore on the gradient (derivative) of the relationship between refractive index and wavelength dn/dE. Whether a phase change occurs depends on the relative optical density of the reflecting medium to the transit medium. This phase change affects the interference at the point of detection, for example observe the clear phase transition in Fig. 4.1c between probe wavelengths of 265 and 270 nm which straddle the predicted band gap. This is the result of a sign change in the photo-elastic coefficients on either side of the peak value for n. This suggests the possibility of finding local maxima in the refractive index and thereby accurately identifying the position of the band gap E_g in transparent semiconductors by analysing the phase dynamics of spectroscopic Brillouin oscillation data, even in cases where the dependence of n on λ is not known.

The obtained values for the dependence of n and k on the probe wavelength are displayed in the right hand column of Figs. 4.2a–4.2c and derived from Eq. (4.1) where the speed of sound in the alloy is calculated from a linear interpolation. The real and imaginary components of $\Delta\tilde{n} = (\alpha + i\beta)\eta$ may be estimated from the gradient of the energy dispersions of the refractive index and extinction coefficient. The values for the dimensionless parameters α and β at optical wavelengths approaching the band gap are presented in Table 4.2. Clearly $\alpha = 0$ at $E = E_g$, where the dispersion is flat. The accuracy to which the photo-elastic constants may be stated in this case is limited by the value of the deformation potential which is not well defined for the cubic (AlGa)N alloys and still disputed. From [29] and the references contained within, an estimated uncertainty of $\sim$20% is taken based on the variance in reported values in prior studies. For this reason only the first significant figure for α and β is presented in Table 4.2. These values for the photoelastic constants are of comparable magnitude to other direct band gap semiconductors where the photon energy is in the vicinity of the band gap. For instance in GaAs ($E_g = 1.43$ eV) $\alpha = 2.8$ $\beta = 2.6$ for E =1.65 eV [85, 118]. The feature broadening in the alloys due to inhomogeneities discussed earlier most likely acts to reduce the maximum amplitude of the photoelastic effect. For direct

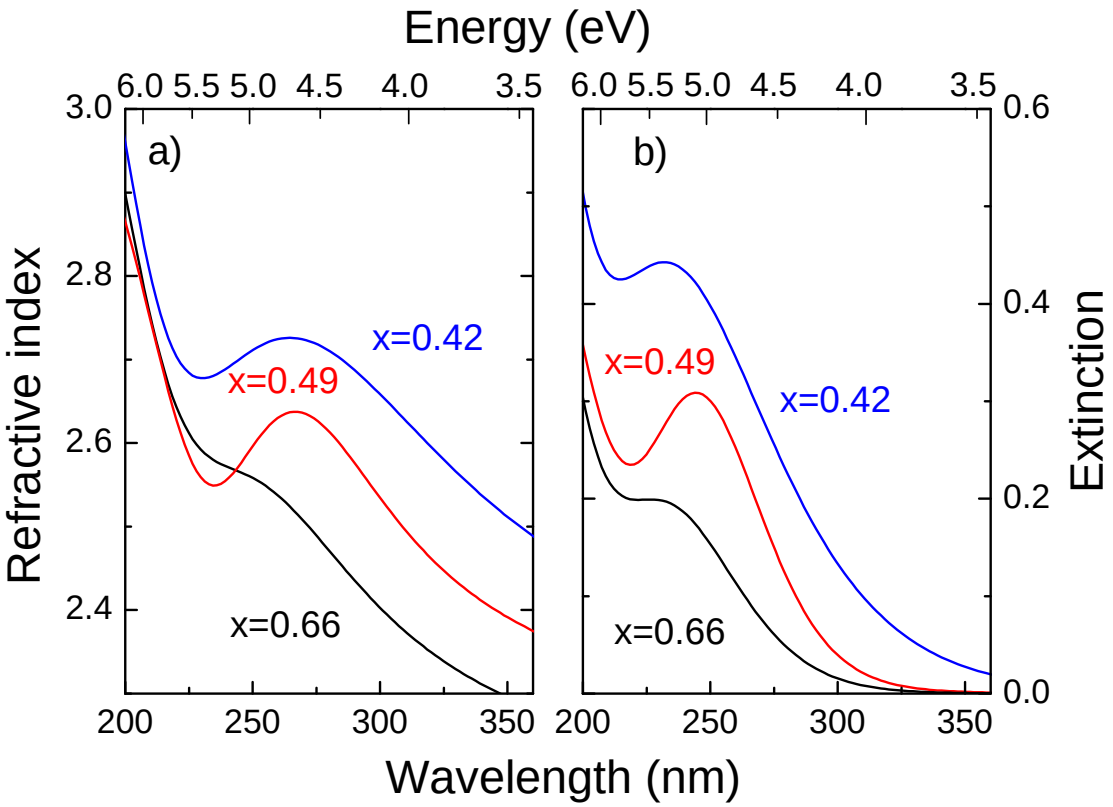

Figure 4.3: The dependences of refractive indices, n, and extinction coefficients, κ, on wavelength obtained from ellipsometry measurements for the samples with $x = 0.42$, 0.49 and 0.66.

band gap semiconductors with a sharp absorption edge the photoelastic parameters may be quite large when approaching $E = E_g$ from the low energy side. As a comparison, applying a similar analysis to the dielectric function dispersion data for c-GaN reported in [116] yields values of $\alpha \approx 10$ and $\beta \approx 20$.

A quantitative calculation of the relative reflectivity changes $\Delta R(t)/R_0$ (R_0 is the unperturbed reflectivity when $\eta = 0$), in response to strain induced fluctuations in optical constants may be performed via analytical [62, 82] or numerical [68] methods. The expected maximum amplitude of the Brillouin oscillations is calculated here using the estimated photoelastic parameters and following the derivation described in [62]. For short strain pulse and $\kappa \ll n$ one obtains the relation

$$\frac{\Delta R(t)}{R_0} \approx \frac{16\pi n p \eta \Delta z}{\lambda(n^2 - 1)} \tag{4.4}$$

where $z \sim$10 nm is the spatial width of the strain pulse. For $p \sim 10$ at the steep part of the dispersion and substituting in the experimental values for n and λ an estimate of $\Delta R(t)/R_0 \sim 10\eta$ is found. With the experimental result of $|\Delta R(t)|/R_0 \sim 10^{-4}$ this is equivalent to an average strain amplitude across the acoustic pulse of $\eta \sim 10^{-5}$. This value for strain amplitude is realistic for a pump excitation of 10 µJ cm^{-2} and consistent with other works generating strain in GaAs at similar pump fluences [119], despite a considerable loss at the GaAs/GaN interface due to reflection.

4.1.3 Surface Roughness

The fact that for most of the studied λ_{pr} the Brillouin oscillations are only observed in the time period $t_1 < t < t_2$ when the strain pulse is propagating in the AlGaN layer immediately after being generated in the GaAs substrate, indicates a large degree of conditional scattering at the free surface. There are only a few signals measured at longer wavelengths, i.e. $\lambda_{pr} \geq 290nm$, where the oscillations are detected after reflection at the free surface, obviously the scattering is proportional to the phonon frequency f_B. It was established in Section 2.3.1 that the reflectivity is only dependent upon one Fourier component or phonons with frequency corresponding to a wavenumber of $2k\cos\theta$, where θ is the angle between the probe wavevector and the normal to the surface. To understand why this is the case, consider radiation of wavevector k incident normally on a medium with refractive index n. For light scattered through 180° a momentum transfer of $2nk\hbar$ must take place. As long as $\kappa \ll n$ a phonon of momentum $p = 2nk\hbar$ is required in the exchange. Therefore the frequency of the phonons involved in the Brillouin scattering are a function of the probe wavelength in the medium and the degree of surface scattering which is frequency dependent. Whether phonon reflection from a surface can be modelled as specular depends upon the relative magnitude of the phonon wavelength to the surface roughness and correlation lengths. The experimental results indicate that the strong scattering starts at $f_b \approx 150$ GHz [by qualitative comparison of Figs. 4.1 and 4.2] which corresponds to a phonon wavelength, $\Lambda_p = s_a/f_B$, of around 50 nm depending on the speed of sound in the alloy. If the RMS surface roughness, R_{RMS}, is of the order of, or greater than $\Lambda_p/4$ in the area under the probe spot in these experiments then the scattering is diffuse and the phase and spatial coherence of the phonon flux will be lost after reflection. From the picosecond ultrasonic data a conservative estimate of $R_{RMS} \sim$10 nm is found.

In order to corroborate this result, the surfaces of the three samples were studied by AFM imaging to examine the surface topology deviation as well as the lateral

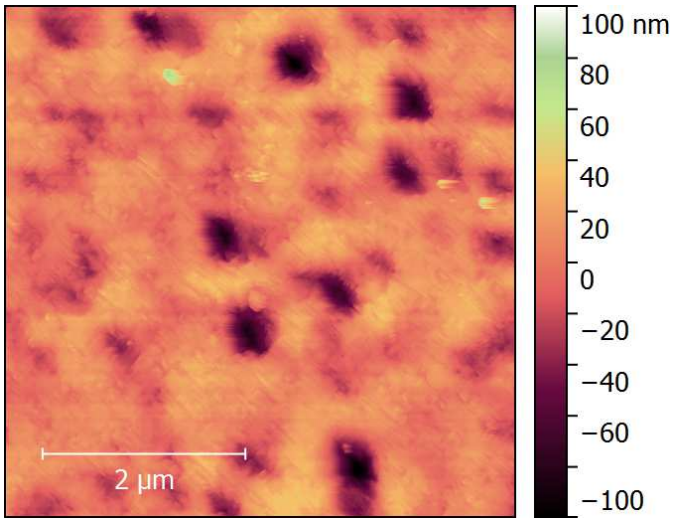

Figure 4.4: AFM image of the surface of the c-$Al_xGa_{1-x}N$ layer with $x = 0.49$, the 2 µm scale bar is shown to indicate the horizontal length scale of height variations.

length scale on which it varies. If the surface features are much larger for instance than the area of the probe spot ($\sim$ 20 µm in these experiments) then the coherence may be more likely to be conserved. The surface roughness R_{RMS} in an arbitrary $5\mu m \times 5\mu m$ square was found to be (in nm) 7 ± 3, 30 ± 14 and 20 ± 4 for films with $x = 0.42,\ 0.49$ and 0.66 respectively. The AFM image for the sample with $x = 0.49$ is presented in Fig. 4.4. The variations in the height of the surface take place with a lateral correlation length of $\sim$1 µm which is much smaller than the size of the probe spot so these features will be inherent in the optical reflectivity response. Moreover, this lateral length scale is much larger than the visible and UV probe wavelengths employed in ellipsometry measurements which means that specular reflection cannot be assumed and an angular reflection must be accounted for, depending on the size of the probe aperture. Where the lateral dimension is greater than the incident optical wavelength then a substantial intensity is lost to scattering and the assumptions of the effective medium approximation are not met. Therefore under these circumstances spectroscopic ellipsometry measurements cannot make a valid estimate of the surface roughness (see Section 4.1.1). Comparison of the picosecond ultrasonic data with the AFM measurements demonstrates the viability of measuring the surface roughness in the nitride alloys by monitoring the loss of coherence by phonon scattering at interfaces using the picosecond acoustic technique.

		c-GaN (x=0)	x = 0.42	x = 0.49	x = 0.66	c-AlN (x=1)
Thickness of the c-GaN layer (nm)			57 ± 10	49 ± 10	57 ± 10	
Thickness of the alloy layer (nm)			282 ± 12	289 ± 10	286 ± 10	
Density (kg/m^3)		6000	4824	4628	4152	3200[b]
Speed of sound (m/s)	Measured		7940 ± 380	8017 ± 340	8855 ± 290	
	Linear fit	7000[a]	8100	8283	8728	9619[b]
Direct Band Gap E_g (eV)		3.2[d]	4.4 ± 0.2 (4.47)	4.5 ± 0.2 (4.47)	4.8 ± 0.2 (4.86)	5.93[c,e]
			3.87[d],4.1[e]	3.98[d],4.2[e]	4.26[d],4.5[e]	5.0[d]
Refractive index at $E = E_g$, n		2.8[d]	2.7 ± 0.1 (2.72)	2.6 ± 0.1 (2.63)	2.6 ± 0.1(2.54)	2.9[c]
			2.4 for x = 0.46[d]			2.3[d]
Extinction at $E = E_g$, κ		0.25[d]	0.05 (0.22)	0.05 (0.16)	0.05 (0.14)	∼0.01[c]
			0.15 for x = 0.46[d]			0.15[d]
Photo-elastic parameters	α	-	10 at 4.25eV	2 at 4.3eV	8 at 4.6eV	-
			-6 at 4.55eV	-3 at 4.7eV	-4 at 4.8eV	
	β		2 at 4.37eV	1 at 4.5eV	2 at 4.8	

Table 4.2: Photo-elastic parameters of c-$Al_xGa_{1-x}N$ measured in the present work and compared with the data obtained in differing studies. The values obtained from ellipsometry data are shown in brackets. The accuracy for obtaining n and κ from ellipsometry measurements are ±0.05 and ±2.5% respectively.

[a]Refs. [75, 76]
[b]Ref. [115]
[c]Ref. [27]
[d]Refs. [26, 112]
[e]Ref. [114]

4.2 Characterisation of Free-Standing AlGaN Membranes

In this section the results from observation of ultrafast thickness oscillations excited in free-standing cubic AlGaN membranes with a thickness of several hundred nanometers are discussed. Free-standing membranes are of interest due to their potential applications in nanomechanical [120] or optomechanical systems as well as their general importance in fundamental research such as mode lifetime [104]. The fabrication of the membranes is described in detail in Section 3.2.4. The optical excitation frequency used to pump the membranes was tuned to the composition of the ternary alloy and ranged from $\lambda_{pu} = \lambda_0/3 = 250\text{-}290\,\text{nm}$. The probe wavelengths employed for the detection of the membrane oscillations were $\lambda_{pu} = \lambda_0/2 = 375\text{-}435\,\text{nm}$. There is very little absorption at these energies so the probe pulse is free to reflect from the two free surfaces bounding the membrane, much like in a Fabry-Pérot etalon. After the absorption of the pump pulse, a large amount of non-equilibrium carriers are created. Acoustic phonons are generated through the deformation potential and electron-phonon coupling, when the charge carriers transfer their excess energy to the lattice. As light at the chosen wavelengths is absorbed relatively weakly the process is dominated by the deformation potential contribution which is dependent only on the total number of non-equilibrium excited carriers because the excess thermal energy imparted to the lattice by relaxation to the conduction and valence band minima is small [103].

The small thickness of the membrane relative to the phonon wavelength leads to a confinement of the longitudinal acoustic modes much like in an optical resonator. After the excitation of the membrane, the boundary conditions given by the free surfaces lead to the formation of standing waves. It is possible to observe these vibrational eigenmodes in supported films although this method is less effective as it relies on a large acoustic mismatch to confine the longitudinal phonons efficiently and typically results in a short confinement time. The reader should be aware that elsewhere in the literature these membrane modes may be referring to the low frequency oscillation of the entire film commonly referred to as drum head modes. These modes are strongly related to the macroscopic geometry of the membrane and propagate laterally. The modes discussed here are the localised thickness oscillations, so called dilatational modes [103], which are related only to the membrane thickness. Thus the upper limit for frequency generation is dependent on the minimum membrane thickness that may be fabricated.

4.2.1 Membrane Thickness Oscillation

To obtain an expression for the frequency of the membrane thickness oscillations, the thin c-GaN buffer layer which remains on the back of the membrane after back etching must be taken into consideration. As we are only concerned with the thickness change normal to the growth plane we take the solution to the one dimensional wave equation defined in Section 2.4.1:

$$\psi(z) = A_i cos\,(k_i z) + B_i sin\,(k_i z)\,, \tag{4.5}$$

where i is an integer signifying the layer. The boundary between the GaN buffer and the AlGaN layer is designated as $z = 0$, with the position of the free surfaces of the AlGaN and GaN buffer at $z = a$ and $z = b$ respectively. The two free surfaces are traction free i.e., the stress components normal to the surface are zero, and the strain and stress amplitude must be continuous across the GaN/AlGaN interface. By solving the resultant simultaneous equations from the boundary conditions at the GaN/AlGaN interface and the two free surfaces we obtain a relation between the longitudinal speed of sound in the AlGaN layer and other known parameters:

$$\sin\left(\frac{b\omega}{s_0}\right)\cos\left(\frac{a\omega}{s_a}\right) + \frac{Z_a}{Z_0}\sin\left(\frac{a\omega}{s_a}\right)\cos\left(\frac{b\omega}{s_0}\right) = 0, \tag{4.6}$$

where a is the thickness of the c-AlGaN layer, b the thickness of the GaN buffer, s_a the speed of longitudinal sound in the c-AlGaN layer and s_0 =7000 m s^{-1} the speed of longitudinal sound in c-GaN [75]. The frequency ω is the angular frequency of the fundamental dilatational mode in the membrane. $Z_0 = s_0\rho_0$ and $Z_a = s_a\rho_a$ are the acoustic impedances of c-GaN and the alloy respectively (ρ_0 and ρ_a are the corresponding densities). The alloy density ($\rho_a = 6000 - 2800x$) is found from a linear interpolation between the known densities of the binary nitrides GaN and AlN [115].

Fig. 4.5 shows the transient reflectivity signal $\Delta R(t)/R_0$ from the membrane. The data is taken in a total measurement window of 1 ns and with a time resolution of 5 ps. Again the high amplitude spike in the initial picoseconds is a response to the slowly decaying non-equilibrium excited carriers in the film. The transient reflectivity data is displayed with the multi exponential decay of the electronic excitation subtracted for ease of presentation. This is the reason for the apparent double peaks which are an artefact of the fitting. For the duration $t = 100-800$ ps the triangle-wave-like film

thickness oscillations are observed with minimal damping across the full measurement window. That the waves appear triangle-like with sharp features indicates the presence of higher order modes. The lifetime of the fundamental mode is estimated at 1.2 ns extrapolating beyond the short measurement window.

The observed modes are dependent on both the generation and detection processes. In Fig. 2.6 the strain and displacement profiles for the lower order modes are illustrated. In order to excite a particular mode there must be a non-zero spatial overlap integral with the strain distribution of that mode. It is therefore necessary to have a non-uniform excitation to produce both odd and even modes. In these experiments the pump optical absorption length in the various samples was on the order of $\sim$100 nm which is considerably shorter than those reported in similar works. These works aim at a uniform rectangular strain distribution produced by a pump pulse with very long absorption length, as the excitation is symmetrical with respect to the center plane of the membrane only the odd acoustic eigenmodes are produced [76, 103, 104]. Nevertheless the absorption length is quite long and the whole of the membrane is excited.

Despite the even-modes being generated by an asymmetric optical excitation, the detection mechanism may not be responsive enough to the strain induced changes to observe them. There are two mechanisms affecting the optical reflectivity of the membrane, the first is the optical cavity thickness modulation and the second is the photo-elastic contribution which may affect the effective optical path length of the membrane. The even-modes correspond to an anti-symmetric displacement about the center of the membrane which results in a translation of the whole membrane. The outcome is a relative phase shift which does not affect the signal amplitude at the point of detection. The detection mechanism is not particularly sensitive to the photo-elastic changes in the sample due to the optical probe wavelengths used and therefore the film thickness variation is the dominant contribution. Only the odd vibrational modes in the membrane will modulate the optical cavity thickness.

An example Fourier spectrum across the entire measurement window for the sample with $x = 0.23$ is presented in Fig. 4.6. Several discrete acoustic phonon modes are shown the largest of which being the fundamental frequency for the membrane thickness oscillation. Only the first two odd vibrational modes are observed by this technique as the higher order modes decay following a $1/n^2$ relationship (n: mode number). It is well known that in order to generate high frequency acoustic phonons

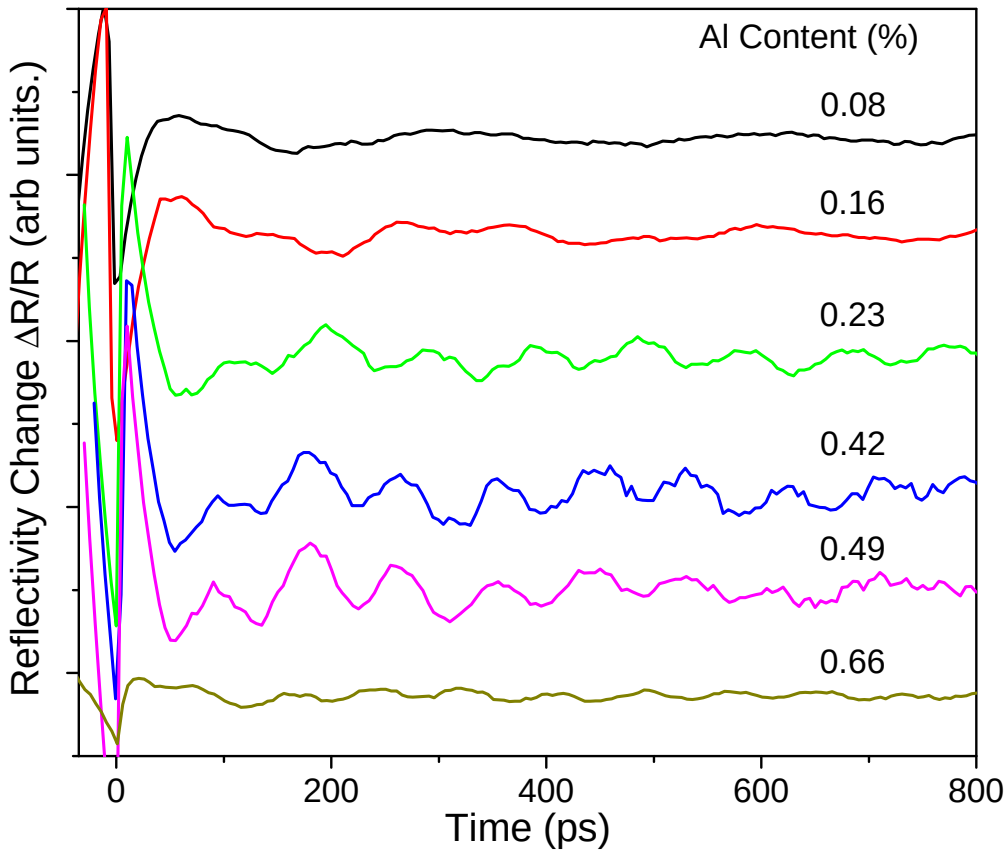

Figure 4.5: Pump-probe response for c-AlGaN membranes at different Al concentrations. Time = 0 has been set to the moment of coincidence between pump and probe pulses. Membrane oscillations are observed that persist across the entire measurement window relatively unattenuated.

both an ultrafast optical excitation as well as short wavevectors in the strain distribution are required. The sharp features desired in the strain profile, as they contain the high-frequency components in the Fourier spectral domain, are defined by the flat membrane boundaries in this case [76, 104]. A perfectly flat strain profile will generate an infinite number of eigenmodes. Unfortunately as the amplitude of higher order modes decay exponentially the experimental sensitivity was not enough to identify these modes in the frequency spectrum.

The time resolution of the acquired data was also not sufficient to identify Brillouin oscillations in the membrane as they are just above the Nyquist limit. These may be of interest as a previous study on c-GaN demonstrated a significant shift in the frequency compared to the supported film, possibly due to the release of interfacial strain in the layer. There is however some evidence for the detection of the first even-mode at

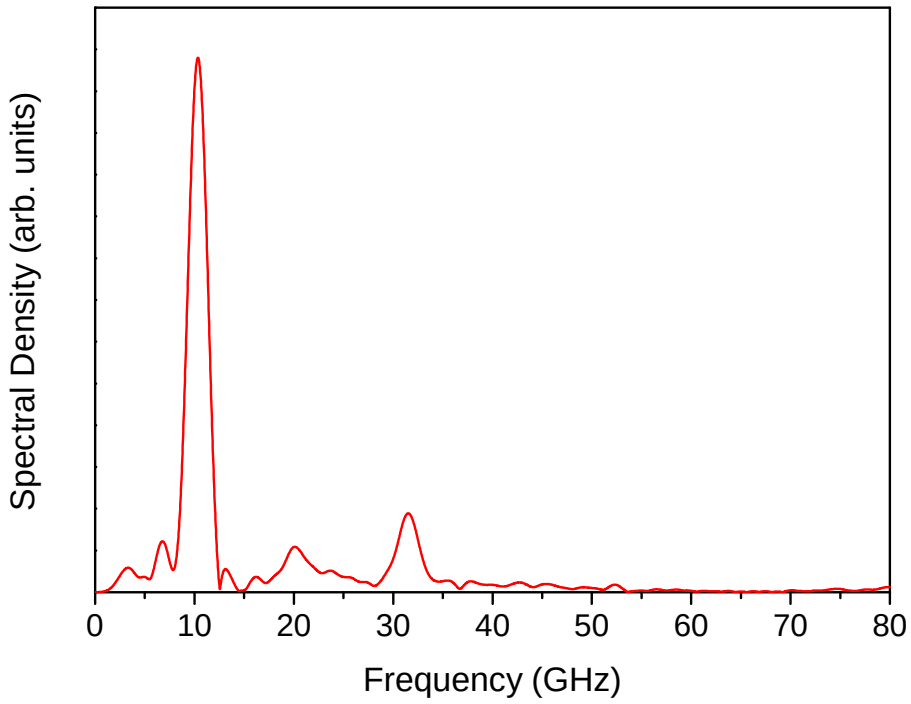

Figure 4.6: Example Fourier spectrum of SN442 c-$Al_{0.23}Ga_{0.77}N$ layer. The first two odd vibrational modes are seen due to modulation of optical cavity thickness as well as a small peak suggesting the first even mode due to photoelastic coupling.

$\sim$20 GHz which would confirm that they are indeed generated by the strain gradient in the membrane and the detection method is merely insensitive to the photoelastic changes.

4.2.2 Speed of Sound

The fundamental mode is the frequency of interest for finding a numerical solution to Eq. (4.6). This leaves us the speed of longitudinal sound as a function of aluminium content as shown in Fig. 4.7, alongside a linear fit between the known velocities in the binary alloys. For the dilatational modes of a free standing membrane the mode frequency is dependent only on the film thickness which was measured by ellipsometry. Thus the error in the calculated values for speed of sound are almost entirely dependent on the accuracy of film thickness measurement. The accuracy of judging layer thickness in multilayer films is complicated by the covariance of the parameters between the two layers, that is, the total thickness is more certain than the separate values. For this reason the mean square error of the ellipsometry model is significantly higher for the

samples with low Al content where the optical parameters are quite similar between the layers. This bears itself out in the data which deviates much further from the linear trend line at lower values of x.

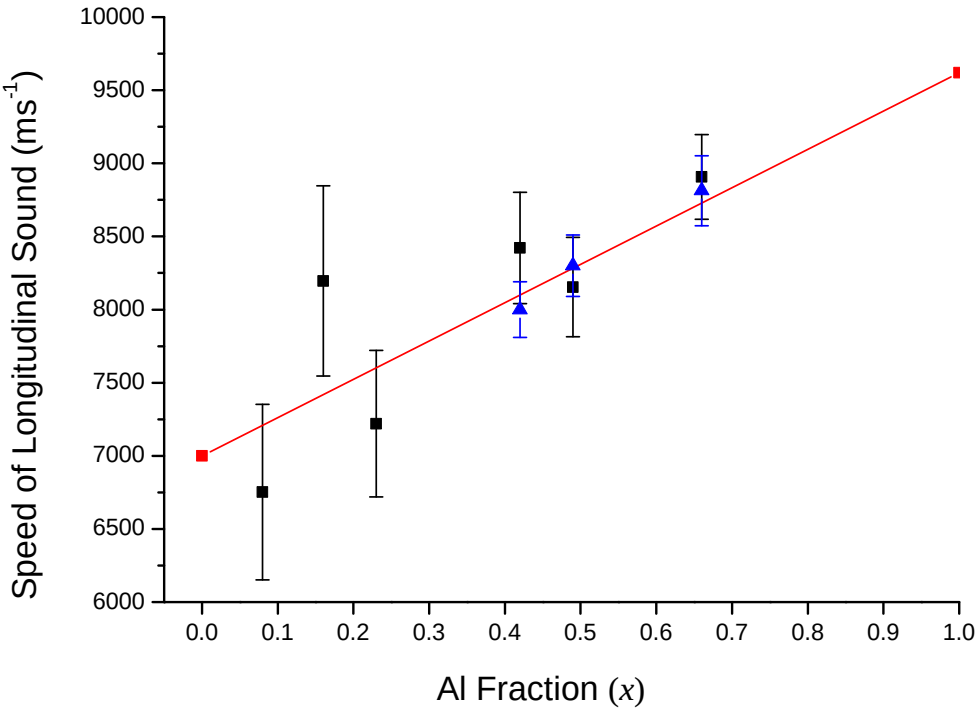

Figure 4.7: Speed of longitudinal sound in $c-Al_xGa_{1-x}N$ dependence on aluminium fraction calculated from membrane modes (black squares) and Brillouin oscillations (blue triangles). The red line shows an interpolation between the known values for the binary alloys.

It is possible to determine the speed of sound from the frequency of Brillouin oscillations where the optical constants are known however there are compound errors in the optical density, angle of incidence and optical wavelength. The calculated velocities are presented alongside those derived from the optical cavity thickness modulation. The fit to the trend line is significantly better and with a reduced error as the accuracy of film thickness measurements was quite poor. There is no experimental evidence of a bowing factor affecting the C_{33} elastic constants in these results as the relationship appears linear allowing for the level of error.

4.3 Conclusion

In summary, a series of cubic AlGaN wafers of varying group-III ratios and with sub-μm thickness were prepared on (001) GaAs substrates by pa-MBE. Subsequently free-standing membranes were fabricated by back etching through the GaAs substrate. Picosecond acoustic techniques were applied to monitor the coherent phonon dynamics in the membranes and supported films in order to extract the physical and optical parameters. Observing the frequency of Brillouin oscillations in the time domain of femtosecond pump probe spectroscopic data in conjunction with ellipsometry data returned the refractive index and extinction coefficients for three samples with aluminium fraction around 50%. After removing the substrate it was observed that the optical cavity thickness modulation became the dominant mechanism for interferometric response and thus the first two odd modes are clearly observed in a series of $c - Al_xGa_{1-x}N$ free-standing membranes with x ranging from 0 to 0.66. Extracting the frequency of the oscillations in the time domain, the speed of longitudinal sound in the alloy as a function of aluminium content was determined.

Chapter 5

Characterisation of Cubic (AlGa)N Microstructures

There remains a considerable current interest in the properties and applications of semiconductor multilayer systems. The advantages of employing cubic nitride materials for this purpose lie in the ability to grow heterostructures in which the intrinsic strain is not accompanied by an associated in-built electric field. The complications arising from using lattice mismatched substrates for cubic nitride growth are only compounded when trying to grow nanoscale heterostructures. The samples tend to suffer from a high degree of surface roughness which increases with growth time. Raising the growth temperatures to enhance surface mobility and reduce interface roughness is limited by a corresponding increase in breakdown of the metastable cubic phase. The poor quality of available material has until recently hampered research efforts where surface roughness and inhomogeneities are on the order of layer thicknesses. This chapter reviews the experimental and theoretical aspects of picosecond acoustic studies conducted on cubic nitride heterostructures. It is subdivided into two sections devoted to one specific sample structure each, namely single c-GaN quantum wells and cubic GaN/AlN superlattices. The focus is on the application of these structures as tools for the generation and detection of the short wavelength THz phonons required for high resolution acoustic nanoscopy of photonic devices with length scales on the order of nanometres. Section 5.1 explores the use of single c-GaN quantum wells as selective strain transducers with a high temporal resolution. Subsequently cubic nitride superlattices are investigated as tools for the generation of quasi monochromatic THz phonons in Section 5.2.

There exist many contemporary techniques for the metrology of semiconductor samples with nanometer accuracy. If the sample surface is of interest then AFM mea-

surements may trace the surface profile with up to sub-nanometer precision. Where depth information is also required, the sample may be cleaved and the cross section examined by SEM. This remains however a destructive technique that is not viable where the sample may not be cleaved or may be destroyed in the process, for instance when working with single celled organic matter [121]. Ellipsometry may be very effective, as demonstrated in the previous chapter, for characterisation of simple structures and thin films, yet for stacked structures with multiple unknown layer thicknesses or constructed from materials for which the optical constants are not well defined the solutions rapidly become ambiguous due to the large number of covariant terms in the model.

The standard technique for non-invasive microscopy in medical science is ultrasound imaging. The acoustic waves are generated by piezoelectric transducers that operate between 1 and 18 MHz. The reflected echoes are then detected by the same acousto-electrical transducers that produce the original signal [60]. State of the art techniques using highly focusing acoustic lenses are able to increase the lateral resolution of such techniques to $\sim$1 µm with maximum phonon frequency $\sim$1 GHz [122]. Improvements in the lateral resolution in the images produced are contingent on increasing the acoustic frequency and resolving successive echoes discretely which requires faster electronics [123]. Both of these problems are easily solved by switching to an all optical generation and detection scheme.

5.1 Cubic GaN Quantum Wells for Strain Generation and Detection

A principle characteristic of acoustic microscopy is the ability to discretely resolve successive echoes reflecting from internal regions of the sample with varying acoustic impedances. Where the length scale of these regions of varying acoustic impedance is on the order of or smaller than the width of the excited strain pulse it becomes difficult to parse the data as serial reflections overlap. In order to temporally resolve between successive echoes reflecting from buried interfaces and structures in optically opaque materials the detection scheme must meet a few key criteria. One of these is that the detection must take place in a sufficiently small length or volume such that the precise position of the strain pulse becomes known. As in the previous chapter, detecting strain in bulk material will allow for the observation of the presence of strain

in the form of coherent Brillouin oscillations, however this contains no information on the actual location of the strain pulse or the amplitude profile of the acoustic wave. Therefore, it is important that only a minimal area is sensitive to the acoustic changes by photoelastic effect or interface displacement. Another criteria is that the material must respond optically to the strain with picosecond rise times otherwise the spatio-temporal information of the acoustic pulse will become washed out. Finally, the characteristic time of the acoustic pulse should be short enough that reflections from inhomogeneous regions may be separately resolved.

There are a variety of systems that are proposed to meet these criteria by detecting the strain electrically at a heterojunction. In these devices the transit of an acoustic pulse across the depletion zone produced at a p-n junction or Schottky diode is detected in the transient current change brought about by the piezojunction effect [124, 125]. Still, the temporal resolution in these studies is limited by the effective capacitance and load resistance of the devices [123]. Even where these may be reduced by advanced processing techniques, the bandwidth of the readout electronics has limited signal rise times to upwards of 30 ps to date [124]. Another novel technique is measuring the variation in the population of photoexcited carriers in a GaAs QW embedded in a p-i-n device by changes in the photocurrent generated by incident light as the QW excitonic resonance is modulated [126]. This gives resolution on the order of picoseconds but requires the growth of complex devices on samples to be imaged. Optical detection may observe changes in the transient reflectivity with sub-picosecond temporal resolution. This may be accomplished by two methods. The first is using a high photon energy probe pulse to limit the scope of the detection to the absorption depth of the laser pulse at the sample surface [62,85]. Secondly, where depth information is desired then buried layers are required. Most commonly studied are QWs as they possess the reduced dimensionality required to provide the greatest spatial sensitivity [68,119,126].

The optical reflectivity of the QW responds to the strain passing across it as the interfaces are displaced and by the photoelastic effect. The advantage of QW structures is that the band edge of the barriers cladding the wells are necessarily higher than those in the well for type 1 QW structures such as those studied here. This is reflected in the variation of the electronic resonances and the dispersion of the refractive index. As such, where the wavelength is properly selected then the probe beam will be insensitive to the strain in the barrier layers and sensitive only to acoustic perturbations in the QW [68]. In this section the results of picosecond acoustic experiments on three

samples with single cubic GaN quantum wells bounded by c-$Al_xGa_{1-x}N$ barrier layers. The barrier layer compositions for each sample are presented in Table 5.1.

5.1.1 Single c-GaN QW Structure and Experimental Methodology

The QW samples were produced by the same basic methods outlined previously for the growth of cubic nitrides [c.f. Section 3.1]. A schematic of the sample structure is illustrated in Fig. 5.1(a). The structures are deposited onto a 350 µm GaAs (100) substrate. Firstly a thin GaAs buffer is used to initiate and sustain cubic growth. Then the actual sample structure is laid down, it consists of a 100 nm c-GaN layer followed by a further two c-AlGaN barrier layers of thickness 100 nm and 10 nm respectively cladding the c-GaN QW which has a nominal thickness of 2 nm. The QW photoluminescence (PL) spectra presented in Fig. 5.1(b) was recorded by Ross Powell at the University of Nottingham. There is a shift of the peak emission energy (3.415 eV) of the well from that of bulk c-GaN (3.2 eV) [26]. The observed PL peaks correspond to confined energy states in the well rather than band edge transitions observed in bulk material. This combined with the discrete energies for the well and barrier indicates that an abrupt junction has been achieved and the QW is properly functioning. The Al content of the barrier layers has been estimated by comparison with the PL emission from bulk c-$Al_xGa_{1-x}N$ material with known compositions. Due to the differences in growth conditions and internal strain for the two samples this is unlikely to be highly accurate but provides a useful reference in lieu of SIMS data.

Wafer No.	**Nominal barrier AlN fraction (x)**	**Al effusion cell flux ($\times 10^{-}8$ torr)**	**Estimated barrier AlN fraction (x)**
SN647	0.3	945	0.16
SN646	0.5	975	0.5
SN649	0.7	996	-

Table 5.1: Sample specifications for all studied GaN/c-$Al_xGa_{1-x}N$ QWs. The barrier Al fraction is estimated from the photoluminescence data where possible.

Picosecond acoustic experiments were conducted on three cubic GaN quantum well samples for c-$Al_xGa_{1-x}N$ barrier layers with $x = 0.16$, 0.5 and 0.7. Measurements were recorded in two experimental configurations. In the first case the strain pulse is excited predominantly in the GaAs substrate with a pump energy of $\lambda_{pu} = \lambda_0/2 = 420$ nm. The strain pulse is detected in the QW near to the sample surface with a

probe beam of $\lambda_{pu} = \lambda_0/3 = 280\,\text{nm}$. The second, with the intention of exciting a narrow strain pulse with high frequency spectral components, the quantum well is excited with a femtosecond laser pulse from the third harmonic of the fundamental laser output where $\lambda_{pu} = 283\text{-}295\,\text{nm}$. This pump energy is tuned well above the hh1-e1 transition in the well. The full extent of the sample is then probed with deeply penetrating $\lambda_{pr} = 425\text{-}445\,\text{nm}$ radiation.

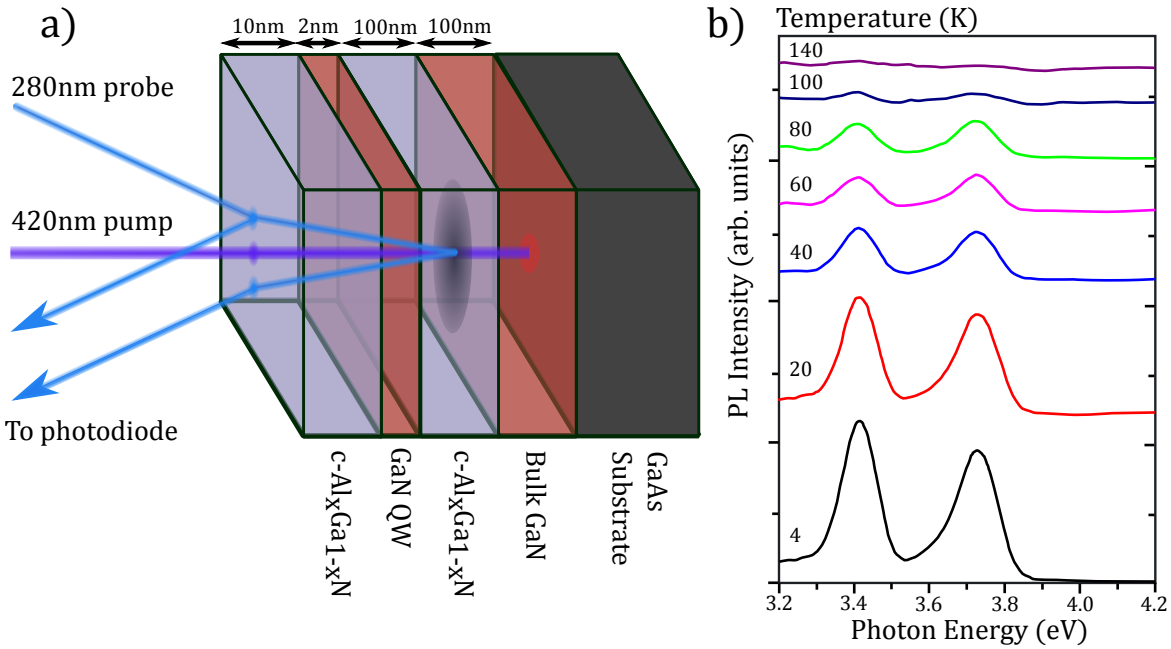

Figure 5.1: a) Schematic diagram of the pump-probe configuration and sample structure for measurements on cubic GaN quantum wells clad by c-$Al_xGa_{1-x}N$ barrier layers. The acoustic pulse is represented by the shadow propagating away from the site of pump incidence on the substrate. b) Photoluminescence spectra from the cubic $Al_{0.3}Ga_{0.7}N/GaN/Al_{0.3}Ga_{0.7}N$ QW samples showing the blueshifted emission peaks from the GaN well.

5.1.2 Phonon Generation in the Well

In order to interpret the experimental data it is crucial to understand the phonon generation process in the well as the excited carrier distribution may effectively become imprinted on the shape of the travelling strain pulse. As detailed in Section 2.1 the acoustic strain is generated by the carrier distribution through the deformation potential and carrier relaxation towards the band edges. It has been shown that the acoustic generation process can be treated in the semiclassical case detailed previously, so long

as the carrier densities are replaced with the corresponding probability expectation values. For the case of a quantum well containing a static population of electrons and holes excited to their jth states then Eq. (2.11) may be transformed to

$$\sigma_{zz} = \rho\nu\eta_{zz} - 3B\beta(T(z,t) - T_0) + \frac{\partial E_c}{\partial \eta_{zz}} N_e \left|\phi_j^{(e)}(z)\right|^2 - \frac{\partial E_v}{\partial \eta_{zz}} N_h \left|\phi_j^{(h)}(z)\right|^2, \qquad (5.1)$$

where the superscripts (e) and (h) refer to the wavefunctions for electrons and holes in the well respectively. The deformation potentials are also position dependent quantities as they differ between the well and barrier. The values of N_e and N_h refer to the total number of carriers in the volume applied for the normalisation of $\phi_j^{(e,h)}$. For optical excitation and no intentional doping it is assumed here that $N_e = N_h$. The value of this constant is estimated by calculating the absorption profile of an individual pump pulse using the extinction coefficients and layer thicknesses. The absorbed photon number in the well is equated to the number of excited electrons and holes. The envelope function approximation [88, 90] is used to characterise the position expectation value in the well. To simplify the situation a square well potential is assumed for all carriers independently in the Schrödinger equation for the envelope function

$$\left\{ -\frac{\hbar^2}{2m_\mu(z)} \frac{\mathrm{d}^2}{\mathrm{d}z^2} + V_\mu(z) \right\} \phi_{j,\mu} = E_{j,\mu}\phi_{j,\mu}, \qquad (5.2)$$

where the suffix μ denotes the particle type (i.e. light hole, heavy hole or electron). The effective masses m_μ and deformation potentials are extrapolated from the values for binary nitride compounds in [29]. The boundary conditions for the wavefunction envelope are such that $\phi_{j,\mu}$ and $1/m_\mu \cdot d/\phi_{j,\mu}/dz$ are continous at the interface between the barrier and well. The contribution from the thermal stress is estimated to be only ~ 0.12 of the magnitude of the electronic stress ignoring non-radiative recombination processes. This estimate comes from an analysis of the deformation potential contribution from each excited electron versus the thermalisation energy, as the electron relaxes to the band edge. The effects of thermal diffusion are neglected here but would only act to further smear out this negligible contribution. As an example Fig. 5.2 panels (a) and (b) depicts the normalised wavefunctions for the electrons and holes excited to the lowest energy bound state in the $GaN/Al_{0.5}Ga_{0.5}N$ quantum well respectively. There is a minimal amount of penetration of the wavefunction into the barrier layers.

The corresponding induced strain pulse as calculated is shown in Fig. 5.2(c). The

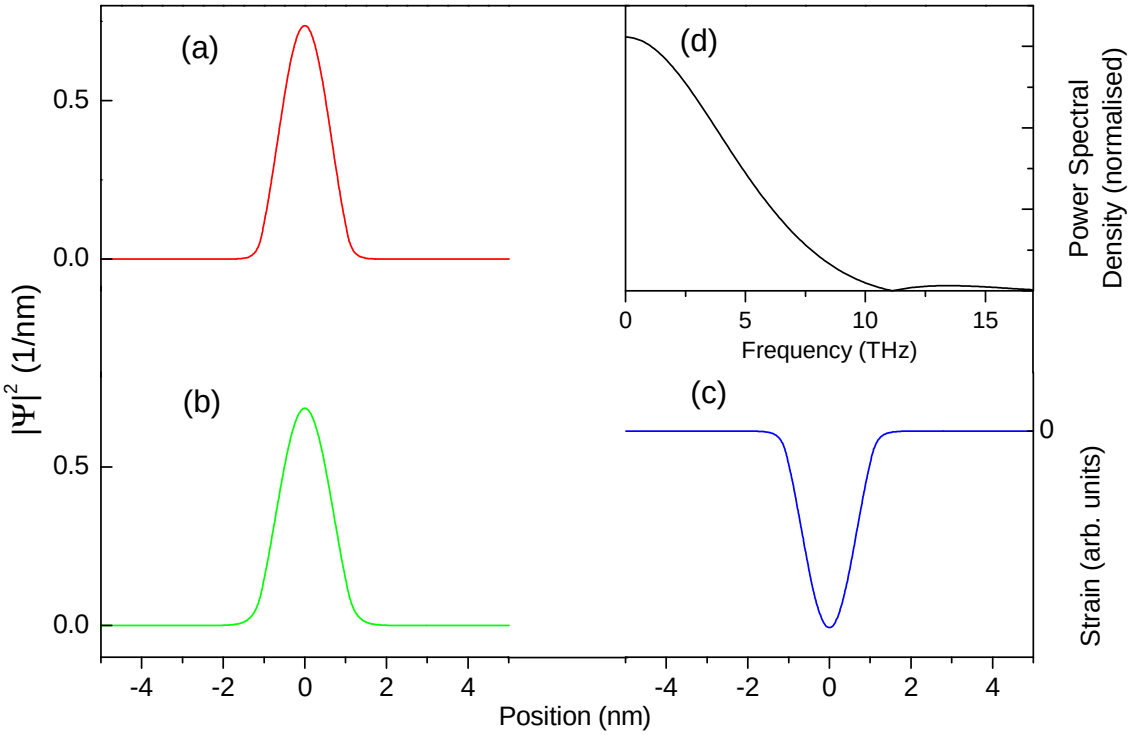

Figure 5.2: a) The position expectation value of $|\Psi|^2$ for (a) the $e1$ electronic state and (b) the $hh1$ heavy hole state for a GaN/$Al_{0.5}Ga_{0.5}N$ quantum well of width 2 nm. The presence of excited carriers in these states generates the strain profile (c) whose frequency spectrum is shown in (d).

strain pulse is composed of a sum of contributions from the electron and hole deformation potentials, the induced hydrostatic stress launches a strain pulse of identical shape in opposite directions ($\pm z$). The spatial extent of the produced strain pulse is similar in scale to the width of the quantum well and has a temporal width of 0.5 ps. Fig. 5.2(d) displays the spectral content of the waveform from a temporal Fourier transform of the strain pulse, showing that phonons with frequencies ranging up to 10 THz are efficiently generated.

As the strain pulse propagates away from the QW in both directions it is attenuated proportionally to $\omega^2(k_BT/\hbar)^3$. Therefore in these room temperature experiments the strain pulse will not retain its shape across even short propagation distances. The largest acoustic impedance mismatch between the GaN and $Al_{0.7}Ga_{0.3}N$ layers leads to an acoustic reflection coefficient for strain at the interface of only $\sim \pm 0.10$ so the influence of multiple reflections will be neglected in the final analysis. It may

be presumed that the surface roughness and non-homogeneities at the interfaces will further serve to wash out the high frequency strain components.

5.1.3 Reflectivity Modulation Results

At first the results obtained for the geometry where the strain pulse is excited at the GaAs/GaN interface are discussed. The frequencies are tuned to optimise optical generation in the GaAs substrate and detection in the QW. Presented in Fig. 5.3 are the results for relative reflectivity $\Delta R(t)$ measurements obtained on all three QW samples with a probe wavelength of 280 nm alongside the FFT of the data in the measurement window from 5−50 ps. At $\tau = 0$ the pump pulse is incident on the substrate.

The immediately obvious dominant features are periodic reflectivity modulations related to Brillouin scattering from the GaN buffer layer and AlGaN barrier layers. Two clear yet broad peaks are present in the FFT for all barrier compositions, the lower frequency peak (∼100 GHz) is attributed to the GaN buffer layer and the higher frequency peak (∼160 GHz) to the AlGaN barrier and have been marked with arrows in Fig. 5.3 respectively. The increase of longitudinal speed of sound with increasing aluminium content is expected to be associated with a proportional increase in the Brillouin frequency. Therefore it is surprising that the peak frequencies in the barrier layer are located so closely together, especially for the sample with $x = 0.16$ for which peak is clearly distinct from the GaN layer despite their apparent similarity in composition. The strain effects on the refractive index in this multilayer heterostructure are unknown and most probably play some significant role.

The expected arrival time of the strain pulse from the GaAs substrate at the QW comes at approximately 25 ps based on the nominal thicknesses and expected longitudinal acoustic velocity. Unfortunately there is no clearly discernible signal related to the presence of the well at this time because it is overshadowed in all three cases by Brillouin scattering from the barrier layers. This may be anticipated for the sample with the lowest aluminium content as a similar result was observed for a cubic AlGaN/GaN QW with the barrier having $x = 0.1$ in similar experiments conducted at the University of Dortmund [68]. In this circumstance the similarity in optical properties between the various layers are insufficient to resolve the QW independently and the sample may be treated as a homogeneous block. However for samples with greater aluminium content a clear signal relating to the presence of the QW at the surface was

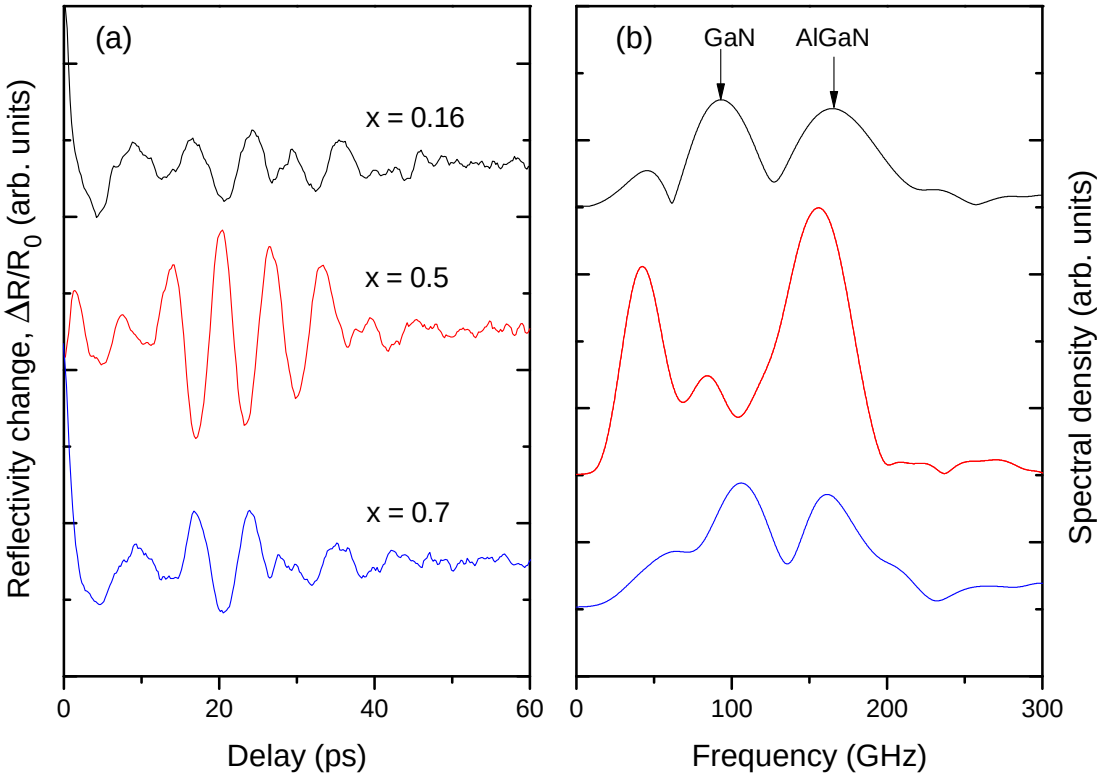

Figure 5.3: Transient reflectivity response for QW samples probed at $\lambda_{pr} = 280\,\text{nm}$. Panel (a): Temporal profile of the reflectivity modulation for c-$Al_xGa_{1-x}N$/GaN QWs with x = 0.16, 0.5 & 0.7. Panel (b): The fast fourier transform of the signal data in the time domain. The arrows indicate the peaks corresponding to Brillouin oscillations from the GaN and AlGaN layers independently. Time = 0 has been set to the moment of coincidence between pump and probe pulses.

observed. The inability to detect the QW here is attributed to the much smaller size of the well, 2 nm compared to 10 nm, such that the integral of the strain effects in the detection region make a negligible impact on the final signal and the fact that it was not possible to select the detection photon energies to sufficiently screen the presence of the AlGaN barriers while also exciting a strain pulse for any of the studied values of x. It may be worth noting at this point that single colour (400 nm) pump-probe spectroscopy was investigated on these samples but no significant differences in the results were recorded. Since there is no signature from the QW in the results obtained in this experimental geometry no further discussion will be provided on this data.

The same experiments were repeated for these three samples with the pump and

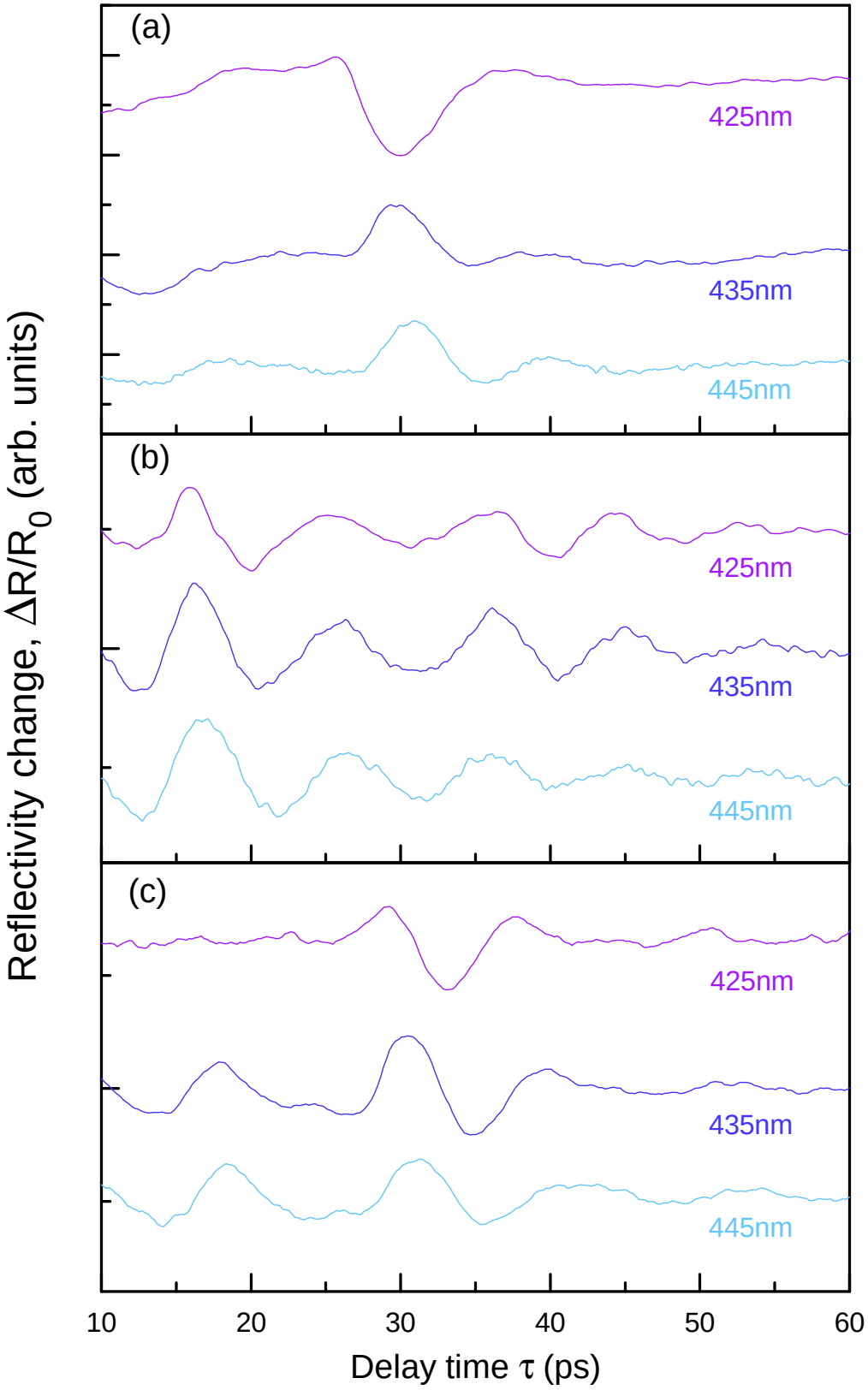

Figure 5.4: Pump-probe response for c-$Al_xGa_{1-x}N$/GaN QWs with x = (a) 0.16, (b) 0.5 & (c) 0.7 at three different indicated probe wavelengths λ_{pr}. Time = 0 has been set to the moment of coincidence between pump and probe pulses. The strain from the QW arrives beginning at approximately 26 ps.

probe sources reversed, predominantly exciting strain in the QW and detecting throughout the grown film and in the near surface of the substrate interface. Three wavelengths λ were studied that lie in the optimal window for laser operation and above absorption in the GaN layers of the pump pulse. The samples were strongly optically excited with a pump energy well above that required for electronic transitions in the QW but below the band edge for the barrier layers, while the sample is probed throughout all epilayers and even into the substrate. The results for the samples with $x = 0.16$, 0.5 and 0.7 are presented in Fig. 5.4 panels (a), (b) and (c) respectively for the studied optical wavelengths.

Firstly the temporal reflectivity modulation is described in detail. Initially it may be seen that in Fig. 5.4(a) and Fig. 5.4(c) the Brillouin oscillations observed in the previous experimental configuration are strongly suppressed and in their place is a simple waveform with single unipolar and bipolar peaks appearing at $\sim$15 ps and $\sim$26 ps. These times correspond quite well to the theoretical time of flights for a pair of longitudinal acoustic pulses propagating from the surface side of the GaN layer and the QW to the substrate respectively. The detection mechanisms are enhanced in the GaAs substrate because there is a maximum in the dispersion of the complex refractive index at this photon energy [127]. Regarding the reflectivity profile in Fig. 5.4(b), the contribution from discrete strain pulses in either the substrate surface or quantum well cannot be easily discerned as the Brillouin scattering is significantly stronger for reasons obviously related to the specific growth conditions. Seeing as the wavelength λ is not in the vicinity of the band edge the photoelastic parameters of neither the barrier or buffer layers are expected to be in resonance the exact mechanisms are unknown to the author and these results will not be discussed further.

The suggested reason for the supression of the additional early peaks in Fig. 5.4(a) is that there is still significant absorption in the $Al_xGa_{1-x}N$/GaN layers for this value of x and so the GaN buffer layer is not strongly excited by the mostly depleted pump pulse. The signal feature at $\sim$26 ps is attributed to the strain pulse generated in the QW and described in Fig. 5.2. The initial temporal extent of this strain pulse is estimated to have sub-picosecond duration, however these experiments are conducted at room temperature with a large thermal phonon bath interfering with the strain pulse as well as the Herring attenuation which scales quadratically with phonon frequency [95]. Consequently the strain pulse is significantly broadened by the time the pulse arrives at the substrate and the high frequency components are not observed after propagation.

The resultant reflectivity modulation is the product of a convolution between interface displacements at the GaN/GaAs interface and the photoelastic coefficients in GaAs. The fact that the peak is inverted in Fig. 5.4(a) for 425 nm implies that the optical signal is predominantly governed by the deformation potential as opposed to interface displacement, because the GaAs photoelastic constants undergo a sign change in this region [127].

The reflectivity modulation arising from the strain pulse generated in the QW ∼26 ps has a bipolar appearance and a longer temporal duration than the unipolar strain pulse from the buffer layer. As the QW is embedded very close to the sample surface and the strain pulse is ejected in both directions perpendicular to the growth plane, the strain pulse and its reflection from the surface undergoing a π-phase change will form a continuous strain profile. The difference in appearance between the two strain pulses demonstrates that this sample is functioning as a detector able to effectively raster the strain profile and resolve individual pulses from a cubic GaN quantum well on a picosecond timescale. This also shows the advantage of generating strain in buried layers, by avoiding surface reflection the characteristic lifetime of the strain pulse is halved. The theoretical limit to the resolution of this detection mechanism is defined by the thickness of the detection region and found to be $\xi/v_{GaAs} = \sim 3.2$ ps (where ξ is the absorption depth), but the acoustic pulse did not contain sharp enough features to verify the resolution limit.

5.2 Study of Coherent Folded Phonons in Cubic Nitride Superlattices

As briefly discussed in Chapter 2, the behaviour of phonons in a superlattice is significantly different to that observed in bulk material due to the additional periodicity of the structure. This section of the thesis concerns results obtained from experiments using a cubic GaN/AlN superlattice to detect coherent folded longitudinal acoustic (FLA) phonon modes. Optical to acoustic transduction in semiconductor superlattices (SLs) and the properties of zone folded modes have been studied extensively in structures such as GaAs/AlAs [69]. The additional periodicity of the elastic properties along the growth direction of the superlattice structure gives rise to zone folding of the acoustic branches within the Brillouin zone (BZ), which allows optical excitation of coherent acoustic phonons with first-order frequency v_{SL}/D_{SL}, where v_{SL} is the

speed of sound in the SL and D_{SL} the SL period, in the sub-THz range. In GaN/AlN SLs based on the, more common, wurtzite (hexagonal) crystal structure, excitation of >1THz FLA phonons has been demonstrated [107]. This high frequency is due to the naturally higher value of v_{SL} in GaN/AlN than in GaAs/AlAs. The other technique available for increasing the frequency is the further shrinking of the period of the SL which, notwithstanding the fundamental limits, is additionally accompanied by complications associated with maintaining order in the artificial periodicity.

Recently there has been a lot of interest in cubic III-Nitride structures, which are not subject to the same spontaneous and piezoelectric polarization fields as the hexagonal structure, which may be deleterious for some optoelectronic applications. The internal fields in hexagonal nitride multilayer structures may actually be beneficial in phonon research and have already been exploited to enhance the detection mechanisms in transmission geometry [72]. What cannot be overstated is the difficulty inherent in the manufacture of high quality multilayer structures. This, combined with the fact that the samples not possessing any piezoelectricity in the [100] crystal direction have reduced sensitivity to free carrier population induced changes has led to a stalling in cubic nitride research output. Recent improvements in growth techniques have made the production of cubic nitride heterostructures possible, although the material quality still leaves a lot to be desired from a commercial perspective.

Quantum wells remain broadband transducers with a high frequency cutoff defined by the layer thickness or absorption length at both the points of generation and detection. The availability of monochromatic phonon sources at ultrahigh frequencies with their wavelength in the nanometer range would be of great interest for the study of the elastic properties of nanostructures, imaging of buried nanostructures by high resolution acoustic microscopy, or to allow for the conception of acousto-optic devices operating at the picosecond time scale [128]. SL structures may also find applications as acoustic mirrors or filters (e.g. band-pass) or to limit thermal conductivity in phononic devices [129].

5.2.1 Experimental Setup

For these experiments aiming to detect the presence of short lifetime high frequency modes a fast scanning delay line (optical shaker) is set in place after the motorised delay stage. This reduces the total duration of the measurement window but allows

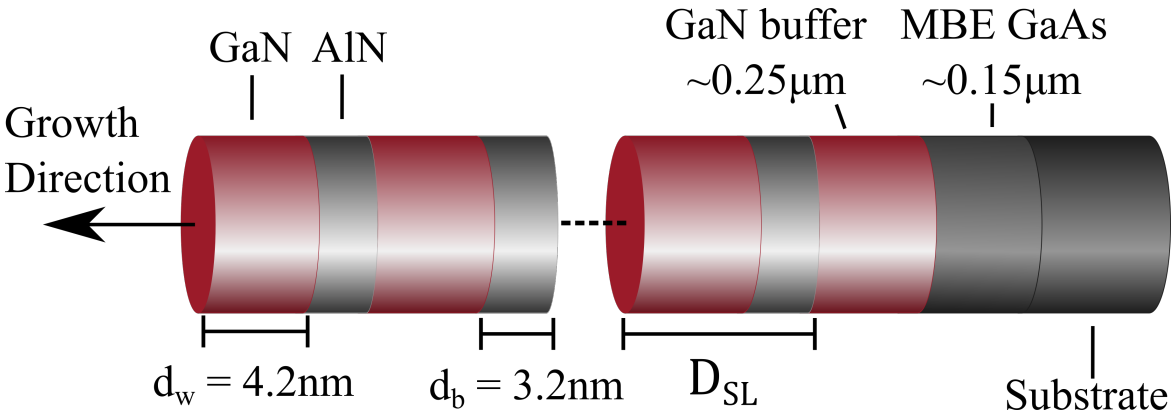

Figure 5.5: Schematic of GaN/AlN superlattice. The widths of the wells d_w and barriers d_b are indicated. L denotes the length of the entire superlattice structure. The period of the superlattice is $D_{SL} = d_w + d_b$.

for the fast averaging of a high number of scans, which is beneficial for the study of high frequency FLA modes with short characteristic lifetimes. All other elements in the experimental setup remain as described in Chapter 3. For the experiments described in this section a 20-period c-GaN/AlN superlattice was grown by molecular beam epitaxy on GaAs (100) substrate, with nominal well and barrier thicknesses of 4.2nm and 3.2nm respectively. GaN and AlN comprising the well and barrier regions respectively. A diagram of the growth schematic is presented in Fig. 5.5 depicting the alternating arrangement of each constituent material in the growth direction. The binary materials are chosen to avoid the additional complication of compositional inhomogeneities between layers introducing additional disorder. At the start a small GaAs layer is grown as the excess arsenic acts as a surfactant to initiate cubic growth, subsequently a GaN buffer is grown to allow the strain to relax into dislocations before the SL structure is deposited.

The acoustic strain is generated in the SL in two regimes: firstly by tuning the photon energy of the pump to just above the first excitonic interband transition in the well region but below that of the barrier, which establishes a strain profile with the periodicity of the superlattice and, secondly, by optically pumping the GaAs substrate which launches a strain pulse into the SL. In the first regime the superlattice is used to acousto-optically transduce strain in both directions (i.e., it is both generator and detector). The SL is pumped with photons of $\lambda_{pu} = \lambda_0/3 = 257\,\text{nm}$ and probed with $\lambda_{pu} = \lambda_0/2 = 335\,\text{nm}$. In the second configuration the GaAs substrate is excited with a pump energy of $\lambda_{pu} = \lambda_0/2 = 435\,\text{nm}$while the strain pulse is detected in the super-

lattice with a probe beam of $\lambda_{pu} = \lambda_0/3 = 290\,\text{nm}$. These two configurations will be hereafter be referred to as the detection and generation geometries respectively. Measurements were taken in a maximum window of 50 ps total duration and the Fourier transform spectra presented are calculated across the maximum measurement window.

As with a single laser pump-probe setup the pump and probe wavelengths covary there is often a trade-off in the efficiency of either the excitation or detection mechanisms. The choice of optical pump wavelength is in general less important than the detection wavelength; this should be ideally selected to match an excitonic resonance due to the small signals involved. The optical reflectivity response in the time domain is compared to the expectation values of detected frequencies based on a quantitative calculation of the theoretical phonon dispersion in the SL. Finally picosecond acoustics is demonstrated as a diagnostic tool, by comparing the nominal dimensions of the SL to the observed phonon dispersion a more accurate value for the superlattice period may be determined.

5.2.2 SL Theory and Calculated Dispersion

A consideration of the Bragg conditions within a superlattice governing constructive and destructive interference from reflections originating at multiple interfaces reveals how the phonon dispersion is altered by the large scale periodicity. The condition for maximum intensity in Bragg's equation is,

$$n\lambda = 2D_{SL}\cos\theta \tag{5.3}$$

where λ is the wavelength; θ is the wave angle of incidence measured relative to the normal of the interfaces; D_{SL} the separation between layers (i.e. SL period); and n is an integer signifying the order of interference. For large layer spacings, such as those in a superlattice, the Bragg conditions are satisfied by acoustic phonons [130]. Consider phonons propagating perpendicular to the SL growth direction, i.e., $\theta = 0$. The Bragg condition in reciprocal space is then ,

$$2q = mG_0 \tag{5.4}$$

where the basic reciprocal superlattice vector has a magnitude $G_0 = |G_0| = 2\pi/D_{SL}$.

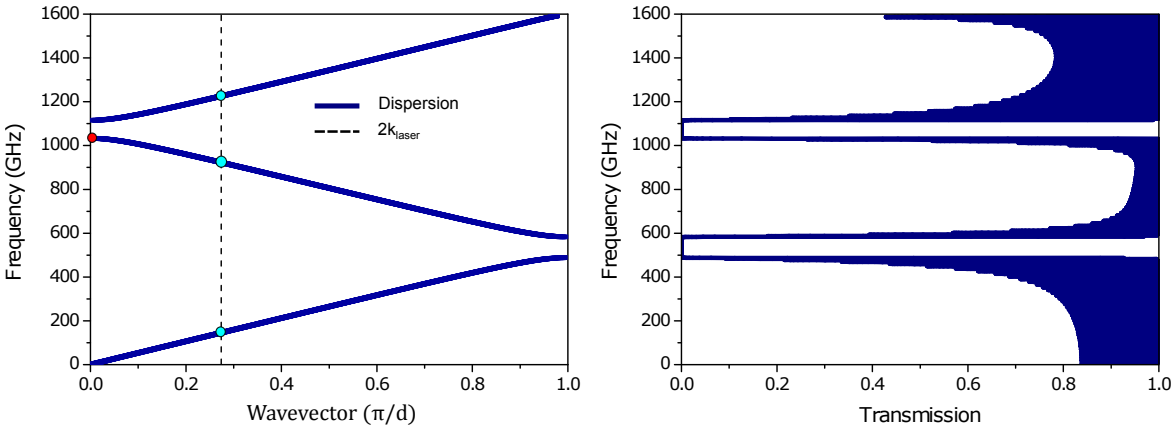

Figure 5.6: a) Calculated phonon dispersion for a cubic GaN/AlN superlattice with d_w = 4.2 nm and d_b = 3.2 nm. The wavevector corresponding to $2k_{laser}$ represented by the dashed line. The blue circles indicate the frequencies at which detection is most efficient and the red circles where generation is optimised. b) The corresponding phonon transmission frequency dependence calculated for a SL of 20 periods and of the same dimensions and materials as above.

Hence phonons with wavevector $q = m\pi/D_{SL}$ are Bragg-reflected in the SL and cannot propagate through. The acoustic dispersion may be represented in the reduced zone scheme by folding it back on itself at these phonon wavevectors into a mini-Brillouin zone of width π/D_{SL}. Frequency gaps - or "phonon stop bands"- are expected to open up at the centre and boundaries of the reduced zone due to the mismatch in acoustic impedances of the adjacent layers.

Quantitative calculations of the theoretical phonon dispersion and transmission relations are a useful tool both for the design of optimal devices and the analysis of experimental data e.g., identifying observed modes. The phonon dispersion in a SL can be obtained by applying the Rytov elastic continuum model, which is a general model concerning phonon propagation in all layered media [131]. The model is strictly only valid for an infinite superlattice, which is required for the condition of perfect periodicity, however the errors introduced for applying the model in the case of a non-infinite SL have been investigated and found to be insignificant for SLs with N>20 where N is the period number [132]. The calculated phonon dispersion for an arbitrary SL in this model is given by,

$$\cos(qD) = \cos\left(\frac{\omega d_w}{v_w}\right) + \cos\left(\frac{\omega d_b}{v_b}\right) - \frac{1+\delta^2}{2\delta}\sin\left(\frac{\omega d_w}{v_w}\right)\sin\left(\frac{\omega d_b}{v_b}\right) \qquad (5.5)$$

where ω is the phonon frequency, υ_w and υ_b are the phonon velocities in the well and barrier materials respectively, and $\delta = \rho_w \upsilon_w / \rho_b \upsilon_b$ is the ratio of the acoustic impedances of the materials, where ρ corresponds to the density of each material [130]. The dispersion relation for the SL studied in this work can be seen in Fig. 5.6(a). The elastic properties are taken from Ref. [115].

In a similar way the transmission rates of phonons of different frequency through the SL can be calculated via a transfer-matrix technique described in the work of Tamura et al. [130]. The corresponding phonon transmission spectrum is presented alongside the dispersion in Fig. 5.6(b). As is expected from the above discussion, the phonon transmission quickly tends to zero at the frequencies where phonon stop-bands open up in the dispersion. The magnitude of the reduction in the transmission is contingent on the size of the gap in the dispersion and the number of periods in the superlattice, with a greater number of periods acting as a superior filter.

A variety of processes may be involved in the generation of acoustic phonons in the superlattice: photothermal generation, deformation potential, piezoelectric and electrostriction effects [80]. Incoming acoustic strain into the lattice will cause displacement of the interfaces and local modulation of the refractive index due to transient perturbation of the electronic distribution. For any and all of these processes the physical properties of the two layers vary such that when exciting the superlattice the strain field is dominated by a periodic modulation equal to the SL period. Hence the modes at $q = 0$ are the most efficiently generated by optical excitation. Conversely, the interaction of coherent phonons with light is enhanced in backscattering geometry for acoustic wave vectors satisfying $q = 2k$ due to a phase matching requirement [128], in the reflection geometry as opposed to transmission pump-probe spectroscopy. For SLs having typical dimensions with $D_{SL} \sim 10\,\mathrm{nm}$ and probing by visible light, this means modes with wave vectors close to the center of the mini Brillouin-zone. Furthermore only phonons of wavevector $q \leq 2k$ are Raman active in backscattering and forward-scattering geometry due to the condition of momentum conservation in phonon-photon interactions. For an ideal SL there is technically no overlap between the optimal generation and detection frequencies, however in reality the finite size of SLs compared with optical wavelength and limited light absorption depth, as well as fluctuations in layer thickness, causes these selection rules to become relaxed. The term for the optical reflectivity in an opaque layer may be modified for a SL by summing over the layers [133],

$$\sum_p \frac{\partial \epsilon_p}{\partial \eta} \int_0^{d_p} dz \eta_p(z) e^{iq_p z} \left(a_p e^{ikz} + a_p e^{-ikz}\right)^2 \tag{5.6}$$

where p denotes the pth layer, q_p is the corresponding acoustic phonon wave vector, and k the effective electromagnetic wave vector in the SL. Specifically, a_p is the amplitude of the probe electric field penetrating in the SL, b_p the one reflected by the interface between substrate and SL, often negligible.

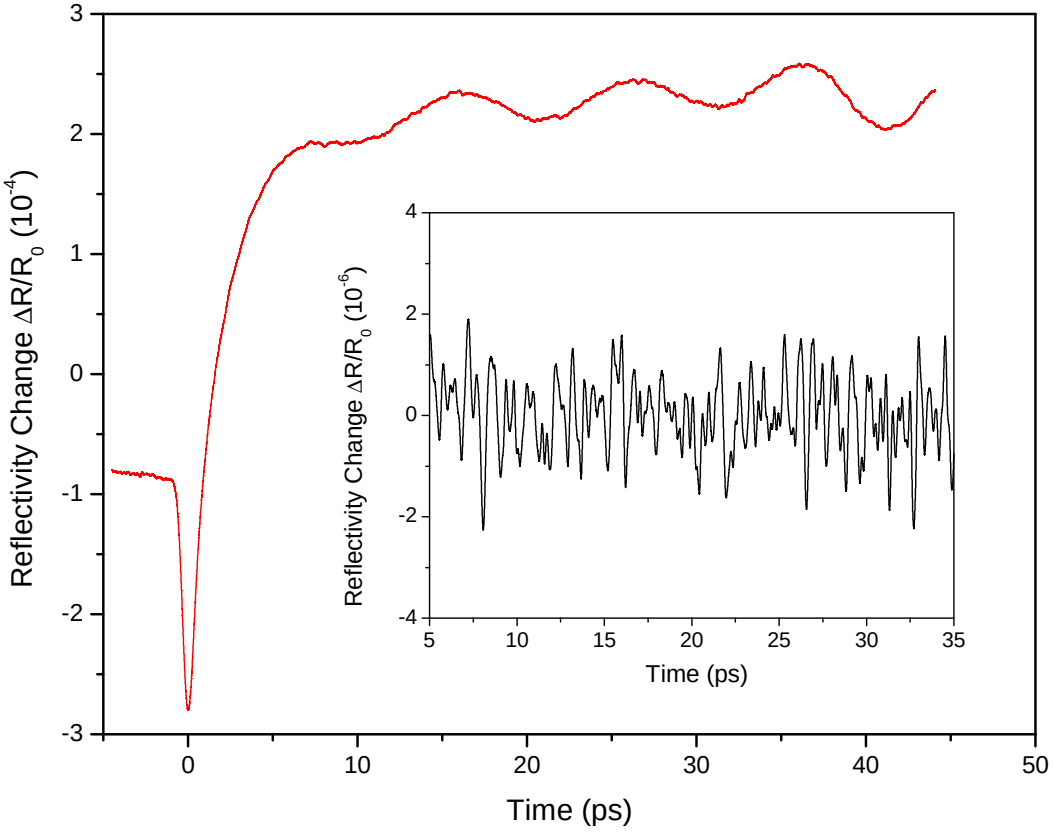

Figure 5.7: Reflectivity changes for the SL pumped at 385 nm. The inset shows the extracted high frequency oscillatory behaviour.

5.2.3 Experimental Results and Discussion

The reflectivity changes in the generation geometry are dominated by carriers excited to the first interband transition and above. Fig. 5.7 shows an initial reflectivity increase on the order $\Delta R/R_0 \approx 10^{-4}$, followed by clear Brillouin oscillations with a

frequency determined by the average properties of the lattice. The slow electronic decay and Brillouin oscillations are further modulated by very small signals created by folded acoustic phonons in the lattice with a magnitude $\Delta R/R_0 \approx 10^{-6}$ shown in the inset of Fig. 5.7. In order to separate the lattice dynamics from the carrier dynamics the high frequency signature is extracted from the reflectivity response numerically. The result is a convolution of several different modes and the signal demonstrates a weak frequency beating. The magnitude of the reflectivity modulation is an order of magnitude weaker than results obtained in similar experiments on GaAs/AlAs superlattices [70]. This is attributed to the difficulties of working in the UV regime as well as the inferior quality of the SL itself.

Nevertheless, promising results are obtained despite the statistical noise to signal ratio being ~ 1. The Fourier transform of the time resolved signal (blue solid line) in generation geometry and the nominal (red) and fitted (black) dispersion are depicted in Fig. 5.8. The SL is optically excited asymmetrically in the barrier and well regions The Fourier spectrum yields a response for three first order folded acoustic modes centred around 1200 GHz. In order to identify the wavevectors present from the peaks in the Fourier transform the frequency spectrum is superimposed on and compared to the theoretical frequency dispersion. It was found that the observed peaks did not well match the anticipated mode frequencies based on the nominal values for well and barrier thickness. A least squares solution matching the frequencies of observed peaks to a revised value for the period of the SL was used to obtain a more accurate estimate of the average well and barrier thicknesses. The revised values for the well and barrier widths was 3.76 nm and 2.86 nm respectively, corresponding to a $\sim 12\%$ disagreement in lattice parameters. One reason for discrepancies between experimental results versus the model dispersion is that layer thickness fluctuations and growth conditions may produce a material more like the alloy at the interface. This leads to a reduction of the acoustic mismatch and a narrowing of the phonon stop-bands. This only affects the zone centre modes, as at backscattering q values the dispersion can be well modelled by a folding of the average bulk dispersion. All this relies on the assumption that the literature values for longitudinal speed of sound and density in cubic GaN and AlN used for dispersion calculations quoted from Ref. [115] are valid under the strain conditions in the SL. In this way picosecond acoustics and numerical techniques may be used as a diagnostic tool for dimensional analysis of SLs with known material properties.

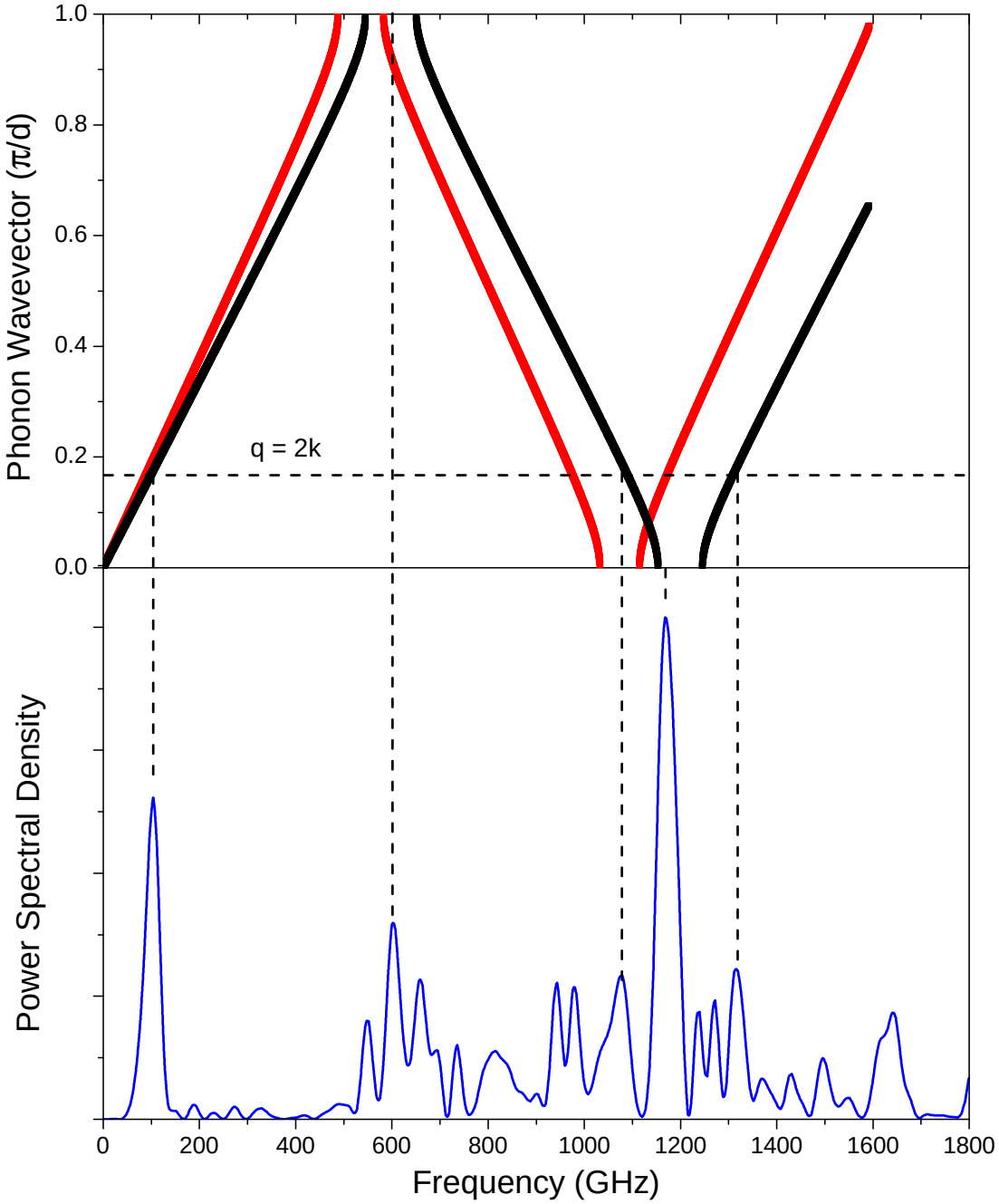

Figure 5.8: The Fourier power spectrum for the studied superlattice for pump wavelength 257 nm and probe wavelength 385 nm, plotted compared to the nominal (red) and modified (black) folded longitudinal phonon dispersion. The horizontal dashed line is the $2k_{laser}$ line.

The dominant peak in the frequency spectrum belongs to the zone center mode where generation is most efficient. Although two non-degenerate modes exist for $q = 0$ on either side of each phonon stop-band, it is commonly reported that only one is observed at a time. This is due to symmetry criteria related to the ratios between

the barrier width and the total SL period. One of the two modes enclosing each minigap displays symmetry properties resulting in an integral sum approaching zero (reaching zero for an infinite superlattice) [134]. The value of $2k_{laser} = 4\pi n/\lambda$ marked on Fig. 5.8 is estimated by averaging the refractive index n over one superlattice period for the two binary compounds, the refractive indices are sourced from Ref. [26]. The q-vectors of the two side band features accompanying the central peak match well the frequencies corresponding to the $q = 2k_{laser}$ mode. This suggests an impulsive stimulated Raman scattering mechanism in a backscattering direction for these modes. At the backscattering q value both branches of the same order are excited due to the mixing of symmetric and antisymmetric components of the strain field unlike the mini-BZ center modes. The remains of the Brillouin oscillations corresponding to the lowest order backscattering mode may be seen at around 100 GHz.

A small feature in the Fourier spectrum has been marked at around 600 GHz which frequency corresponds approximately to the expected modes at the mini-zone edge. As previously mentioned detection is enhanced at wavevectors $q = 2k_{laser}$, but entirely forbidden above these wavevectors as momentum cannot be conserved in the phonon-photon interactions. These modes are not expected to be observed as though the strain modifies the excitonic energy levels in the quantum wells the elastic strain in adjacent wells oscillate in antiphase which acts to supress the reflectivity response. A mechanism for the detection of the zone edge modes in a heavily doped SL was suggested by Beardsley et al. where the explanation for the phenomena is a three-particle interaction between electrons and holes in the nearest neighbouring wells [77]. Although the sample under study is nominally undoped the III-nitride materials grown by pa-MBE have unintentional inclusion rates of shallow donors, such as oxygen, on the order $1 \times 10^{22}/\mathrm{cm}^3$ [59,135]. Although the donors in wide band gap materials tend to be deep level only a fraction need be thermally activated to give a significant free carrier concentration. Further work would be required to confirm this observation, by comparing the free carrier concentration with the magnitude of the mini-zone edge mode.

Now results from the same sample in the detection configuration are discussed. The strain is mostly generated in the GaAs with 2.85 eV photons with while the strain pulse is detected in the superlattice surface layers with a probe beam of 4.28 eV photons. As no rapid transient reflectivity change is observed at the coincidence in time of pump and probe, it can be concluded that only the layers near to the surface are optically

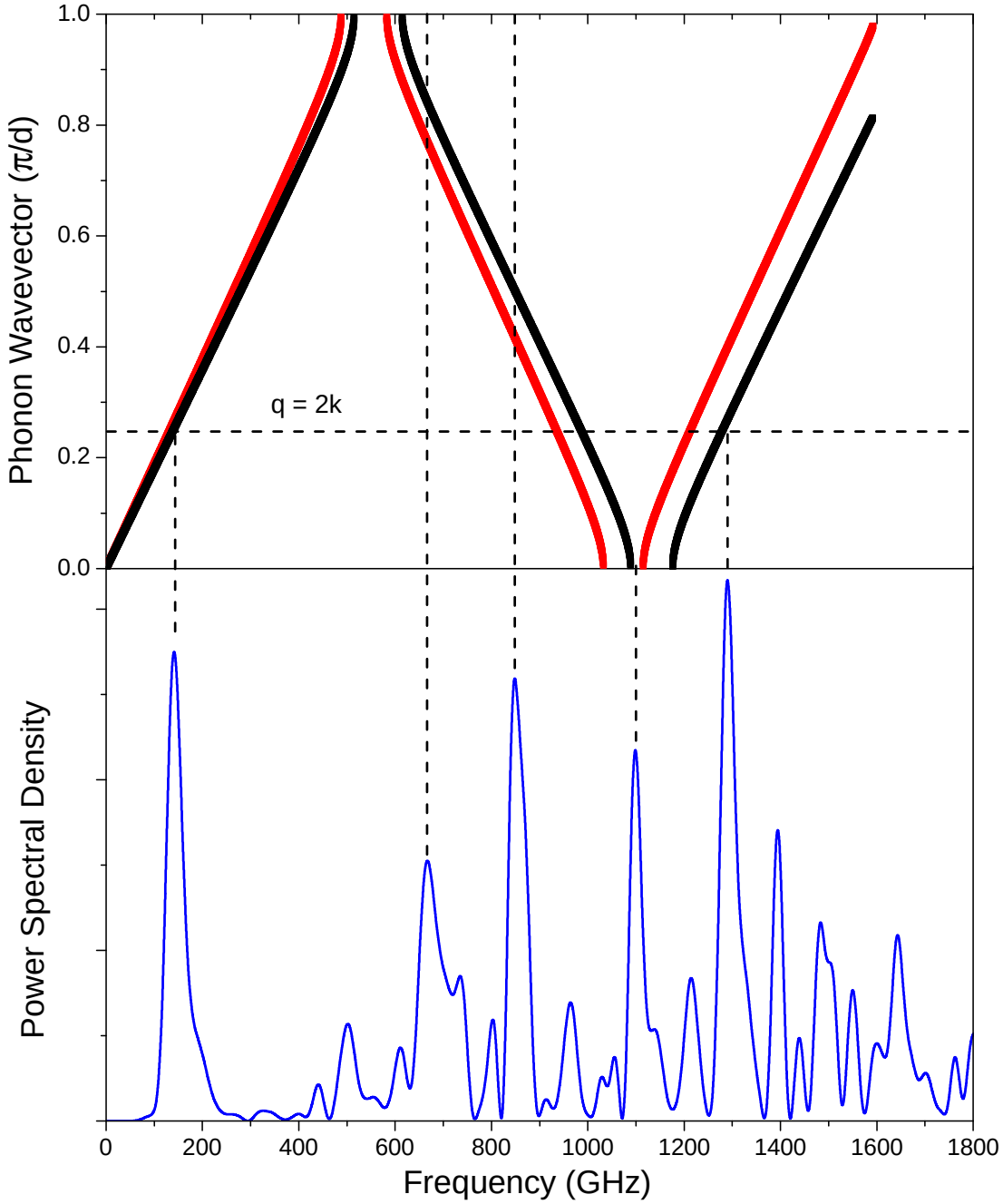

Figure 5.9: The Fourier power spectrum for the studied superlattice for pump wavelength 435 nm and probe wavelength 290 nm, plotted compared to the nominal (red) and modified (black) folded longitudinal phonon dispersion. The horizontal dashed line is the $2k_{laser}$ line.

probed. The measurement window is moved 35 ps later in time to correspond to the transition time of the acoustic pulse across the GaN buffer layer.

The Fourier transform of the time resolved signal (blue solid line) in detection ge-

ometry and the nominal (red) and fitted (black) dispersion are presented in Fig. 5.9. The amplitude of the spectral peaks are much smaller in this configuration and not much larger than the residual Brillouin oscillation contribution. The vertical dashed lines are used as a guide to the eye to denote the position of possible modes however they do not match perfectly with the fitted phonon dispersion. The revised values for the well and barrier widths was 3.98 nm and 3.03 nm respectively, corresponding to a $\sim 5.5\%$ disagreement in lattice parameters from the nominal values. Although this value differs somewhat from the previous estimate on the same sample, they are within reasonable agreement considering the level of error in the identification of mode frequencies, the random disorder of the SL, as well as potential thickness variations across the diameter of the growth wafer.

Previous work has demonstrated the potential of using superlattices as detectors of strain generated in metal films. In these experiments the results were enhanced by increasing the pump fluence to the onset of non-linear propagation across longer distances, leading to soliton formation and frequency upconversion. The GaAs substrate is a broadband transducer and probably does not produce high frequency phonons in sufficient number to excite the folded modes in this experimental geometry. Furthermore, from the condition for the optical reflectivity in Eq. (5.6), when the optical reflection at the SL/substrate interface is accounted for the optical field is modulated by $a_p^2 e^{2ikz} + a_p b_p$, with b_p being the reflected wave amplitude [128]. This results in a modified conservation rule allowing for $q = 2k$ and $q = 0$. As the probe beam does not penetrate far enough into the sample to reflect at this interface it may offer another explanation as to why the zone centre mode is not observed. Unfortunately only modes from the first order branches of the mini-BZ are observed in either experimental geometry. Higher order modes are typically excited with an order of magnitude smaller power spectral density and cannot be resolved above the noise in these experiments.

5.3 Conclusions

In this chapter of the thesis two different sample structures were studied by picosecond acoustic techniques for the generation and detection of high frequency coherent phonons. The first experimental work focused on generating and detection strain pulses in a single c-GaN quantum well with a view towards applications in ultrasonic microscopy. The transition of the acoustic pulse through the sample was tracked opti-

cally and manifested as a perturbation of the optical reflectivity in different layers of the structure. The QW was unsuccessful as a detector of strain as it was not possible to separate the photoelastic contribution of the well and barrier layers possibly due to the small thickness. The QW was then studied as an optical-acoustic transducer of strain and detected in the GaAs substrate. It was possible to resolve independent sources of strain on the picosecond timescale although the high frequency strain components from the well did not have long enough lifetimes to be reflected in the time resolved optical modulation. The half period of the narrowest detected strain pulses was around 3.5 ps and has a broadband frequency spectrum up to 170 GHz.

The second work involved exploring the generation of terahertz coherent FLA phonon modes in a zinc-blende GaN/AlN SL. The amplitude of the response from the SL in both configurations was much smaller than that observed in similar experiments on hexagonal nitrides where the internal fields couple with excited carriers to modulate the optical properties. The first order folded acoustic modes, as well as possible indication of the first order mini-zone edge mode, were observed in the generation geometry with an optical reflectivity modulation of $\Delta R/R_0 \approx 10^{-6}$. Time resolved transient reflectivity modulations up to 1.2 THz were recorded, which is almost twice that obtained for a GaAs/AlAs SL of the same period. A model fitting the peaks of the spectral transform data to the theoretical dispersion was used for dimensional analysis of the period of the SL.

Chapter 6

Conclusions and Further Work

Various cubic III-Nitride epilayers grown by pa-MBE on the (001) face of GaAs substrates have been studied by picosecond acoustic spectroscopy. This chapter will attempt to summarise the results from experiments conducted throughout the course of this work, and the main conclusions which may be drawn from them. Any opportunities for further work following on from the experiments conducted here will be discussed, with an eye toward the associated opportunities and challenges yet to be overcome in the field.

6.1 Research Outcomes

A series of c-Al $_x$Ga$_{1-x}$N epilayers with x up to 0.66 and with sub-μm thickness were prepared on (001) GaAs substrates by pa-MBE. Subsequently free-standing membranes were fabricated by back etching through the GaAs substrate. The coherent acoustic phonon dynamics of the c-Al $_x$Ga$_{1-x}$N/GaAs samples and the free-standing c-Al $_x$Ga$_{1-x}$N membranes are investigated by femtosecond pump-probe spectroscopy. By observing the frequency of the so-called Brillouin oscillations in the thin Al $_x$Ga$_{1-x}$N films in comparison with spectroscopic ellipsometry data the refractive index and extinction coefficients are obtained as a function of optical wavelength in the range 250-300 nm. The photoelastic parameters of the alloys have been derived from the analysis of Brillouin oscillations on the basis of the deformation potential mechanism of the photoelastic effect. Finally, the ability of phonons of different frequency to preserve their coherence upon reflection at the free surface was found to correlate closely with the surface roughness determined by AFM measurements. This demonstrates the possibility of using picosecond ultrasonics to measure surface roughness where the lateral length scale exceeds the optical probe wavelength.

After removing the substrate the optical cavity thickness modulation becomes the dominant mechanism for reflectivity modulation. The characteristic dilatational modes of free-standing Al $_x$Ga$_{1-x}$N membranes were studied and used to determine the longitudinal speed of sound in the alloys. The speed of sound increased approximately linearly with the increase in Al fraction. Speed of sound calculations made on the free-standing membranes were subject to significant error due to a covariance between the measured alloy layer thickness and the GaN buffer. It was not possible to rule out the presence of a bowing factor affecting the relationship between Al fraction and longitudinal velocity.

The work detailed in Chapter 5 demonstrates the potential of cubic III-Nitride heterostructures as transducers of higher frequency acoustic strain than the III-Arsenide counterparts due to the naturally higher speed of sound. The thin single c-GaN QW was unable to be disentangled from the Brillouin oscillations in the barrier layers, for any choice of barrier composition. It was however successfully applied for the generation of high frequency acoustic phonons in a buried layer and detection at another location.

For the first time folded acoustic modes in a c-GaN/AlN superlattice of $\sim$1.2 GHz are detected in reflection geometry about the mini-BZ center. Despite the amplitude of the signals being attenuated by the random disorder in the structure there is also an indication that we have observed the same modes operating in a detection regime (i.e, strain is generated outside the SL). Picosecond acoustics was applied as a tool for the dimensional analysis of the SL period with prior knowledge of the constituent materials.

6.2 Future Work

With regard to the work carried out in Chapter 4, it would be of benefit for anyone designing opto-electronic devices with the ternary nitride compounds to have access to the material parameters for the full range of aluminium content. Although samples were produced across the full range of aluminium content the photoelastic parameters are only resonant within a relatively narrow spectral window which limited our ability to study the samples for which resonances fall outside this window. Moreover, when moving into the deep UV regime a specialised set of optics (e.g, AOM, photodiode) is required to operate with any efficiency. Further study would be useful in the mid- to

upper level of Al content to investigate the onset of indirect band absorption.

In the field of cubic nitride research in general, but particularly heterostructures, device performance is severely hampered by the available material quality. One suggestion is the lattice matching of adjacent MBE grown layers to the available substrates by the introduction of indium to increase the critical thickness and reduce strain effects [136]. Nevertheless, this suggestion is already a number of years old and it is unclear if high quality c-GaN heterostructures will be realised in the near future. In the absence of readily available commercial cubic substrates for homoepitaxy the dislocation densities remain extremely high.

The experimental configuration for pump-probe measurements throughout the experiments recounted in this work relied on a mechanical delay stage. Contemporary techniques, such as asynchronous optical sampling (ASOPS) which is becoming more ubiquitous, may give signal to noise ratios in excess of 10^7. Additionally operating with a two laser system allows for better tuning of the pump and probe energies for any given sample.

List of References

[1] M. Maldovan. Sound and heat revolutions in phononics. *Nature*, 503:209, 2013.

[2] N. Li, J. Ren, L. Wang, G. Zhang, P. Hänggi, and B. Li. Colloquium: Phononics: Manipulating heat flow with electronic analogs and beyond. *Rev. Mod. Phys.*, 84(3):1045, 2012.

[3] S. Vilhunen, H. Särkkä, and M. Sillanpää. Ultraviolet light-emitting diodes in water disinfection. *Environmental Science and Pollution Research*, 16(4):439, 2009.

[4] M. N. Chong, B. Jin, C. W. K. Chow, and C. Saint. Recent developments in photocatalytic water treatment technology: a review. *Water Res.*, 44(10):2997, 2010.

[5] S. Parsons. *Advanced oxidation processes for water and wastewater treatment*. IWA Publishing: London, 2004.

[6] P. E. Hockberger. A history of ultraviolet photobiology for humans, animals and microorganisms. *Photochem. Photobiol.*, 76(6):561, 2002.

[7] M. Schreiner, J. Martínez-Abaigar, J. Glaab, and M. Jansen. Uv-b induced secondary plant metabolites. *Optik Photonik*, 9(2):34, 2014.

[8] B. Romanczyk, S. Wienecke, M. Guidry, H. Li, E. Ahmadi, X. Zheng, S. Keller, and U. K. Mishra. Demonstration of constant 8 W/mm power density at 10, 30, and 94 GHz in state-of-the-art millimeter-wave n-polar GaN MISHEMTs. *IEEE Transactions on Electron Devices*, 65(1):45, 2018.

[9] D. Carvalho, K. Müller-Caspary, M. Schowalter, T. Grieb, T. Mehrtens, A. Rosenauer, T. Ben, R. García, A. Redondo-Cubero, K. Lorenz, et al. Direct measurement of polarization-induced fields in GaN/AlN by nano-beam electron diffraction. *Scientific Reports*, 6:28459, 2016.

[10] O. Ambacher, B. Foutz, J. Smart, J. R. Shealy, N. G. Weimann, K. Chu, M. Murphy, A. J. Sierakowski, W. J. Schaff, L. F. Eastman, et al. Two dimensional electron gases induced by spontaneous and piezoelectric polarization in undoped and doped AlGaN/GaN heterostructures. *J. Appl. Phys.*, 87(1):334, 2000.

[11] P. Waltereit, O. Brandt, A. Trampert, H. T. Grahn, J. Menniger, M. Ramsteiner, M. Reiche, and K. H. Ploog. Nitride semiconductors free of electrostatic fields for efficient white light-emitting diodes. *Nature*, 406(6798):865, 2000.

[12] T. Paskova, R. Kroeger, S. Figge, D. Hommel, V. Darakchieva, B. Monemar, E. Preble, A. Hanser, N. M. Williams, and M. Tutor. High-quality bulk a-plane GaN sliced from boules in comparison to heteroepitaxially grown thick films on r-plane sapphire. *Appl. Phys. Lett.*, 89(5):051914, 2006.

[13] C. Y. Yeh, Z. W. Lu, S. Froyen, and A. Zunger. Zinc-blende–wurtzite polytypism in semiconductors. *Phys. Rev. B*, 46(16):10086, 1992.

[14] S. C. Jain, M. Willander, J. Narayan, and R. Van Overstraeten. III–nitrides: Growth, characterization, and properties. *Journal of Applied Physics*, 87(3):965, 2000.

[15] M. Magnuson, M. Mattesini, C. Höglund, J. Birch, and L. Hultman. Electronic structure and chemical bonding anisotropy investigation of wurtzite AlN. *Phys. Rev. B*, 80:155105, 2009.

[16] B. Monemar, P. P. Paskov, and A. Kasic. Optical properties of InN the bandgap question. *Superlattices and Microstructures*, 38(1):38, 2005.

[17] A. M. Witowski, K. Pakuła, J. M. Baranowski, M. L. Sadowski, and P. Wyder. Electron effective mass in hexagonal GaN. *Appl. Phys. Lett.*, 75(26):4154–4155, 1999.

[18] K. Kim, W. R. L. Lambrecht, B. Segall, and M. van Schilfgaarde. Effective masses and valence-band splittings in GaN and AlN. *Phys. Rev. B*, 56(12):7363, 1997.

[19] Y. Chang, H. W. Chu, C. Shen, H. Chen, and S. Gwo. Determination of the electron effective mass of wurtzite InN by coherent upper-branch A_1 (LO) phonon-plasmon coupling mode. *Appl. Phys. Lett.*, 90(7):072111, 2007.

[20] S. K. Pugh, D. J. Dugdale, S. Brand, and R. A. Abram. Electronic structure calculations on nitride semiconductors. *Semiconductor science and technology*, 14(1):23, 1999.

[21] R. Y. Korotkov, J. M. Gregie, and B. W. Wessels. Optical properties of the deep Mn acceptor in GaN : Mn. *Appl. Phys. Lett.*, 80(10):1731, 2002.

[22] V. M. Bermudez, C. I. Wu, and A. Kahn. AlN films on GaN: Sources of error in the photoemission measurement of electron affinity. *J. Appl. Phys.*, 89(3):1991, 2001.

[23] W. Walukiewicz, J. W. Ager, K. M. Yu, Z. Liliental-Weber, J. Wu, S. X. Li,

R. E. Jones, and J. D. Denlinger. Structure and electronic properties of InN and in–rich group III–nitride alloys. *J. Phys. D: Appl. Phys.*, 39(5):R83, 2006.

[24] I. Vurgaftman, J. R. Meyer, and L. R. Ram-Mohan. Band parameters for III-V compound semiconductors and their alloys. *J. Appl. Phys.*, 89(11):5815–5875, 2001.

[25] S. J. Pearton, C. R. Abernathy, M. E. Overberg, G. T. Thaler, D. P. Norton, N. Theodoropoulou, A. F. Hebard, Y. D. Park, F. Ren, J. Kim, et al. Wide band gap ferromagnetic semiconductors and oxides. *Journal of Applied Physics*, 93(1):1, 2003.

[26] T. Suzuki, H. Yaguchi, H. Okumura, Y. Ishida, and S. Yoshida. Optical constants of cubic GaN, AlN, and AlGaN alloys. *Jpn. J. Appl. Phys.*, 39(6A):L497, 2000.

[27] M. Röppischer, R. Goldhahn, G. Rossbach, P. Schley, C. Cobet, N. Esser, T. Schupp, K. Lischka, and D. J. As. Dielectric function of zinc-blende AlN from 1 to 20 eV: Band gap and van Hove singularities. *J. Appl. Phys.*, page 076104, 2009.

[28] J. Schormann, D. J. As, K. Lischka, P. Schley, R. Goldhahn, S. F. Li, W. Loffler, M. Hetterich, and H. Kalt. Molecular beam epitaxy of phase pure cubic InN. *Appl. Phys. Lett.*, 89(26):261903, 2006.

[29] I. Vurgaftman and J. R. Meyer. Band parameters for nitrogen-containing semiconductors. *J. Appl. Phys.*, 94(6):3675–3696, 2003.

[30] K. Kim, W. R. L. Lambrecht, and B. Segall. Elastic constants and related properties of tetrahedrally bonded BN, AlN, GaN, and InN. *Phys. Rev. B*, 53(24):16310, 1996.

[31] J. W. Matthews and A. E. Blakeslee. Defects in epitaxial multilayers: I. misfit dislocations. *J. Cryst. Growth*, 27:118, 1974.

[32] M. E. Sherwin and T. J. Drummond. Predicted elastic constants and critical layer thicknesses for cubic phase AlN, GaN, and InN on $\beta-$SiC. *J. Appl. Phys.*, 69:8423, 1991.

[33] R. Juza and H. Hahn. Über die kristallstrukturen von Cu_3n, GaN und InN metallamide und metallnitride. *Anorg. Allgen. Chem.*, 239(3):282, 1938.

[34] H. G. Grimmeiss and H. Koelmans. Über die kantenemission und andere emissionen des GaN. *Z. Naturf.*, 14:264, 1959.

[35] H. P. Maruska and J. J. Tietjen. The preparation and properties of vapor-deposited single-crystal-line GaN. *Appl. Phys. Lett.*, 15(10):327, 1969.

[36] H. Okumura, S. Misawa, and S. Yoshida. Epitaxial growth of cubic and hexag-

onal GaN on GaAs by gas-source molecular-beam epitaxy. *Appl. Phys Lett.*, 59:1058, 1991.

[37] T. S. Cheng, L. C. Jenkins, S. E. Hooper, C. T. Foxon, J. W. Orton, and D. E. Lacklison. Selective growth of zinc-blende, wurtzite, or a mixed phase of gallium nitride by molecular beam epitaxy. *Appl. Phys. Lett.*, 66(12):1509, 1995.

[38] S. V. Novikov, N. M. Stanton, R. P. Campion, C. T. Foxon, and A. J. Kent. Free-standing zinc-blende (cubic) GaN layers and substrates. *J. Cryst. Growth*, 310(17):3964, 2008.

[39] S. V. Novikov, N. M. Stanton, R. P. Campion, R. D. Morris, H. L. Geen, C. T. Foxon, and A. J. Kent. Growth and characterization of free-standing zinc-blende (cubic) GaN layers and substrates. *Semicond. Sci. Technol.*, 23(1):015018, 2008.

[40] S. V. Novikov, N. Zainal, A. V. Akimov, C. R. Staddon, A. J. Kent, and C. T. Foxon. Molecular beam epitaxy as a method for the growth of freestanding zinc-blende (cubic) GaN layers and substrates. *J. Vac. Sci. Technol. B*, 28(3):C3B1, 2010.

[41] D. J. As, F. Schmilgus, C. Wang, B. Schöttker, D. Schikora, and K. Lischka. The near band edge photoluminescence of cubic GaN epilayers. *Appl. Phys. Lett.*, 70:1311, 1997.

[42] L.-W. Sung, H.-H. Lin, and C.-T. Chia. Cubic GaN grown on (0 0 1) GaAs substrate by RF plasma assisted gas source MBE. *J. Cryst. Growth*, 241(3):320, 2002.

[43] Y. Hiroyama and M. Tamura. Effect of very thin SiC layer on heteroepitaxial growth of cubic GaN on Si (001). *Jpn. J. Appl. Phys.*, 37(6A):L630, 1998.

[44] M. Rüsing, T. Wecker, G. Berth, D. J. As, and A. Zrenner. Joint raman spectroscopy and HRXRD investigation of cubic gallium nitride layers grown on 3C-SiC. *Phys. Status Solidi B*, 253(4):778, 2016.

[45] R. C. Powell, N.-E. Lee, Y.-W. Kim, and J. E. Greene. Heteroepitaxial wurtzite and zinc-blende structure GaN grown by reactive-ion molecular-beam epitaxy: Growth kinetics, microstructure, and properties. *J. Appl. Phys.*, 73(1):189, 1993.

[46] T. Kurobe, Y. Sekiguchi, J. Suda, M. Yoshimoto, and H. Matsunami. Preferential growth of cubic GaN on sapphire (0001) substrates by metal organic molecular beam epitaxy. *Appl. Phys. Lett.*, 73(16):2305, 1998.

[47] H. Tsuchiya, K. Sunaba, T. Suemasu, and F. Hasegawa. Growth of thick and pure cubic GaN on (001) GaAs by halide VPE. *J. Cryst. Growth*, 198:1056, 1999.

[48] R. Liu and C. Bayram. Maximizing cubic phase gallium nitride surface coverage on nano-patterned silicon (100). *Appl. Phys. Lett.*, 109(4):042103, 2016.

[49] A. Nakadaira and H. Tanaka. Metalorganic vapor-phase epitaxial growth and characterization of cubic c-$Al_xGa_{1-x}N$ alloy. *Jpn. J. Appl. Phys.*, 37(3S):1449, 1998.

[50] M. Ogawa, M. Funato, T. Ishido, S. Fujita, and S. Fujita. The role of growth rates and buffer layer structures for quality improvement of cubic GaN grown on GaAs. *Jpn. J. Appl. Phys.*, 39(2A):L69, 2000.

[51] M Kakuda, S Kuboya, and K Onabe. RF-MBE growth of Si doped cubic GaN and hexagonal phase incorporated c-AlGaN films on MgO (0 0 1) substrates. *J. Cryst. Growth*, 323(1):91, 2011.

[52] M. Kakuda, K. Makino, T. Ishida, S. Kuboya, and K. Onabe. MBE growth of cubic AlN films on MgO substrate via cubic GaN buffer layer. *Phys. Status Solidi C*, 9(3):558, 2012.

[53] S. V. Novikov, C.T. Foxon, and A. J. Kent. Molecular beam epitaxy as a growth technique for achieving free-standing zinc-blende GaN and wurtzite c-$Al_xGa_{1-x}N$. *Prog. Cryst. Growth Charact. Mater.*, 63(2):25, 2017.

[54] L. He, M. A. Reshchikov, F. Yun, D. Huang, T. King, and H. Morkoç. Properties of c-$Al_xGa_{1-x}N$ layers grown by plasma-assisted molecular-beam epitaxy under Ga-rich conditions. *Appl. Phys. Lett.*, 81(12):2178, 2002.

[55] T. Schupp, K. Lischka, and D. J. As. Mbe growth of atomically smooth non-polar cubic AlN. *J. Cryst. Growth*, 312(9):1500, 2010.

[56] C. G. Van de Walle. Defects and doping in GaN. *Braz. J. Phys.*, 27(4):74, 1997.

[57] H. W. Jang, J. M. Baik, M.-K. Lee, H.-J. Shin, and J.-L. Lee. Incorporation of oxygen donors in AlGaN. *J. Electrochem. Soc.*, 151(8):G536, 2004.

[58] S. Yoshida, S. Misawa, and S. Gonda. Properties of c-$Al_xGa_{1-x}N$ films prepared by reactive molecular beam epitaxy. *J. Appl. Phys.*, 53(10):6844, 1982.

[59] S. V. Novikov and C. T. Foxon. Unintentional boron incorporation in AlGaN layers grown by plasma-assisted MBE using highly efficient nitrogen RF plasma-sources. *J. Cryst. Growth*, 477:154, 2017.

[60] J. W. Hunt, M. Arditi, and F. S. Foster. Ultrasound transducers for pulse-echo medical imaging. *IEEE Trans. Biomed. Eng.*, 30(8):453, 1983.

[61] C. Thomsen, J. Strait, Z. Vardeny, Maris. H. J., and J. Tauc. Coherent phonon generation and detection by picosecond light pulses. *Phys. Rev. Lett.*, 53(10):989, 1984.

[62] C. Thomsen, H. T. Grahn, H. J. Maris, and J. Tauc. Surface generation and detection of phonons by picosecond light pulses. *Phys. Rev. B*, 34(6):4129, 1986.

[63] O. B. Wright and K. Kawashima. Coherent phonon detection from ultrafast surface vibrations. *Phys. Rev. Lett.*, 69(11):1668, 1992.

[64] H. T. Grahn, H. J. Maris, and J. Tauc. Picosecond ultrasonics. *IEEE Journal of Quantum Electronics*, 25(12):2562, 1989.

[65] O. B. Wright. Thickness and sound velocity measurement in thin transparent films with laser picosecond acoustics. *J. Appl. Phys.*, 71(4):1617, 1992.

[66] E. Tzianaki, M. Bakarezos, G. D. Tsibidis, Y. Orphanos, P. A. Loukakos, C. Kosmidis, P. Patsalas, M. Tatarakis, and N. A. Papadogiannis. High acoustic strains in si through ultrafast laser excitation of ti thin-film transducers. *Opt. Express*, 23(13):17191, 2015.

[67] O. B. Wright and T. Hyoguchi. Ultrafast vibration and laser acoustics in thin transparent films. *Opt. Lett.*, 16(19):1529, 1991.

[68] T. Czerniuk, T. Ehrlich, T. Wecker, D. J. As, D. R. Yakovlev, A. V. Akimov, and M. Bayer. Picosecond acoustics in single quantum wells of cubic GaN/(AlGa)N. *Phys. Rev. Appl.*, 7(1):014006, 2017.

[69] K. Mizoguchi, M. Hase, S. Nakashima, and M. Nakayama. Observation of coherent folded acoustic phonons propagating in a GaAs/AlAs superlattice by two-color pump-probe spectroscopy. *Phys. Rev. B*, 60(11):8262, 1999.

[70] A. Bartels, T. Dekorsy, H. Kurz, and K. Köhler. Coherent zone-folded longitudinal acoustic phonons in semiconductor superlattices: excitation and detection. *Phys. Rev. Lett.*, 82(5):1044, 1999.

[71] A. V. Scherbakov, P. J. S. Van Capel, A. V. Akimov, J. I. Dijkhuis, D. R. Yakovlev, T. Berstermann, and M. Bayer. Chirping of an optical transition by an ultrafast acoustic soliton train in a semiconductor quantum well. *Phys. Rev. Lett.*, 99(5):057402, 2007.

[72] C.-K. Sun, J.-C. Liang, and X.-Y. Yu. Coherent acoustic phonon oscillations in semiconductor multiple quantum wells with piezoelectric fields. *Phys. Rev. Lett.*, 84(1):179, 2000.

[73] K.-H. Lin, C.-T. Yu, Y.-C. Wen, and C.-K. Sun. Generation of picosecond acoustic pulses using a p-n junction with piezoelectric effects. *Appl. Phys. Lett.*, 86(9):093110, 2005.

[74] S. Wu, P. Geiser, J. Jun, J. Karpinski, J.-R. Park, and R. Sobolewski. Long-

lived, coherent acoustic phonon oscillations in GaN single crystals. *Appl. Phys. Lett.*, 88(4):041917, 2006.

[75] D. Moss, A. V. Akimov, S. V. Novikov, R. P. Campion, C. R. Staddon, N. Zainal, C. T. Foxon, and A. J. Kent. Elasto-optical properties of zinc-blende (cubic) gan measured by picosecond acoustics. *Journal of Physics D: Applied Physics*, 42(11):115412, 2009.

[76] C. He, M. Grossmann, D. Brick, M. Schubert, S. V. Novikov, C. T. Foxon, V. Gusev, A. J. Kent, and T. Dekorsy. Study of confined coherent acoustic phonon modes in a free-standing cubic GaN membrane by femtosecond spectroscopy. *Appl. Phys. Lett.*, 107(11):112105, 2015.

[77] R. P. Beardsley, R. P. Campion, B. A. Glavin, and A. J. Kent. A GaAs/AlAs superlattice as an electrically pumped THz acoustic phonon amplifier. *New J. Phys.*, 13(7):073007, 2011.

[78] W Maryam, A. V. Akimov, R. P. Campion, and A. J. Kent. Dynamics of a vertical cavity quantum cascade phonon laser structure. *Nature communications*, 4:2184, 2013.

[79] P. Ruello and V. É. Gusev. Physical mechanisms of coherent acoustic phonons generation by ultrafast laser action. *Ultrasonics*, 56:21, 2015.

[80] O. Matsuda, M. C. Larciprete, R. L. Voti, and O. B. Wright. Fundamentals of picosecond laser ultrasonics. *Ultrasonics*, 56:3, 2015.

[81] E. S. K. Young, A. V. Akimov, R. P. Campion, A. J. Kent, and V. Gusev. Picosecond strain pulses generated by a supersonically expanding electron-hole plasma in GaAs. *Phys. Rev. B*, 86(15):155207, 2012.

[82] P. Babilotte, P. Ruello, D. Mounier, T. Pezeril, G. Vaudel, M. Edely, J. M. Breteau, V. Gusev, and K. Blary. Femtosecond laser generation and detection of high-frequency acoustic phonons in GaAs semiconductors. *Phys. Rev. B*, 81(24):245207, 2010.

[83] J. Bardeen and W. Shockley. Deformation potentials and mobilities in non-polar crystals. *Phys. Rev.*, 80(1):72, 1950.

[84] B. P. Zakharchenya, D. N. Mirlin, V. I. Perel', and I. I. Reshina. Spectrum and polarization of hot-electron photoluminescence in semiconductors. *Sov. Phys. Usp.*, 25(3):143, 1982.

[85] O. B. Wright, B. Perrin, O. Matsuda, and V. É. Gusev. Ultrafast carrier diffusion in gallium arsenide probed with picosecond acoustic pulses. *Phys. Rev. B*, 64(8):081202, 2001.

[86] J. Möreke, M. J. Uren, S. V. Novikov, C. T. Foxon, S. Hosseini Vajargah, D. J. Wallis, C. J. Humphreys, S. J. Haigh, A. Al-Khalidi, E. Wasige, et al. Investigation of the GaN-on-GaAs interface for vertical power device applications. *J. Appl. Phys.*, 116(1):014502, 2014.

[87] S. A. Akhmanov and V. É. Gusev. Laser excitation of ultrashort acoustic pulses: New possibilities in solid-state spectroscopy, diagnostics of fast processes, and nonlinear acoustics. *Sov. Phys. Usp.*, 35(3):153, 1992.

[88] M. Cardona and P. Y. Yu. *Fundamentals of semiconductors: Physics and material properties*. Springer, 2005.

[89] P. A. Knipp and T. L. Reinecke. Coupling between electrons and acoustic phonons in semiconductor nanostructures. *Phys. Rev. B*, 52(8):5923, 1995.

[90] J. H. Davies. *The physics of low-dimensional semiconductors: an introduction*. Cambridge University Press, 1998.

[91] Ziman. J. M. *Electrons and phonons: the theory of transport phenomena in solids*. Oxford university press, 1960.

[92] Z. Tian, K. Esfarjani, and G. Chen. Enhancing phonon transmission across a Si/Ge interface by atomic roughness: First-principles study with the Green's function method. *Phys. Rev. B*, 86(23):235304, 2012.

[93] H. J. Maris. *Physical Acoustics*, volume 8, chapter 6, pages 280–342. Academic Press, 1971.

[94] B. C. Daly, K. Kang, Y. Wang, and D. G. Cahill. Picosecond ultrasonic measurements of attenuation of longitudinal acoustic phonons in silicon. *Phys. Rev. B*, 80(17):174112, 2009.

[95] T.-M. Liu, S.-Z. Sun, C.-F. Chang, C.-C. Pan, G.-T. Chen, J.-I. Chyi, V. Gusev, and C.-K. Sun. Anharmonic decay of subterahertz coherent acoustic phonons in GaN. *Appl. Phys. Lett.*, 90(4):041902, 2007.

[96] J. Zi, X. Wan, G. Wei, K. Zhang, and X. Xie. Lattice dynamics of zinc-blende GaN and AlN: I. bulk phonons. *J. Phys.: Condens. Matter*, 8(35):6323, 1996.

[97] P. J. S. van Capel, E. Péronne, and J. I. Dijkhuis. Nonlinear ultrafast acoustics at the nano scale. *Ultrasonics*, 56:36, 2015.

[98] H.-N. Lin, R. J. Stoner, H. J. Maris, and J. Tauc. Phonon attenuation and velocity measurements in transparent materials by picosecond acoustic interferometry. *J. Appl. Phys.*, 69(7):3816, 1991.

[99] C. Thomsen, H. T. Grahn, H. J. Maris, and J. Tauc. Picosecond interferometric

technique for study of phonons in the Brillouin frequency range. *Opt. Commun.*, 60:55, 1986.

[100] A. Devos, J.-F. Robillard, R. Côte, and P. Emery. High-laser-wavelength sensitivity of the picosecond ultrasonic response in transparent thin films. *Phys. Rev. B*, 74(6):064114, 2006.

[101] R. D. Mindlin. *An introduction to the mathematical theory of vibrations of elastic plates*. World Scientific, 2006.

[102] A. V. Akimov, E. S. K. Young, J. S. Sharp, V. Gusev, and A. J. Kent. Coherent hypersonic closed-pipe organ like modes in supported polymer films. *Appl. Phys. Lett.*, 99(2):021912, 2011.

[103] F. Hudert, A. Bruchhausen, D. Issenmann, O. Schecker, R. Waitz, A. Erbe, E. Scheer, T. Dekorsy, A. Mlayah, and J.-R. Huntzinger. Confined longitudinal acoustic phonon modes in free-standing Si membranes coherently excited by femtosecond laser pulses. *Phys. Rev. B*, 79(20):201307, 2009.

[104] M. Schubert, M. Grossmann, C. He, D. Brick, P. Scheel, O. Ristow, V. Gusev, and T. Dekorsy. Generation and detection of gigahertz acoustic oscillations in thin membranes. *Ultrasonics*, 56:109, 2015.

[105] N. D. Lanzillotti-Kimura, A. Fainstein, and B. Jusserand. Towards GHz–THz cavity optomechanics in DBR-based semiconductor resonators. *Ultrasonics*, 56:80, 2015.

[106] C. H. Chen, Y. F. Chen, An Shih, S. C. Lee, and H. X. Jiang. Zone-folding effect on optical phonon in GaN/c-$Al_{0.2}Ga_{0.8}N$ superlattices. *Appl. Phys. Lett.*, 78(20):3035, 2001.

[107] C. E. Martinez, N. M. Stanton, P. M. Walker, A. J. Kent, S. V. Novikov, and C. T. Foxon. Generation of terahertz monochromatic acoustic phonon pulses by femtosecond optical excitation of a GaN/AlN superlattice. *Appl. Phys. Lett.*, 86(22):221915, 2005.

[108] S. Mizuno. Acoustic phonon modes and phononic bandgaps in GaN/AlN nanowire superlattices. *Nanoscale Res. Lett.*, 7:479, 2012.

[109] G. Feuillet, H. Hamaguchi, K. Ohta, P. Hacke, H. Okumura, and S. Yoshida. Arsenic mediated reconstructions on cubic (001) GaN. *Appl. Phys. Lett.*, 70(8):1025, 1997.

[110] H. Tompkins and E. A. Irene. *Handbook of Ellipsometry*. William Andrew, 2005.

[111] R. E. L. Powell, S. V. Novikov, F. Luckert, P. R. Edwards, A. V. Akimov, C. T. Foxon, R. W. Martin, and A. J. Kent. Carrier localization and related photolu-

minescence in cubic AlGaN epilayers. *Journal of Applied Physics*, 110(6):063517, 2011.

[112] H. Okumura, T. Koizumi, Y. Ishida, H. Yaguchi, and S. Yoshida. Optical characterization of cubic AlGaN epilayers by cathodoluminescence and spectroscopic ellipsometry. *Phys. Status Solidi C*, 216(1):211, 1999.

[113] E. Martinez-Guerrero, F. Enjalbert, J. Barjon, E. Bellet-Almaric, B. Daudin, G. Ferro, D. Jalabert, L. Si Dang, H. Mariette, Y. Monteil, et al. Optical Characterization of MBE Grown Zinc-Blende AlGaN. *Phys. Status Solidi A*, 188(2):695, 2001.

[114] M. Landmann, E. Rauls, W. G. Schmidt, M. Röppischer, C. Cobet, N. Esser, T. Schupp, D. J. As, M. Feneberg, and R. Goldhahn. Transition energies and direct-indirect band gap crossing in zinc-blende c-$Al_xGa_{1-x}N$. *Phys. Rev. B*, 87(19):195210, 2013.

[115] A. F. Wright. Elastic properties of zinc-blende and wurtzite AlN, GaN, and InN. *J. Appl. Phys.*, 82(6):2833–2839, 1997.

[116] M. Feneberg, M. Röppischer, C. Cobet, N. Esser, J. Schörmann, T. Schupp, D. J. As, F. Hörich, J. Bläsing, A. Krost, et al. Optical properties of cubic GaN from 1 to 20 eV. *Phys. Rev. B*, 85(15):155207, 2012.

[117] R. Riane, A. Zaoui, S. F. Matar, and A. Abdiche. Pressure dependence of electronic and optical properties of zinc-blende GaN, BN and their $B_{0.25}Ga_{0.75}N$ alloy. *Physica B: Condensed Matter*, 405(3):985, 2010.

[118] P. Etchegoin, J. Kircher, M. Cardona, C. Grein, and E. Bustarret. Piezo-optics of GaAs. *Phys. Rev. B*, 46(23):15139, 1992.

[119] O. Matsuda, T. Tachizaki, T. Fukui, J. J. Baumberg, and O. B. Wright. Acoustic phonon generation and detection in GaAs/Al $_{0.3}Ga_{0.7}As$ quantum wells with picosecond laser pulses. *Phys. Rev. B*, 71(11):115330, 2005.

[120] A. N. Cleland. *Foundations of nanomechanics: from solid-state theory to device applications*. Springer Science & Business Media, 2013.

[121] T. Dehoux, M. A. Ghanem, O. F. Zouani, M. Ducousso, N. Chigarev, C. Rossignol, N. Tsapis, M.-C. Durrieu, and B. Audoin. Probing single-cell mechanics with picosecond ultrasonics. *Ultrasonics*, 56:160, 2015.

[122] G. Vogg, T. Heidmann, and S. Brand. Scanning acoustic GHz-microscopy versus conventional SAM for advanced assessment of ball bond and metal interfaces in microelectronic devices. *Microelectronics Reliability*, 55:1554, 2015.

[123] A. V. Akimov, C. L. Poyser, and A. J. Kent. Review of microwave

electro-phononics in semiconductor nanostructures. *Semicond. Sci. Technol.*, 32(5):053003, 2017.

[124] D. M. Moss, A. V. Akimov, B. A. Glavin, M. Henini, and A. J. Kent. Ultrafast strain-induced current in a GaAs Schottky diode. *Phys. Rev. Lett.*, 106(6):06602, 2011.

[125] D. M. Moss, A. V. Akimov, R. P. Campion, and A. J. Kent. Ultrafast strain-induced electronic transport in a GaAs pn junction diode. *Chinese Journal of Physics*, 49(1):499, 2011.

[126] D. Moss, A. V. Akimov, R. P. Campion, M. Henini, C. T. Foxon, L. Eaves, A. J. Kent, and B. A. Glavin. Picosecond strain pulses probed by the photocurrent in semiconductor devices with quantum wells. *Phys. Rev. B*, 83(24):245303, 2011.

[127] D. E. Aspnes, S. M. Kelso, R. A. Logan, and R. Bhat. Optical properties of $Al_xGa_{1-x}As$. *J. Appl. Phys.*, 60(2):754, 1986.

[128] A. Huynh, B. Perrin, and A. Lemaître. Semiconductor superlattices: A tool for terahertz acoustics. *Ultrasonics*, 56:66, 2015.

[129] Z. Wei, W. Chen, Z. Chen, K. Bi, J. Yang, and Y. Chen. Phonon filtering for reduced thermal conductance in unconventional superlattices. *Appl. Phys Express*, 10(8):085801, 2017.

[130] S. I. Tamura, D. C. Hurley, and J. P. Wolfe. Acoustic-phonon propagation in superlattices. *Physical Review B*, 38(2):1427, 1988.

[131] S. M. Rytov. Acoustical properties of a thinly laminated medium. *Soviet Physics Acoustic*, 2:68, 1956.

[132] M. W. C. Dharma-Wardana, P. X. Zhang, and D. J. Lockwood. Finite-size effects on superlattice acoustic phonons. *Physical Review B*, 48(16):11960, 1993.

[133] C. Rossignol and B. Perrin. Picosecond ultrasonics study of periodic multilayers. In *Analytical Sciences/Supplements Proceedings of 11th International Conference of Photoacoustic and Photothermal Phenomena*, page s245, 2002.

[134] M. F. Pascual-Winter, A. Fainstein, B. Jusserand, B. Perrin, and A. Lemaître. Spectral responses of phonon optical generation and detection in superlattices. *Physical Review B*, 85(23):235443, 2012.

[135] G. A. Slack, L. J. Schowalter, D. Morelli, and J. A. Freitas Jr. Some effects of oxygen impurities on AlN and GaN. *J. Cryst. Growth*, 246(3):287, 2002.

[136] D. J. As, M. Schnietz, J. Schörmann, S. Potthast, J W. Gerlach, J. Vogt, and K. Lischka. MBE growth of cubic $Al_xIn_{1-x}N$ and $Al_xGa_yIn_{1-x-y}N$ lattice matched to GaN. *Phys. Status Solidi C*, 4(7):2318, 2007.